ISBN 978-82-326-2858-2 (printed version)
ISBN 978-82-326-2859-9 (electronic version)
ISSN 1503-8181

Doctoral theses at NTNU, 2018:30

Ehsan Khalili

Fluid-Structure Interaction and Immersed Boundary Method for the Compressible Navier–Stokes Equations Using High Order Methods

NTNU
Norwegian University of
Science and Technology
Faculty of Engineering
Department of Energy and
Process Engineering

NTNU
Norwegian University of
Science and Technology

Doctoral theses at NTNU, 2018:30

NTNU

NTNU
Norwegian University of
Science and Technology

Ehsan Khalili

Fluid-Structure Interaction and Immersed Boundary Method for the Compressible Navier–Stokes Equations Using High Order Methods

Thesis for the degree of Philosophiae Doctor

Trondheim, December 2017

Norwegian University of Science and Technology
Faculty of Engineering
Department of Energy and
Process Engineering

NTNU
Norwegian University of
Science and Technology

NTNU
Norwegian University of Science and Technology

Thesis for the degree of Philosophiae Doctor

Faculty of Engineering
Department of Energy and
Process Engineering

ISBN 978-82-326-2858-2 (printed version)
ISBN 978-82-326-2859-9 (electronic version)
ISSN 1503-8181

Doctoral theses at NTNU, 2018:30

Printed by Skipnes Kommunikasjon as

To my parents
and
my sisters

The wound is where,
the light enters you.

Rumi

Vether it's worth while goin' through so much,
to learn so little, as the charity-boy said
ven he got to the end of the alphabet,
is a matter o' taste.

Charles Dickens

Abstract

There has been a growing interest in the study of biological flows in biomechanical systems in recent years. Such flows mostly appear in domains with complex geometries, flexible moving boundaries and usually involve fluid-structure interaction (FSI). The simulation of such problems is computationally challenging. The demand for simulating more complex flow problems more efficiently has motivated the development of the more sophisticated and more accurate numerical models. This dissertation presents a framework for simulating the fluid dynamical behaviour of viscous compressible flows around moving bodies and complex geometries as well as FSI.

The first part of the dissertation considers fluid-structure interaction in a simplified 2D model of the upper airways in order to investigate the flow-induced oscillation of the soft palate in the pharynx. This study is related to disorders in the human upper airways, in particular those associated with snoring and obstructive sleep apnoea syndrome (OSAS). A simplified 2D model has been developed to simulate the interaction between the soft palate and compressible viscous flow. The Arbitrary Lagrangian–Eulerian (ALE) formulation is employed to handle the fluid flow in Eulerian description using moving fluid grids and the plate structure in a Lagrangian formulation using stationary structure grids. The coupling between the fluid and the structure is handled by a partitioned approach where forces and deformations are exchanged between the flow and the deformable structure in each time step. To enable the solver to be applicable to larger simulations and to accommodate geometric flexibility with high order summation-by-parts (SBP) difference operators, a multi-block approach is employed to decompose the computational domain and to parallelize the solver. The idealized soft palate is first modeled by the Euler–Bernoulli thin beam theory and then by an inextensible thin beam model. Effects of kinematic as well as structural properties are examined. It has been illustrated that the structure oscillation induces sound generation.

The second part of the dissertation is devoted to devise an efficient and versatile immersed boundary method (IBM) for simulating compressible viscous flows with complex and moving boundaries employing high order summation-by-parts difference operators. The proposed Cartesian grid based immersed boundary method builds on the ghost point approach in which the

solid wall boundary conditions are applied as sharp interface conditions. The interpolation of the flow variables at image points and the solid wall boundary conditions are used to determine the flow variables on three layers of ghost points within the solid body in order to introduce the presence of the body interface in the flow computation and to maintain the overall high order of accuracy of the flow solver. Two different reconstruction procedures, bilinear interpolation and weighted least squares method, are implemented to obtain the values at the ghost points. A robust high order immersed boundary method is achieved by using a hybrid approach where the layers of ghost points are treated differently. The first layer of ghost points is treated by using a third order polynomial combined with the weighted least squares method and the second and third layers of ghost points are treated by finding the image points of the corresponding ghost points and using bilinear interpolation to find the values at the image points. After demonstrating the accuracy of the present IBM for low Mach number flow around a circular cylinder, it is applied to simulate flow in the upper airways with the cross-section of the complex geometry of a specific OSAS patient. The IBM solver has been further verified and validated for moving boundaries by applying it to a transversely oscillating cylinder in free-stream flow and an in-line oscillating cylinder in an initially quiescent fluid. Sound waves generated by the in-line oscillation of the cylinder exhibit both quadrupole and monopole types.

Preface

This dissertation is submitted in partial fulfillment of the requirements for the degree of Philosophiae Doctor (Ph.D.) at the Norwegian University of Science and Technology (NTNU). The research has been conducted at the Department of Energy and Process Engineering (EPT) from September 2014 to December 2017. The Ph.D. Project has been a part of the research project entitled *Modeling of obstructive sleep apnea by fluid-structure interaction in the upper airways* funded by the Research Council of Norway under grant number 231741.

I would first and foremost like to offer my sincerest gratitude to my supervisor, Professor Bernhard Müller, for trusting me and giving me this great opportunity. I am deeply grateful for his continuous support, positiveness and guidance. His passion for doing research and sharp eyes for analyzing physics behind each problem have been a great source of inspiration. I have truly enjoyed all the moments discussing the numerical approaches and fluid mechanics with him either on the whiteboard or by the round table in his office. I would specially like to thank my co-supervisor Dr. Martin Larsson for his expertise, experience, excellent advice and all scientific discussions. He has always been patient with all my programming questions and tried to teach me new tricks and tools. I have always been fascinated by how quickly he could make things simple and elegant. Working with you, Bernd and Martin, had a great influence on me, though now I wish I had learned more from you. I will definitely miss our meetings, every other Friday at 16.30 o'clock!

I am very grateful to the entire OSAS project team, Mads Henrik Strand Moxness and Ståle Nordgård at Department of Neuroscience (Faculty of Medicine, NTNU), Hongliang Liu and Bjørn Helge Skallerud at the Department of Structural Engineering (Faculty of Engineering Science, NTNU), and Sverre Gullikstad Johnsen, Paul Roger Leinan, Are Simonsen and Sigrid Kaarstad Dahl at SINTEF Materials and Chemistry, for interesting discussions in our meetings. I have been so fortunate to be involved in this multidisciplinary research group.

I wish to thank NTNU and NOTUR for providing computing facilities and computing time on Kongull and on Vilje. I also want to express my appreciation to the staff at these high performance computing facilities for

their excellent support.

Thanks to all my friends and colleagues at the Department of Energy and Process Engineering for making this study a fun and pleasant experience. In particular my fellow Ph.D. students in the fluid mechanics research group, Jan Bartl, Marin Prebeg, Øyvind Waage Hanssen-Bauer, Jørgen Røysland Aarnes and Son Tung Dang for sharing succession of satisfaction and frustration of Ph.D. studies with each other.

I also thank my friends who have helped me tremendously during my stay in Trondheim and have shared many delightful events and gatherings with me, particularly Reza Sabzi and Negar Olfati. Special thanks goes to Hamed Fouladi for his great friendship and all signal processing and mathematical discussions.

My extended thanks further go to my friend, Hossein Yahyazadeh, for motivating me to pursue Ph.D. studies abroad. He was a great source of help and inspiration for me during my M.Sc. studies.

Last, and most importantly, my deepest gratitude goes to my family for their endless kindness and love. My parents, Zobeydeh Golpour and Hossein Khalili, have always supported me in every decision I have made in life. I would not have been able to come this far without their constant support and care. I would also like to thank to my lovely sisters, Azadeh and Arezoo, for their continuous encouragement and affection throughout the years even after I moved to Norway.

Trondheim, December 2017
Ehsan Khalili

Contents

List of Figures

CHAPTER 1

Introduction

This chapter provides a general introduction of this thesis. The outline of the thesis including motivations and contributions is also presented.

1.1 Fluid-Structure Interaction

Various processes in engineering and nature are associated with coupled problems. Many examples of coupled systems can be found in practice. One of the most common examples is fluid-structure interaction (FSI) where motions of structural components with the surrounding fluid are considered. In order to understand the fluid forces on the structure and similarly the structural responses on the fluid, a detailed study for the interaction between the fluid and structure is required by solving their coupled behavior. Fluid-structure interaction coupling is present in many engineering applications and almost all natural phenomena. Typical examples of this interaction include engineering systems such as flow interaction with flexible pipes [86], engines, pumps, compressors, turbines, ventilation systems, aeroelasticity phenomena like aircraft wing flutter, flutter of flags, wind-induced vibration of structures and hydroelasticity phenomena such as interaction of ocean and sea currents with off-shore platforms [100, 107]. Furthermore, fluid-structure interaction is the keystone in motion of many biological species such as insects, birds, fish, cells and bacteria [16, 119].

With growing interest in the multidisciplinary field of biomedical and biomechanical engineering, a vast amount of research has been conducted to comprehend fluid-structure interaction in physiological systems in the human body [64, 65]. One of the main examples of FSI in biomechanical systems is the dynamics of the upper airways where the interaction between inspiratory and expiratory airflow with soft tissues may lead to complex flow regimes in the upper airways. Understanding biological flows in biomechan-

ical systems requires FSI models to inspect the cases of complex geometry, large structural deformation and complete closure of the fluid domain in the system.

The interaction between the fluid flow and the structure occurs at the interface where forces act on the structural boundary because of the fluid pressure and viscous stress [100]. The structure is deformed by these forces and correspondingly, the fluid domain changes. As a result, the fluid domain changes lead to changes in the flow field. That is, the solution to each part has to be taken into account as a boundary condition on the interface for the other part [100]. As mentioned, the interface deformation determines the fluid flow behaviour and at the same time, the deformation and the displacement of the structure are complied by the fluid forces, owing to this dependency, the interaction between the fluid and the structure cannot be considered as a linear problem. Thus, the whole coupled problem in most of the cases is unlikely to be solved analytically, hence, it leads to solving FSI problem numerically. Solving the coupled fluid-structure interaction problem numerically clearly consists in the numerical solutions to the fluid flow and the structural components involved in the system [100, 107].

The computational models are based on the equations which govern the physics of the problem. Fluid motion is commonly described in a Eulerian (spatial) formulation where the governing equations are written as the rate of change of mass, momentum and energy in a control volume. Conversely to fluid dynamics, the Lagrangian (material) formulation is employed for the description of the governing equations of structural dynamics [22]. In the Lagrangian formulation, the displacement or deformation of the solid is followed in time relative to its initial position. The discretized solid-fluid interface is changing in time and thereby causes a moving and deforming mesh of the changing fluid domain with a grid velocity equal to the material velocity at the fluid-solid interface [22]. Computational fluid dynamics (CFD) and computational structural dynamics (CSD) have developed many efficient approaches for solving various fluid and structure dynamics problems numerically.

In some applications, the structural response to the fluid can be ignored and only the dynamics of the fluid flow is sufficient to be considered. In some other applications, the fluid forces are insignificant compared to other forces exerted externally. Therefore, the structural problem may be solved without taking into account the fluid flow response. Nevertheless, in many applications the fluid forces and the structural deformations cannot be solved independently and special approaches for the coupled solution of fluid and structure dynamics problems are needed [100, 107]. Although many efficient and sophisticated solvers have been developed for solving both fluid and

structural problems, improving and developing solvers for modeling different FSI problems are still challenges and goals to achieve.

1.2 Classification of Fluid-Structure Interaction Approaches

In order to solve FSI problems, information has to be communicated between the flow and structural fields. The approaches for solving fluid-structure interaction problems can be broadly classified into partitioned and monolithic approaches in terms of the underlying algorithmic approach and solution strategy for information exchange [46].

1.2.1 Partitioned Approach

In the partitioned interaction approach [46, 85], the coupled problem is partitioned into fluid and structural parts and each part is solved separately with its own corresponding numerical approaches. The communication between fluid and structural solvers is performed through interface conditions.

The major advantage of this coupling approach is that it permits the use of existing developed, efficient and validated solvers for each of the fluid and structure fields, and allows to treat the solution of each sub-problem as a black box. Therefore, complexity of the fluid flow and arbitrary deformation of the structure can properly be modeled based on the versatility of the two solvers. Since the validation process is only constrained to the interface communication, the only programming effort is to develop suitable procedures for interaction between the solvers at the interface or interaction surface [70, 107].

The main drawback of this approach comes from the explicit nature of this coupling algorithm which may cause convergence problems. Since the interface location and related variables are unknown and change in time, the tracking and updating of the interface may become complicated and cause divergence errors. Owning to these issues, the stability of the partitioned approach is usually restricted by a maximum allowable time step. Therefore, there is a limitation on the range of time steps that can be chosen even though implicit time integration schemes are employed by the two solvers individually [70, 107].

The partitioned method can further be categorized into weakly (loosely) and strongly coupled algorithms [15, 46]. In both of these approaches, the fluid and structure are solved independently. In the loose coupling method, the fluid flow and structural variables are not updated iteratively to obtain a converged solution for the interface at each time step. Conversely, sub-iterations at each time step will be used in strong coupling to enforce the

convergence of the fluid flow variables and the deformation and displacement of the structure.

1.2.2 Monolithic Approach

In the monolithic approach [51, 98, 121], conversely to the partitioned coupling strategy, both fluid and structure of the FSI problem are solved simultaneously in the same mathematical framework. For this purpose, a unified formulation and algorithm needs to be developed to simulate the whole fluid and structure domain. One unified system of equations resulting from discretising the governing fluid and structural equations and taking into account the boundary conditions at the interface needs to be solved. Therefore, a monolithic algorithm is used to solve the whole FSI problem [51, 98].

The monolithic algorithms are more difficult to develop and to program, contrary to the partitioned coupling approach. Solving the whole fluid-structure interaction problem simultaneously typically requires to reformulate the systems of equations and affects the spectrum of choices for computational approaches that can be employed [70, 107]. Therefore, these issues influence the ability and capability of a specific monolithic algorithm in handling different coupling problems [129].

Nevertheless, the significant advantage of this approach is that there is no need for handling coupling between different solvers and dealing with its associated interface communication difficulties which may cause convergence problems.

1.3 Computational Approaches

Typically, there are some solid boundaries in CFD problems, e.g. walls in external and internal flows, and certainly in FSI problems. The mathematical modeling techniques and numerical methods for those flows and FSI problems can be broadly categorized based on the nature of the underlying meshes into body-conforming grid and non-conforming grid approaches, as shown schematically in Figure 1.1.

1.3.1 Body-Conforming Grid Methods

In body-conforming grid methods, the interface boundary coincides with the physical boundary of the solid body (cf. Figure 1.1(a)). The flow variables at the interface are parts of the solution, and grids need to conform to the interface. In the case of a FSI problem, since the structure deformation changes the interface location and velocity for the solid body, the fluid domain should move or deform to capture the new location or shape

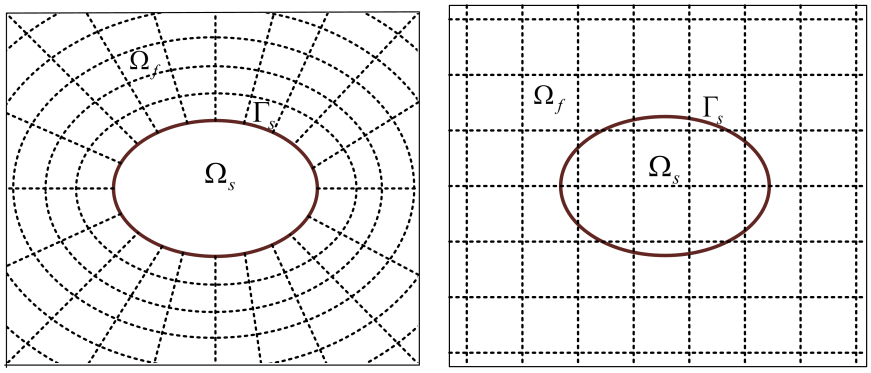

(a) (b)

Figure 1.1: (a) Schematic of a body in a fluid flow with body conforming mesh. (b) Schematic of a body in a fluid flow with body non-conforming mesh. Ω_s is the solid body, Ω_f is the fluid domain and Γ_s is the solid boundary. The outer rectangular frames are not representing the outer boundaries of the whole computational domains, but of the extracted parts.

of the structure and to track the interface. Advancing the solution in time, updating the mesh points in the fluid flow domain along with solid boundary movement or deformation is unavoidable in this approach. Since all the paths of the material (structure) points, including the moving boundary can be followed at all times, the treatment of the moving boundaries is rather straightforward from the Lagrangian viewpoint. However, in the fluid domain with the Eulerian viewpoint, the treatment of the moving boundary is not trivial and special methods are required to match the Eulerian description of the fluid motion with the Lagrangian description of the moving boundary. The main feature of body-conforming grid methods in FSI is that they operate on dynamic grids. The most commonly used approach is the Arbitrary Lagrangian-Eulerian (ALE) method [21]. ALE methods are prone to be constrained when it comes to problems involving bodies with complex geometry or undergoing large deformations.

1.3.2 Non-Conforming Grid Methods

In non-conforming grid methods, the governing equations are solved on a fixed background mesh (primarily Cartesian grids) and the presence of the solid body or the effect of the moving boundaries are taken into account (cf. Figure 1.1(b)). The most notable method among non-conforming grid methods is the immersed boundary method (IBM). In this approach, the interface location and the boundary conditions are imposed as constraints

on the governing equations or on nodes or cells near the interface, and the fluid and structure equations can be solved independently on their own corresponding grids without any re-meshing procedure [10]. The presence and the effect of the boundary can be treated as a diffused interface through a body-forcing term in the Navier-Stokes equations, e.g. Peskin's method [87], or as a sharp interface by proper modification of the solution variables in the vicinity of the immersed boundary [75].

Since in body-conforming grid methods the immersed boundaries coincide with grid lines, the boundary conditions are directly applied to the fluid flow governing equations. On the other hand, in non-conforming grid methods, the imposition of the boundary conditions needs to happen at the points which are not the physical boundary, which it is the primary drawback of this approach [75].

Since the IB methods employ Cartesian grids, they can easily reduce the number of floating point operations per grid point or grid cell. Additionally, they make the grid generation effortless which can be a cumbersome task for body-conforming grid methods for complex geometries. Therefore, the ease of handling complex geometries can be noted as a significant advantage of non-conforming grid methods compared to the body-conforming grid approach. Particularly, non-body conforming grid methods can handle moving boundaries with large deformation of the structure without requiring a sophisticated re-meshing strategy at each time step. Consequently, the use of non-conforming grid methods like IBM will influence the computational cost, simplicity and accuracy [75].

1.4 Application of Fluid-Structure Interaction

There are many highly elastic tissues in the human body. These tissues play a significant role in the functionality and physiology of the human body when the forces from internal fluid flow deform the tissues. Moreover, the deformation and displacement of the tissues in return affect the fluid flows inside the human body. The interaction between the fluid flow and the soft tissues involved in the human upper airways is an interesting biomechanical and biomedical application which can be studied. Disorders of the upper airways are often associated with respiratory syndromes. Among these, obstructive sleep apnea syndrome (OSAS) and snoring are closely related to the flow conditions in the upper airways.

1.4.1 Anatomy of Upper Airways

The respiratory system not only exchanges oxygen and carbon dioxide into and from the blood, but is also involved in sound production and transferring

fluids or solids into the digestive system. The respiratory system can be broadly divided into the upper and lower airways [103]. The upper airways which are considered in this study extends from the nostrils and the mouth to the larynx.

Figure 1.2 presents an overview of the human upper airways. The inhaled air enters from the nostrils and mouth opening and passes through the nasal and oral cavities into the lungs. The nasal cavity, which is the space between the floor of the skull and the roof of the mouth, is divided by the nasal septum into two halves. Airflow enters in each half from the outside through one of the two nose openings, known as the nostrils or the external nares. The two openings from the nasal cavity into the pharynx are the internal nares [110]. The first section of the mouth, known as the oral cavity, is the beginning of the digestive system and plays a significant role in communication. This space is bordered to the front and to the sides by the two alveolar arches, which contain the teeth and to the roof of the mouth. Toward the back it is bordered by the isthmus of the fauces which is a part of the oropharynx directly behind the oral cavity. The nasal and oral cavities are separated by the roof of the mouth known as the palate. The bony, rigid part of the palate located towards the front of the mouth is the hard palate. Directly attached to the hard palate is the soft palate, the fleshy, deformable part. It tapers down to a hanging, flapping piece of tissue called the uvula, the short tail end of the soft palate [110].

The airflow passing through nasal and oral cavities goes into the pharynx which is a fibromuscular tube connecting the nasal and oral cavities to the lower respiratory tract and the esophagus which is the digestive pathway. The pharynx can be divided into three parts namely the nasopharynx, the oropharynx, and the laryngopharynx [3]. The nasopharynx, which is the upper part of the pharynx, is the space between the internal nares and the soft palate and lies above the oral cavity. The oropharynx lying behind the oral cavity, extends from the soft palate to the level of the hyoid bone. The hyoid bone is located near the upper part of the epiglottis and is a small bone in the neck. The laryngopharynx which is the caudal [1] part of the pharynx lies below the hyoid bone. It lies inferior to the epiglottis and extends to the location where this common pathway separates into the larynx and esophagus [110]. The larynx is known as the voice box because the vocal sound is produced in this part. It consists of the essential parts for phonation such as the vocal folds, vestibular folds, and glottis. It is also the pathway conveying air from the pharynx to the lungs. The larynx extends from the upper border of the epiglottis to the trachea [28].

[1] Directed toward or situated in or near the tail or posterior part of the body.

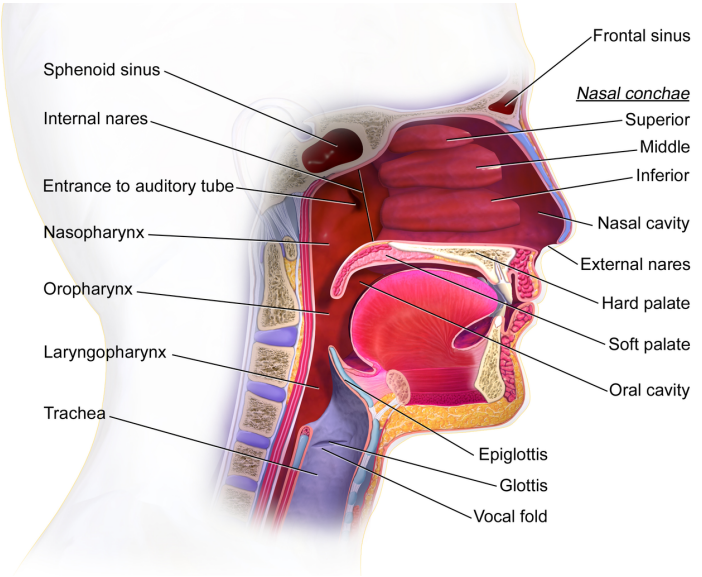

Figure 1.2: The human upper airways and its anatomical features in the sagittal plane [42].

1.4.2 Obstructive Sleep Apnea Syndrome

The obstructive sleep apnea syndrome (OSAS) is a disorder identified by recurring incidents of partial and complete pharyngeal airways collapse during sleep. These incidents can be classified into two groups, namely hypopnea when airflow is reduced by at least 30% and lasting at least 10 seconds and apnea when the pharyngeal airways are fully blocked and no airflow is passing [3, 25, 68].

OSAS is clinically recognized by the symptoms of daytime sleepiness, witnessed breathing interruptions, heavy snoring or awakenings because of gasping or choking in the presence of at least 5 obstructive respiratory events per hour of sleep [25].

The average frequencies of apnea or hypopnea events per hour gives the apnea-hypopnea Index (AHI) or Respiratory Disturbance Index (RDI) reflecting the severity of OSAS in individuals. The diagnosis of the severity of OSAS can be assessed by using these indices through a polysomnography, or sleep study, which measures the number of apneas and hypopneas during sleep. The definition of these indices have varied over time [25]. However, individuals with AHI $\leqslant$ 5, 5 $\leqslant$ AHI $\leqslant$ 15 and 15 $\leqslant$ AHI $\leqslant$ 30 have been classified as normal, mild and moderate OSAS, respectively. An AHI $\geqslant$ 30 is considered as severe OSAS [133].

Although the estimates and definitions often vary when dealing with prevalence, OSAS affects $2-4\%$ of the adult population [133], $9-24\%$ of the middle-age adults population and $1-4\%$ of children [133, 134] according to the reports. Since the diagnosis of OSAS has risen basically because of an increased awareness of this condition and an increased obesity among individuals, estimates show an increasing trend. Primarily due to anatomic differences between males and females particularly in the pharyngeal airway, men are more prone to suffer from OSAS [72]. In Norway, the prevalence of this syndrome is highlighted in a report by the Akershus Sleep Apnea Project [80], indicating that in the adult population (16302 individuals included) 16% having sleep apnea with severity of AHI $\geqslant 5$ and 8% having OSAS with AHI $\geqslant 15$.

1.4.2.1 Risk Factors for OSAS

There are several risk factors that could predispose an individual to OSAS. The risk factors include aging, male gender, obesity, familial genetics, smoking, alcohol consumption and craniofacial abnormalities [63]. Furthermore, there is increasing evidence that OSAS is an independent risk factor for an adverse cardiometabolic risk [2][73]. However, obesity is generally known as a primary factor for OSAS. About two-third of the patients with OSAS are more than 20% above their ideal body weight [73]. Being closely related to obesity, OSAS is a growing concern as obesity has become common and more severe.

1.4.3 Snoring

Snoring is sound generated by vibration of single or multiple soft tissues in the upper airways during sleep. According to estimates, 20-40% of the general population is affected by snoring which has become a prevalent disorder [133]. A population study among Australian men shows that up to 81% of the middle-aged men snore for more than 10% of their sleep time [8].

Aside from an unwanted noise during sleep, snoring could be a symptom of serious sleep disorders. Even though snoring does not necessarily mean that one is suffering from OSAS, estimates show that 10% of the snorers are at risk of OSAS [9] and OSAS sufferers typically have loud snoring [24].

Although the clinical implication of snoring is not completely clear, several types of snoring have been identified similar to OSAS. Palatal snoring happens with the majority of snorers when the soft palate is the main vibrating object. This type of snoring is classified by the mouth being either closed or open. When the mouth is closed, the inspiratory air from the nares

[2]Cardiometabolic risk refers to the chances of having diabetes, heart disease or stroke.

triggers the soft palate to oscillate and to temporarily obstruct the airway in the nasopharynx. In the case when the airflow travels through both upper and lower sides of the soft palate (both mouth and nose are open), the vibration of the soft palate between the tongue and the posterior pharyngeal wall can result in intermittent obstruction of the airways. Snoring may also come from a collapse of the tongue or the pharyngeal wall itself which is typically referred to as pharyngeal or non-palatal snoring. However, all these cases encompass the excited vibration of the flexible parts of the upper airways leading to a considerable noise generation. Palatal snoring is commonly loud with low frequencies compared to snoring generated from vibration of the tongue or the pharyngeal wall [1, 84, 95]. The louder noise and lower frequency of the soft palate oscillation compared to the other tissues is primarily caused by its lower size and its lower stiffness [49].

The nasal cavity and its coupling with other parts in the upper airways plays a significant role in snoring and sleep disorders. Since the obstructions during sleep increase the air resistance, the nasal airflow is altered and may trigger OSAS. Nevertheless, the correlation between nasal constrictions and the progress of sleep disorders has not been fully understood [90, 96].

1.4.4 Treatment of OSAS and Snoring

Nowadays, there are several OSAS and snoring treatment possibilities with varying invasiveness and effectiveness. Non-invasive treatments, particularly for patients with less severe cases, is the first line treatment option. This involves modifying their lifestyle, e.g., getting more exercise, controlling weight, cessation of smoking and sedatives prior to sleep [2].

The continuous positive airway pressure (CPAP) device is the standard tool for OSAS treatment that could be offered to all OSAS patients for being used during sleep [31]. The CPAP device placed next to the patient's bed continuously pumps air under pressure through a sealed nose- or face mask into the upper airways and lungs. Although it is an effective treatment in most cases, some patients cannot tolerate the use of this machine every night [137].

In more severe cases when non-invasive treatments have failed to provide a satisfactory effect, the only effective way to treat the condition is surgery. The nasal surgery, such as septoplasty or turbinectomy, aims to increase the airway volume in order to reduce the likelihood of airway collapse [105]. OSAS patients who cannot tolerate a CPAP device and reject surgery may consider oral appliances to treat their conditions. An oral appliances tries to displace the mandible forwards in order to prevent the tongue from collapsing backwards and to increase the airway volume [66].

1.5 Motivation and Objectives

The present study is motivated by the intention to further understand the flow dynamics in the human upper airways in order to explore computational methods as a tool in enhancing diagnosis and treatment for OSAS and snoring. Since clinical flow measurements in the upper airways are difficult to perform on patients, flow experiments have frequently been performed on mechanical models of the human airways. The vision is to establish computational models for the upper airways.

Considerable challenges are associated with setting up patient specific CFD models and validating FSI models. In addition, the computational costs in terms of computational time are significant in modeling the coupling between fluid flow and structural responses in the upper airways. Generally in computational modeling, mesh generation is an expensive process. Particularly, when the surface of a structure like the soft palate is fitted by body-conforming grids and experiences large deformations, extensive computations are required to frequently update the mesh. The main goals of the present dissertation have been detailed below.

- To develop a multi-block approach to decompose the computational domain and implement Message Passing Interface (MPI) into the existing fluid solver in our research group to increase the geometric flexibility for OSAS modeling and to take advantage of parallelization.
- To extend a high order finite difference method based on the ALE approach to FSI of a simplified model of the soft palate in the pharynx.
- To develop an immersed boundary method (IBM) for the compressible Navier–Stokes equations with complex and moving boundaries, particularly in the pharynx, employing high order finite difference operators in order to avoid the computational cost of the moving mesh and to improve the poor grid quality of body-fitted grids compressed or distorted by deformable structures. The motivating goal is to allow the simulation of computationally challenging moving boundary problems with no requirements of the user to interact with mesh construction or movement.

1.6 Outline and Contributions of the Thesis

The thesis is organized as follows. In Chapter 2, the compressible Navier–Stokes equations in perturbation form are presented. Since general geometries are treated by coordinate transformation, the formulation of the conservative compressible Navier–Stokes equations in transformed coordinates is

discussed here. A brief review of the strictly stable high order finite difference method used in this study is presented. Low pass filters and non-reflecting characteristic boundary conditions are outlined in this chapter. The implementation of the multi-block approach for our high order finite difference operators is explained.

In Chapter 3, the Euler–Bernoulli beam theory and the derivation of the equation of motion are discussed. Furthermore, we devise the modal analysis of the Euler-Bernoulli beam equation with different boundary conditions at the leading and trailing edges. The extension of the 1D structure model to a 2D inextensible plate model is presented. Numerical methods are presented to discretize the structural models.

In Chapter 4, a brief overview on the arbitrary Lagrangian–Eulerian (ALE) method is provided. In order to formulate the governing fluid flow equations for FSI, a time-dependent coordinate transformation is discussed here. The formulation of the ALE approach for the compressible Navier–Stokes equations in perturbation form is presented. The multi-block approach is shown to provide geometric flexibility for a moving mesh with the simplified model.

In Chapter 5, a general overview on the state-of-the-art immersed boundary methods is provided. The boundary treatment with IBM is formulated here. Two different reconstruction procedures are briefly discussed. Then, we show the implementation of the IBM for the high order finite difference operators used in this study. At the end, the treatment of the immersed boundary in the case of moving boundaries is discussed.

In Chapter 6, we give a brief overview on the papers listed in the thesis and present some selected results of our studies.

Chapter 7 summarizes the major conclusions and provides some suggestions for future work.

The following publications form the basis of this dissertation and are presented in the Appendix.

Journal Papers

- Paper I [53]: Khalili. M., Larsson, M., Müller, B., 2016. Interaction between a simplified soft palate and compressible viscous flow. Journal of Fluids and Structures 67, 85–105.

- Paper IV [55]: Khalili. M. E., Larsson, M., Müller, B., 2017. High order immersed boundary method for compressible viscous flows based on summation-by-parts operators. (*Submitted for journal publication*).

- Paper V [57]: Khalili. M. E., Larsson, M., Müller, B., 2017. Immersed boundary method for viscous compressible flows around moving bodies. (*Submitted for journal publication*).

Conference Papers

- Paper II [54]: Khalili. M. E., Larsson, M., Müller, B., 2017. Computational study of flow-induced oscillation of a simplified soft palate. Coupled Problems in Science and Engineering VII. CIMNE, pp. 582–593.

- Paper III [56]: Khalili. M. E., Larsson, M., Müller, B., 2017. Immersed boundary method for the compressible Navier-Stokes equations using high order summation-by-parts difference operators; 12th International Conference on Computational Fluid Dynamics In the Oil & Gas, Metallurgical and Process Industries. SINTEF, pp. 233–242.

CHAPTER 2

Mathematical Model of Fluid Flow

In this chapter, mathematical formulations of the fluid flow used in the simulations are presented in detail. Numerical methods employed to discretize the governing equations in space and time are discussed.

2.1 Compressible Navier–Stokes Equations

The compressible Navier–Stokes equations can be expressed in conservation form as

$$\frac{\partial \mathbf{U}}{\partial t} + \boldsymbol{\nabla} \cdot \mathcal{F}^c(\mathbf{U}) = \boldsymbol{\nabla} \cdot \mathcal{F}^v(\mathbf{U}, \boldsymbol{\nabla}\mathbf{U}), \tag{2.1}$$

where $\mathbf{U}$, the vector of conservative variables, $\mathcal{F}^c(\mathbf{U})$, the inviscid flux tensor and $\mathcal{F}^v(\mathbf{U}, \boldsymbol{\nabla}\mathbf{U})$, the viscous flux tensor are defined as

$$\mathbf{U} = \begin{pmatrix} \rho \\ \rho\mathbf{u} \\ \rho E \end{pmatrix},$$

$$\mathcal{F}^c(\mathbf{U}) = \begin{pmatrix} \rho\mathbf{u} \\ \rho\mathbf{u}\mathbf{u} \\ \rho H\mathbf{u} \end{pmatrix} + p \begin{pmatrix} 0 \\ \mathbf{I} \\ 0 \end{pmatrix},$$

$$\mathcal{F}^v(\mathbf{U}, \boldsymbol{\nabla}\mathbf{U}) = \begin{pmatrix} 0 \\ \boldsymbol{\tau} \\ \boldsymbol{\tau} \cdot \mathbf{u} + \kappa \boldsymbol{\nabla} T \end{pmatrix},$$

where $\rho, \rho\mathbf{u}, \rho E$ denote density, momentum density and total energy density, respectively. $\mathbf{I}$ stands for the unit tensor. The viscous stress tensor for a Newtonian fluid under Stokes' hypothesis is defined by $\boldsymbol{\tau} = \mu(\boldsymbol{\nabla}\mathbf{u} + (\boldsymbol{\nabla}\mathbf{u})^T) -$

$\frac{2}{3}\mu\boldsymbol{\nabla}\cdot\mathbf{u}\,\mathbf{I}$. The equations of state for perfect gas constitute a reliable thermodynamic model for many gases under diverse conditions, particularly for air at standard conditions. Thereby, the pressure is related to the internal energy $p=(\gamma-1)(\rho E-\frac{1}{2}\rho|\mathbf{u}|^2)$ with the ratio of specific heats $\gamma=\frac{c_p}{c_v}=1.4$, c_p and c_v are the specific heats at constant pressure and constant volume, respectively. The viscosity coefficient μ is determined from the Sutherland law $\mu(T)=C_1\frac{T^{1.5}}{T+C_2}$ where the parameters $C_1=1.458\times10^{-6}\mathrm{kg/(msK^{0.5})}$ and $C_2=110.4\mathrm{K}$ for air at standard conditions. The heat conduction coefficient κ is derived by taking into account the constant Prandtl number $\mathrm{Pr}=0.72$ and thus $\kappa=\frac{c_p}{\mathrm{Pr}}\mu$.

2.1.1 Perturbation Formulation

Since in compressible low Mach number flows, the perturbation variables $\mathbf{U}'$ with respect to a reference state $\mathbf{U_0}$ are small, cancellation errors occur when discretizing the Navier–Stokes equations. For instance, the pressure perturbations p' are much smaller than the stagnation pressure p_0, i.e. $p=p_0+p'$ and $|p'|\ll p_0$. Cancellation errors can be minimized by discretizing $\frac{\partial p'}{\partial x}$ rather than $\frac{\partial p}{\partial x}$ [106]. Thus, the perturbation formulation is employed in order to minimize cancellation errors while discretizing the Navier–Stokes equations for compressible low Mach number flow [79, 106].

With regard to this concept, the conservative variables are expressed as

$$\mathbf{U}(\mathbf{x},t)=\mathbf{U_0}(\mathbf{x},t)+\mathbf{U}'(\mathbf{x},t). \tag{2.2}$$

Generally, $\mathbf{U_0}$ and $\mathbf{U}$ are required to satisfy Eq. (2.1). The reference flow state $\mathbf{U_0}$ may be chosen not to be constant, but to depend on $\mathbf{x}$ and t as an unsteady base flow [78].

For the chosen reference flow state $\mathbf{U}_0=(\rho_0,(\rho\mathbf{u})_0,(\rho E)_0)^T$, the perturbed conservative variables $\mathbf{U}'=\mathbf{U}-\mathbf{U_0}=(\rho',(\rho\mathbf{u})',(\rho E)')^T$ can be defined. The Navier–Stokes equations (2.1) in perturbation form [78] can generally be expressed as

$$\frac{\partial\mathbf{U}'}{\partial t}+\boldsymbol{\nabla}\cdot\mathcal{F}^{c'}(\mathbf{U}',\mathbf{U_0})=\boldsymbol{\nabla}\cdot\mathcal{F}^{v'}(\mathbf{U}',\boldsymbol{\nabla}\mathbf{U}',\mathbf{U_0},\boldsymbol{\nabla}\mathbf{U_0}), \tag{2.3}$$

with the perturbed inviscid flux tensor

$$\mathcal{F}^{c'}(\mathbf{U}',\mathbf{U_0})=\begin{pmatrix}(\rho\mathbf{u})'\\((\rho\mathbf{u})_0+(\rho\mathbf{u})')\,\mathbf{u}'+(\rho\mathbf{u})'\mathbf{u}_0\\((\rho H)_0+(\rho H)')\,\mathbf{u}'+(\rho H)'\mathbf{u}_0\end{pmatrix}+p'\begin{pmatrix}0\\\mathbf{I}\\0\end{pmatrix},$$

where the perturbed velocity, pressure and total enthalpy are

$$\mathbf{u}' = \frac{(\rho\mathbf{u})_0 + (\rho\mathbf{u})'}{\rho_0 + \rho'} - \frac{(\rho\mathbf{u})_0}{\rho_0},$$

$$p' = (\gamma - 1)\Big((\rho E)' - \frac{1}{2}\Big((\rho\mathbf{u}') \cdot (\mathbf{u_0} + \mathbf{u}') + (\rho\mathbf{u})_0 \cdot \mathbf{u}' \Big) \Big),$$

$$(\rho H)' = (\rho E)' + p'.$$

The perturbed viscous flux tensor is defined as

$$\mathcal{F}^{v'}(\mathbf{U}', \boldsymbol{\nabla}\mathbf{U}', \mathbf{U_0}, \boldsymbol{\nabla}\mathbf{U_0}) = \begin{pmatrix} 0 \\ \boldsymbol{\tau}' \\ \boldsymbol{\tau}' \cdot (\mathbf{u}_0 + u') + \boldsymbol{\tau}_0 \cdot \mathbf{u}' + (\kappa_0 + \kappa')\boldsymbol{\nabla}T' + \kappa'\boldsymbol{\nabla}T_0 \end{pmatrix},$$

where

$$\boldsymbol{\tau}' = (\mu_0 + \mu')(\boldsymbol{\nabla}\mathbf{u}' + (\boldsymbol{\nabla}\mathbf{u}')^T) - \frac{2}{3}(\mu_0 + \mu')\boldsymbol{\nabla} \cdot \mathbf{u}'\ \mathbf{I} + \mu'(\boldsymbol{\nabla}\mathbf{u_0} + (\boldsymbol{\nabla}(\mathbf{u_0})^T) - \frac{2}{3}\mu'\boldsymbol{\nabla} \cdot \mathbf{u_0}\ \mathbf{I},$$

$$\mu' = \mu(T_0 + T') - \mu(T_0),$$

$$T' = \frac{\frac{p'}{R} - \rho' T_0}{\rho_0 + \rho'},$$

Here, R is the specific gas constant and μ is determined from the Sutherland law with the non-dimensional Sutherland constant $S_c = \frac{110.4K}{T_0}$,

$$\frac{\mu}{\mu_0} = \Big(\frac{T}{T_0}\Big)^{1.5}\Big(\frac{1 + S_c}{\frac{T}{T_0} + S_c}\Big),$$

$$\kappa' = \kappa(T_0 + T') - \kappa(T_0).$$

Since in the perturbation form Eq. (2.3) the large contributions $\mathbf{U}_0$ from $\frac{\partial \mathbf{U}}{\partial t}$ and p_0 from the momentum flux are removed, it allows discretizations in conservative form while minimizing cancellation errors for low Mach number flows [78, 79, 106].

For the chosen constant stagnation flow state $\mathbf{U}_0 = (\rho_0, \mathbf{0}, (\rho E)_0)^T$, equations (2.3) are simplified. The conservative form of the 2D compressible

Navier–Stokes equations in Cartesian coordinates in perturbation formulation can be expressed as

$$\mathbf{U}'_t + \mathbf{F}^{c\prime}{}_x + \mathbf{G}^{c\prime}{}_y = \mathbf{F}^{v\prime}{}_x + \mathbf{G}^{v\prime}{}_y, \tag{2.4}$$

where the subscripts in (2.4) denote derivatives, i.e. $\mathbf{U}'_t = \frac{\partial \mathbf{U}'}{\partial t}, \mathbf{F}'^{c}_{\ x} = \frac{\partial \mathbf{F}'^{c}}{\partial x}$, etc. The conservative perturbation variables $\mathbf{U}'$ are defined by

$$\begin{pmatrix} \rho' \\ (\rho u)' \\ (\rho v)' \\ (\rho E)' \end{pmatrix} = \begin{pmatrix} \rho \\ (\rho u) \\ (\rho v) \\ \rho E \end{pmatrix} - \begin{pmatrix} \rho_0 \\ 0 \\ 0 \\ (\rho E)_0 \end{pmatrix},$$

and the inviscid ($\mathbf{F}^{c\prime}$, $\mathbf{G}^{c\prime}$) and viscous perturbation flux vectors ($\mathbf{F}^{v\prime}$, $\mathbf{G}^{v\prime}$) are defined by $\mathbf{F}^{c\prime} = \mathbf{F}^{c}(\mathbf{U}) - \mathbf{F}^{c}(\mathbf{U_0})$, etc.

$$\mathbf{F}^{c\prime} = \begin{pmatrix} (\rho u)' \\ (\rho u)'u' + p' \\ (\rho v)'u' \\ ((\rho H)_0 + (\rho H)')u' \end{pmatrix}, \quad \mathbf{G}^{c\prime} = \begin{pmatrix} (\rho v)' \\ (\rho u)'v' \\ (\rho v)'v' + p' \\ ((\rho H)_0 + (\rho H)')v' \end{pmatrix},$$

$$\mathbf{F}^{v\prime} = \begin{pmatrix} 0 \\ \tau'_{xx} \\ \tau'_{xy} \\ u'\tau'_{xx} + v'\tau'_{xy} + \kappa T'_x \end{pmatrix}, \quad \mathbf{G}^{v\prime} = \begin{pmatrix} 0 \\ \tau'_{yx} \\ \tau'_{yy} \\ u'\tau'_{yx} + v'\tau'_{yy} + \kappa T'_y \end{pmatrix}.$$

2.1.2 Non-Dimensional Variables

For convenience the variables in the 2D Navier–Stokes equations (2.4) are non-dimensionalized with stagnation density ρ_0, stagnation speed of sound c_0, a characteristic length L and stagnation pressure $p_0 = \frac{\rho_0 c_0^2}{\gamma}$ as reference values. The non-dimensional quantities are defined as follows

$$\begin{aligned} &t^* = \tfrac{tc_0}{L}, x^* = \tfrac{x}{L}, y^* = \tfrac{y}{L}, \rho^* = \tfrac{\rho}{\rho_0}, u^* = \tfrac{u}{c_0}, v^* = \tfrac{v}{c_0}, \\ &T^* = \tfrac{T}{T_0}, p^* = \tfrac{p}{\gamma p_0}, E^* = \tfrac{E}{c_0^2}, (\rho E)^* = \tfrac{\rho E}{\rho_0 c_0^2}. \end{aligned} \tag{2.5}$$

A special choice is made for specifying the non-dimensional viscosity μ^* and the non-dimensional heat transfer κ^* as

$$\mu^* = \frac{1}{\mathrm{Re}_0}\frac{\mu}{\mu_0}, \quad \kappa^* = \frac{1}{(\gamma-1)\mathrm{Pr}_0\mathrm{Re}_0}\frac{\kappa}{\kappa_0}, \tag{2.6}$$

where the stagnation Reynolds and Prandtl numbers are defined by

$$\mathrm{Re}_0 = \frac{\rho_0 c_0 L}{\mu_0}, \quad \mathrm{Pr}_0 = \frac{c_p \mu_0}{\kappa_0}. \tag{2.7}$$

Employing this choice, the non-dimensional and dimensional forms of the compressible Navier–Stokes equations (2.4) coincide.

2.1.3 Coordinate Transformation

In order to perform computations for general geometries, the Cartesian coordinates (x, y) are transformed from the physical domain into curvilinear coordinates (ξ, η) in the computational domain. The coordinate transformation can be expressed by the following relations

$$\begin{aligned} \xi &= \xi(x, y), \\ \eta &= \eta(x, y). \end{aligned} \tag{2.8}$$

The chain rule for partial differentiation yields the following expressions

$$\frac{\partial}{\partial x} = \xi_x \frac{\partial}{\partial \xi} + \eta_x \frac{\partial}{\partial \eta}, \tag{2.9}$$

$$\frac{\partial}{\partial y} = \xi_y \frac{\partial}{\partial \xi} + \eta_y \frac{\partial}{\partial \eta}, \tag{2.10}$$

where the subscript notation is used to denote partial derivatives, i.e., $\xi_x = \frac{\partial \xi}{\partial x}$, $\eta_y = \frac{\partial \eta}{\partial y}$, etc.

Reversing the role of the independent variables, i.e., $x = x(\xi, \eta)$ and $y = y(\xi, \eta)$, it can be concluded that

$$\begin{pmatrix} \xi_x & \xi_y \\ \eta_x & \eta_y \end{pmatrix} = \begin{pmatrix} x_\xi & x_\eta \\ y_\xi & y_\eta \end{pmatrix}^{-1} = J \begin{pmatrix} y_\eta & -x_\eta \\ -y_\xi & x_\xi, \end{pmatrix} \tag{2.11}$$

where J, the Jacobian defined as the ratio of the areas (volume in 3D) in the computational domain to the physical domain, is defined as

$$J = \frac{\partial(\xi, \eta)}{\partial(x, y)} = \frac{1}{x_\xi y_\eta - y_\xi x_\eta}. \tag{2.12}$$

In this way, the transformed 2D compressible Navier–Stokes equations in perturbation form are expressed as

$$\hat{\mathbf{U}}'_t + \hat{\mathbf{F}}'_\xi + \hat{\mathbf{G}}'_\eta = 0, \tag{2.13}$$

where

$$\hat{\mathbf{U}}' = J^{-1} \mathbf{U}',$$

$$\hat{\mathbf{F}}' = J^{-1}\Big(\xi_x(\mathbf{F}^{c\prime} - \mathbf{F}^{v\prime}) + \xi_y(\mathbf{G}^{c\prime} - \mathbf{G}^{v\prime})\Big),$$

$$\hat{\mathbf{G}}' = J^{-1}\Big(\eta_x(\mathbf{F}^{c\prime} - \mathbf{F}^{v\prime}) + \eta_y(\mathbf{G}^{c\prime} - \mathbf{G}^{v\prime})\Big).$$

The chain rule for partial differentiation provides the expressions for Cartesian derivatives in the viscous flux vectors $\mathbf{F}^{v\prime}$ and $\mathbf{G}^{v\prime}$, e.g. $u'_x = u'_\xi \xi_x + u'_\eta \eta_x$ and $u'_y = u'_\xi \xi_y + u'_\eta \eta_y$.

2.2 Numerical Methods for Compressible Navier–Stokes Equations

2.2.1 High Order Finite Difference Method

The high order finite difference method based on summation-by-parts (SBP) operators [40, 41, 111] is employed for space discretization of the compressible Navier–Stokes equations. This approach is based on the energy method, which permits to derive well-posedness for the continuous problem and to guarantee stability for the discrete problem. Both first and second spatial derivatives can be approximated by high order difference operators with built-in stability.

2.2.1.1 Energy Method

The energy method is a technique to prove sufficient conditions for well-posedness of partial differential equations (PDE) and stability of difference methods with general boundary conditions [40]. To demonstrate the energy method, we apply the procedure to a simplified PDE, that is, rather than analysing the full Navier–Stokes equations in this section, we only focus on the 1D convection-diffusion equation as a model equation.

$$\begin{aligned} &u_t + a u_x = b u_{xx}, \quad 0 \le x \le 1, \quad t \ge 0, \\ &u(x,0) = f(x), \\ &u(0,t) = u(1,t) = g(t) = 0, \end{aligned} \tag{2.14}$$

where a and b are assumed to be constant and positive, and u is the dependent variable. The L_2 scalar product for two real functions v and w is defined by

$$(v,w) = \int_0^1 v(x)w(x)dx, \tag{2.15}$$

which then defines the L_2 norm of the continuous solution at time t and energy $E(t) = \|u(\cdot,t)\|^2 = (u,u)$. Integration by parts states

$$(v, w_x) = v(1)w(1) - v(0)w(0) - (v_x, w).$$

The energy method uses the definition of energy, product rule, PDE (2.14), integration by parts, $\|u_x\|^2 \geq 0$, and the boundary conditions (2.14) to arrive at

$$\begin{aligned}
&\tfrac{dE}{dt} = \tfrac{d}{dt}\|u(\cdot,t)\|^2 = (u_t,u) + (u,u_t) \\
&\quad = (-au_x + bu_{xx}, u) + (u, -au_x + bu_{xx}) \\
&\quad = -a\Big(u^2(1,t) - u^2(0,t)\Big) + 2b\Big(u(1,t)u_x(1,t) - u(0,t)u_x(0,t)\Big) \\
&\quad -2b(u_x,u_x) \leq -a\Big(u^2(1,t) - u^2(0,t)\Big) \\
&\quad +2b\Big(u(1,t)u_x(1,t) - u(0,t)u_x(0,t)\Big) = 0,
\end{aligned} \tag{2.16}$$

which yields a non-growing solution, i.e. $E(t) \leq E(0) = \|f(x)\|^2$. Thus, the energy is bounded by the initial condition.

2.2.1.2 Summation-By-Parts Operators

The SBP operators are constructed to guarantee a discrete energy estimate similar to the continuous energy estimate above. The basis of getting such an energy estimate is to satisfy integration by parts in the discrete sense called Summation-by-parts (SBP) property [40, 113]. To outline this technique for model problem (2.14), we consider $u_j = u_j(t)$ the numerical solution of the convection-diffusion equation at grid point $x_j = jh, j = 0, ..., N$, with grid spacing $h = \frac{1}{N}$. The solution vector containing the solution at the discrete grid points is $\mathbf{u} = (u_0(t), u_1(t), ..., u_N(t))^T$. Using a difference operator Q approximating the first derivative in space and using it twice, i.e. QQ, to approximate $\frac{\partial^2}{\partial x^2}$, the semi-discrete form of the model equation can be expressed as

$$\tfrac{d\mathbf{u}}{dt} = -aQ\mathbf{u} + bQQ\mathbf{u}, \quad u_j(0) = f(x_j). \tag{2.17}$$

The discrete scalar product and corresponding norm and energy can be defined by

$$\begin{aligned}
&(\mathbf{u},\mathbf{v})_h = h\mathbf{u}^T H\mathbf{v}, \\
&E_h(t) = \|\mathbf{u}\|_h^2 = (\mathbf{u},\mathbf{u})_h,
\end{aligned} \tag{2.18}$$

where H is a diagonal and positive definite matrix defined by

$$H = \mathrm{diag}(H_L, I, H_R). \tag{2.19}$$

The SBP property is satisfied by the difference operator Q, if

$$(\mathbf{u}, Q\mathbf{v})_h = u_N v_N - u_0 v_0 - (Q\mathbf{u},\mathbf{v})_h, \tag{2.20}$$

or if Q can be written on the form $hQ = H^{-1}P$ for P satisfying

$$P + P^T = E_N - E_0 = \mathrm{diag}(-1, 0, ..., 0, 1), \tag{2.21}$$

where $E_0 = \mathrm{diag}(1, 0, ..., 0)$ and $E_N = \mathrm{diag}(0, 0, ..., 1)$. Using the semi-discrete equation (2.17), the definition of energy, product rule, integration by parts and $\|u_x\|^2 \geq 0$, the energy estimate for the semi-discrete problem can be obtained as

$$\begin{aligned}\frac{dE}{dt} = \frac{d}{dt}\|u(\cdot,t)\|^2 &= (u_t, u)_h + (u, u_t)_h \\ &= (-aQu + bQQu, u)_h + (u, -aQu + bQQu)_h \\ &= -a\Big(u_N^2 - u_0^2\Big) + 2b\Big(u_N(Qu)_N - u_0(Qu)_0\Big) \\ &-2b(Qu, Qu)h \leq -a\Big(u_N^2 - u_0^2\Big) + 2b\Big(u_N(Qu)_N - u_0(Qu)_0\Big).\end{aligned} \tag{2.22}$$

We would get non-growing energy in time if the homogeneous boundary conditions could directly be imposed in (2.22). However, this will change the difference operator Q such that its SBP property might be lost. To avoid this problem, boundary conditions are weakly imposed by the simultaneous approximation term (SAT) technique [14, 40]. A first derivative SBP operator with diagonal quadrature matrix H in (2.18) is of order $\mathcal{O}(h^{2s})$ accurate central difference operator which is of order $\mathcal{O}(h^s)$ accurate at and near boundaries, where $s = 1, 2, 3, 4$. Such an SBP operator is globally $\mathcal{O}(h^{s+1})$ accurate.

2.2.2 Present SBP Operators for Compressible Navier–Stokes Equations

A globally fourth order SBP operator is employed in this study to discretize the first ξ- and η- derivatives in Eq. (2.13). Therefore, the SBP operators for $\frac{\partial}{\partial\xi}$ and $\frac{\partial}{\partial\eta}$ correspond to the standard sixth order central difference operator in the interior, but degrade to third order accuracy near the boundary, resulting in fourth order global accuracy [40, 111]. The difference operator Q is written as

$$Q = \frac{1}{h}\begin{pmatrix}
q_{1,1} & q_{1,2} & q_{1,3} & q_{1,4} & q_{1,5} & q_{1,6} & 0 & \dots & & & & \\
q_{2,1} & 0 & q_{2,3} & q_{2,4} & q_{2,5} & q_{2,6} & 0 & \dots & & & & \\
q_{3,1} & q_{3,2} & 0 & q_{3,4} & q_{3,5} & q_{3,6} & 0 & \dots & & & & \\
q_{4,1} & q_{4,2} & q_{4,3} & 0 & q_{4,5} & q_{4,6} & q_{4,7} & 0 & \dots & & & \\
q_{5,1} & q_{5,2} & q_{5,3} & q_{5,4} & 0 & q_{5,6} & q_{5,7} & q_{5,8} & 0 & \dots & & \\
q_{6,1} & q_{6,2} & q_{6,3} & q_{6,4} & q_{6,5} & 0 & q_{6,7} & q_{6,8} & q_{6,9} & 0 & \dots & \\
 & \dots & 0 & \frac{-1}{60} & \frac{3}{20} & \frac{-3}{4} & 0 & \frac{3}{4} & \frac{-3}{20} & \frac{1}{60} & 0 & \dots \\
 & & & \ddots & \ddots & \ddots & \ddots & \ddots & \ddots & \ddots & \ddots & \ddots
\end{pmatrix}, \tag{2.23}$$

where $q_{i,j} \in \mathbb{R}, i = 1, \dots 6$ and $j = 1, \dots, 9$ are coefficients obtained by the order conditions and the SBP property [40, 41, 111].

Second derivatives of the viscous parts of $\hat{\mathbf{F}}_\xi{}'$ and $\hat{\mathbf{G}}_\eta{}'$ Eq. (2.13) are approximated here by applying the SBP operator for the first derivatives operator twice.

2.2.3 Time Integration

The compressible Navier–Stokes equations discretized in space by a finite difference method can be considered as a system of ordinary differential equations (ODE), i.e.

$$\frac{d\mathbf{U}'}{dt} = \mathcal{F}(t, \mathbf{U}'), \tag{2.24}$$

where

$$\mathcal{F}(t, \mathbf{U}') = -J(Q_\xi \hat{\mathbf{F}}' + Q_\eta \hat{\mathbf{G}}'), \tag{2.25}$$

Q_ξ and Q_η are the SBP operators in the ξ- and η- directions, respectively, $\mathbf{U}'$, $\hat{\mathbf{F}}'$ and $\hat{\mathbf{G}}'$ are defined in (2.13).

The classical fourth order explicit Runge–Kutta method is used for discretizing the compressible Navier–Stokes equations in time. The solution is advanced from the time level n to the level $n+1$ as

$$\mathbf{U}'^{n+1} = \mathbf{U}'^{n} + \frac{\Delta t}{6}(k_1 + 2k_2 + 2k_3 + k_4), \tag{2.26}$$

where in the 4 Runge–Kutta stages $k_i, i = 1, ..., 4$

$$k_1 = \mathcal{F}(t^n, \mathbf{U}'^n),$$

$$k_2 = \mathcal{F}(t^n + \frac{\Delta t}{2}, \mathbf{U}'^n + \frac{\Delta t}{2}k_1),$$

$$k_3 = \mathcal{F}(t^n + \frac{\Delta t}{2}, \mathbf{U}'^n + \frac{\Delta t}{2}k_2),$$

$$k_4 = \mathcal{F}(t^n + \Delta t, \mathbf{U}'^n + \Delta t k_3).$$

2.2.4 Explicit Filters

Waves with wave number $k = \frac{\pi}{h}$, where h is the grid spacing, are not damped by the viscous terms when applying the standard sixth order central difference operator for the first derivative twice. Studies by [128] provide strong evidence that those waves can be successfully damped by applying spatial filters when solving the transformed compressible Navier–Stokes equations (2.13) by high order finite difference methods. To suppress spurious high wavenumber oscillations, a p^{th} (p even, here $p = 6$) order explicit filter is

applied by modifying the numerical solution $\mathbf{U'}_{i,j}^{n+1}$ at the end of the Runge–Kutta stages according to

$$\tilde{\mathbf{U}}'^{n+1}_{i,j} = \mathbf{U}'^{n+1}_{i,j} - \left(D_\xi^{(p)} \mathbf{U}' + D_\eta^{(p)} \mathbf{U}' \right)_{i,j}^{n+1}, \tag{2.27}$$

where $D_\xi^{(p)}$ and $D_\eta^{(p)}$ represent scaled central finite difference approximations of the p^{th} $\xi-$ and $\eta-$ derivatives, receptively. The difference operator $D_\xi^{(p)}$ is defined by

$$(D_\xi^{(p)} \mathbf{U}')_{i,j} = \frac{(-1)^{p/2}}{2^p} \delta_\xi^p \mathbf{U}'_{i,j}, \tag{2.28}$$

which is a p^{th} order approximation of $\frac{(-1)^{p/2}}{2^p} \Delta\xi^p \frac{\partial^p \mathbf{U}'(i\Delta\xi, j\Delta\eta)}{\partial \xi^p}$. The difference operator δ_ξ^p in (2.28) is defined by applying δ_ξ^2 $\frac{p}{2}$ times, where $\delta_\xi^2 \mathbf{U}'_{i,j} = \mathbf{U}'_{i+1,j} - 2\mathbf{U}'_{i,j} + \mathbf{U}'_{i-1,j}$. The same procedure is used for the $\eta-$direction, i.e., $D_\eta^{(p)}$ in (2.27). The coefficient $\frac{(-1)^{p/2}}{2^p}$ is chosen such that the wave with wave number $k_{xi} = \frac{\pi}{\Delta xi}$ is annihilated. Here, $p = 6$ for the sixth order central finite difference operator. Low pass filters are discussed in [79, 127] and their boundary treatment in [79].

2.2.5 Non-Reflecting Characteristic Boundary Conditions

Non-reflecting characteristic boundary conditions are used at the inflow and outflow boundaries to minimize wave reflections. The Navier–Stokes characteristic boundary conditions (NSCBC) developed by [92] are employed to approximate incoming waves. The main idea in the NSCBC approach is to determine the amplitude of the waves entering into the computational domain. The determination of the amplitudes is built on the assumptions that the flow is one-dimensional and inviscid, i.e., local one-dimensional inviscid (LODI) relations. Since fully non-reflecting conditions may lead to an ill-posed problem [92], this approach is partially reflecting.

LODI relations associate the temporal evolution of the primitive variables (ρ, u, v, p), i.e., density, velocity components and pressure, to the wave amplitudes $\mathcal{L}_i, i = 1, ..., 4$. The wave amplitudes $\mathcal{L}_1$ and $\mathcal{L}_4$ correspond to the left and right travelling acoustic waves with the wave speed $(u - c)$ and $(u + c)$, respectively, where c is the speed of sound. $\mathcal{L}_2$ is related to the entropy wave of wave speed u and $\mathcal{L}_3$ the first vorticity wave of wave speed u. LODI relations in transformed coordinates [79] are expressed as

$$J^{-1}\begin{pmatrix}1&0&0&0\\0&\rho&0&0\\0&0&\rho&0\\0&0&0&\frac{1}{\gamma-1}\end{pmatrix}\begin{pmatrix}\rho_t\\u_t\\v_t\\p_t\end{pmatrix}+ \begin{pmatrix}\hat{U}&\rho\hat{\xi}_x&\rho\hat{\xi}_y&0\\0&\hat{U}\rho&0&\hat{\xi}_x\\0&0&\hat{U}\rho&\hat{\xi}_y\\0&\frac{\gamma p}{\gamma-1}\hat{\xi}_x&\frac{\gamma p}{\gamma-1}\hat{\xi}_y&\hat{U}\frac{1}{\gamma-1}\end{pmatrix}\begin{pmatrix}\rho_\xi\\u_\xi\\v_\xi\\p_\xi\end{pmatrix}=0, \tag{2.29}$$

where $\hat{\xi}_x$ and $\hat{\xi}_y$ denote $J^{-1}\xi_x$ and $J^{-1}\xi_y$, respectively, and $\hat{U}=\hat{\xi}_x u+\hat{\xi}_y v$.

Employing characteristic analysis, the LODI system can be recast as

$$J^{-1}\begin{pmatrix}\rho_t\\u_t\\v_t\\p_t\end{pmatrix}+\begin{pmatrix}\mathcal{L}_2+\frac{|\hat{\xi}|}{c}(\mathcal{L}_4-\mathcal{L}_1)\\-\hat{\xi}_y\mathcal{L}_3+\frac{|\hat{\xi}_x|}{\rho}(\mathcal{L}_4+\mathcal{L}_1)\\\hat{\xi}_x\mathcal{L}_3+\frac{|\hat{\xi}_y|}{\rho}(\mathcal{L}_4+\mathcal{L}_1)\\c|\hat{\xi}|(\mathcal{L}_4-\mathcal{L}_1)|\end{pmatrix}=0, \tag{2.30}$$

where $|\hat{\xi}|=\sqrt{\hat{\xi}_x^2+\hat{\xi}_y^2}$ and the wave amplitudes $\mathcal{L}_i,\ i,1,...,4$ are obtained as

$$\begin{pmatrix}\mathcal{L}_1\\\mathcal{L}_2\\\mathcal{L}_3\\\mathcal{L}_4\end{pmatrix}=\begin{pmatrix}\frac{\rho}{2}\frac{\hat{\xi}_x}{|\hat{\xi}|^2}u_\xi+\frac{\rho}{2}\frac{\hat{\xi}_y}{|\hat{\xi}|^2}v_\xi-\frac{p_\xi}{2c|\hat{\xi}|}\\\rho_\xi-\frac{p_\xi}{c^2}\\-\frac{\hat{\xi}_y}{|\hat{\xi}|^2}u_\xi+\frac{\hat{\xi}_x}{|\hat{\xi}|^2}v_\xi\\\frac{\rho}{2}\frac{\hat{\xi}_x}{|\hat{\xi}|^2}u_\xi+\frac{\rho}{2}\frac{\hat{\xi}_y}{|\hat{\xi}|^2}v_\xi+\frac{p_\xi}{2c|\hat{\xi}|}\end{pmatrix}. \tag{2.31}$$

Eqs. (2.30) and (2.31) provide a method to compute the incoming wave amplitude to be imposed at the boundaries. At the inflow, a fixed velocity and temperature are imposed. The imposed velocity at the inlet requires the incoming acoustic wave amplitude to be equal, but opposite to the outgoing acoustic wave amplitude $\mathcal{L}_4=-\mathcal{L}_1$. As the inlet temperature is fixed, LODI relations (2.29) give an estimate of the entropy wave amplitude as

$$\begin{aligned}\mathcal{L}_2&=(\gamma-1)\tfrac{|\hat{\xi}|}{c}(\mathcal{L}_4-\mathcal{L}_1)\\&=-2(\gamma-1)\tfrac{|\hat{\xi}|}{c}\mathcal{L}_1.\end{aligned} \tag{2.32}$$

The density ρ is computed at the inlet boundary from the continuity equation.Imposing a constant pressure at the outlet requires $\mathcal{L}_1=\mathcal{L}_4$. To keep the reflections low and the pressure close to atmospheric pressure, the incoming wave amplitude is set to

$$\mathcal{L}_1=\mathcal{L}_1^{\text{exact}}+(-2c\xi_x)^{-1}K(p-p_{\text{atm}}), \tag{2.33}$$

where K is a relaxation coefficient and $\mathcal{L}_1^{\text{exact}}$ is the exact value of $\mathcal{L}_1$, obtained as

$$\mathcal{L}_1^{\text{exact}} = \Big(- \frac{U}{2c|\hat{\xi}|\xi_x} + \frac{1}{2\xi_x} \Big) p_x^{\text{exact}}(-2c\xi_x), \tag{2.34}$$

which $p_x^{\text{exact}} = -2\mu \frac{U_{max}}{l^2}$.

Rudy and Strikwerda proposed the relaxation coefficient as $K = \sigma(1 - \text{Ma}^2)(c/L_t)$, where Ma is the Mach number, c the sound speed, L_t the total length of the domain and σ a constant value [97]. The optimum value $\sigma = 0.25$ derived by [97] is employed. For reverse flow (negative velocity in x-direction) at the outlet, $\mathcal{L}_1$, $\mathcal{L}_2$ and $\mathcal{L}_3$ are set to zero.

2.3 Domain Decomposition

A multi-block grid is generated through a domain decomposition procedure. First, the computational grid of the whole physical domain is considered as a single block. Then, the domain is divided into several sub-domains (or blocks) by selecting all the nodes lying in each sub-domain with specified block boundaries. Next, each sub-domain is constructed individually. The idea behind the multi-block approach is to obtain a geometric flexibility for structured grids and to speed up the computations. Instead of solving the governing equations for the whole domain as one block, the solution is broken down into several pieces (blocks), in which the solution for one Runge–Kutta stage can be computed separately. Distributing the domain across several computational nodes requires less memory allocated to store the data in each node than to store the data in a single node for the whole grid.

The decomposition of the computational domain into blocks allows us to accommodate geometric flexibility with high order operators, which will be discussed in Section 4.3. Having an overlap region of grid points at the block interfaces is needed to achieve a transfer of the numerical solution from one block to another block. As discussed earlier, in our SBP operators (2.23), the standard sixth order central finite difference method is used for the interior grid nodes. In this study, the decomposition is performed on the interior grid points and sufficiently far from the boundary modification of our SBP operator. For the seven-point stencil of the standard sixth order central finite difference method (2.35), a three-point overlap at each side of

inter-block boundaries is required.

$$Q = \left(\begin{array}{cccccc|ccc|cccc} \times & \times & \times & \times & \times & \times & & & & & & & \\ \times & 0 & \times & \times & \times & \times & & & & & & & \\ \times & \times & 0 & \times & \times & \times & & & & & & & \\ \times & \times & \times & 0 & \times & \times & \times & & & & & & \\ \times & \times & \times & \times & 0 & \times & \times & \times & & & & & \\ \times & \times & \times & \times & \times & 0 & \times & \times & \times & & & & \\ & & & \times & \times & \times & 0 & \times & \times & \times & & & \\ & & & & \times & \times & \times & 0 & \times & \times & \times & & \\ \hline & & & & & \times & \times & \times & 0 & \times & \times & \times & \\ & & & & & & \ddots & \ddots & \ddots & \ddots & \ddots & \ddots & \ddots \end{array}\right). \tag{2.35}$$

The data at block interfaces are treated as block boundary conditions which are updated after each Runge–Kutta stage. As illustrated in Figure 2.1, the black points are located on the block boundary. The three red points in the interior of the left block communicate their data to the overlapping white points of the right block. Likewise, the three green points in the interior of the right block communicate their data to the overlapping white points of the left block. The inter-block communication between neighbouring blocks is accomplished by using the Message Passing Interface (MPI) such that each block is assigned to a single process. The data in the buffer arrays are updated after each stage when all blocks have been processed.

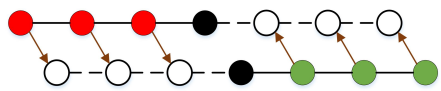

Figure 2.1: Illustration of points overlapping along a line. The black points lie on the block boundary, the red and green points are internal points in different blocks, the white points are added ghost points which overlap the internal points in the other block, and the arrows indicate the direction of data transfer between blocks.

Note that the above method provides synchronized boundary conditions at the block interfaces. Therefore, the derivative of flow variables is computed based on the values at the same time stage. This ensures that the solution of the multi-block algorithm is exactly the same as that of the single block algorithm.

The multi-block approach offers great flexibility in both implementation, memory allocation and computation time for the solver, and also provides a natural platform for parallel implementation. However, the disadvantage is

that if a grid has a lot of blocks, the computational time could suffer because of the explicit nature of the data communication between blocks.

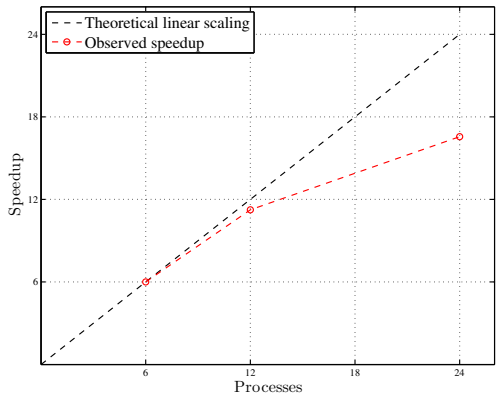

Figure 2.2: Ideal and observed speedup against the number of processes for the fluid solver with one process per block.

To investigate the effects of parallelization on our flow solver, strong scaling is chosen as a metric to show how simulating a given case will speed up when more processes are used. With strong scaling, as the number of cores increases, the problem size remains the same. A viscous channel flow is considered at Re = 378 and Ma = 0.1. A 1280×2048 grid is used with CFL = 0.1 and the case is solved for 1000 time steps. Figure 2.2 shows the resulting speedup compared to the 6 processes.

The number of blocks was doubled by halving the blocks in the $y-$direction. The test is made using one node with multiple cores. The scaling showing the performance of our solver is good. However, as seen in Figure 2.2, the theoretical behaviour would be linear. All simulations in our work are done on the Kongull and Vilje clusters at NTNU with Intel Xeon E5-2670 8-core CPUs.

CHAPTER 3

Mathematical Model of Structure Deformation

In this chapter, structural models used for fluid-structure interaction simulations are presented. The computational approaches and their procedures are stated.

3.1 The Euler-Bernoulli Beam Theory

A beam is a structural element in which one of its dimensions is much larger than the other two dimensions. The axis of the beam is considered along the longer dimension and a beam primarily resists loads applied laterally to its axis. A cross-section normal to the longer axis is assumed to vary smoothly along the span or length of the beam [7]. Several beam theories have been developed based on various assumptions, and lead to different levels of accuracy. One of the simplest and most useful of these theories was first described by Leonhard Euler and Daniel Bernoulli in the 17th century [44] and is commonly called Euler–Bernoulli beam theory.

In order to study the transverse motion of beams, the coupling between the membrane forces (axial) and the transverse motion which is known as geometric nonlinearity, can be neglected [83, 112]. Therefore, the linear Euler–Bernoulli beam theory is a simplification of the geometrically nonlinear theory. If the membrane force of the beam is constant or it can be neglected, which is valid for beams for small deformations, this theory can model the structure appropriately [7]. Nonetheless, when the membrane force becomes significant, like in the case of buckling and large deformations, the linear theories become inaccurate. The Euler–Bernoulli beam theory does not take into account the effect of the correction for transverse shear and rotatory inertia [27, 83]. Moreover, it is assumed that the mass per unit length and the stiffness of the beam remain constant along the length of the beam.

This model is a valid approximation for thin beams under small transverse deformations. Based on the Experimental measurements, these assumptions are accurate for long, slender beams made of isotropic materials with rigid cross-sections [7]. When one or more of these conditions are not met, the predictions of Euler–Bernoulli beam theory can become inaccurate and the need for a new model arises.

According to what is described above, the Euler–Bernoulli beam theory can be summarized in three major assumptions. The essential assumption is that no deformations happen in the plane of the cross-section, i.e. the cross-section of the beam is infinitely rigid in its own plane. The second and third assumptions are that the out-of-plane displacements of the cross-section remain plane after deformation and normal to the neutral axis of the beam, respectively [7].

Figure 3.1 shows a beam element with constant properties along its span (x-direction) subjected to only two bending moments M, at the ends of the element. y-direction indicates the transverse direction. The dashed rectangle depicts the reference configuration of the beam element at the initial time. Since the only applied load to beam is the bending moment, this type of problem is often referred to as *pure bending* [7]. The cross-section of the beam ($a - b$ line in 2D) is assumed to be symmetric, and bending takes place in that plane of symmetry. The line on the cross-section is called the neutral axis which is not carrying any stresses.

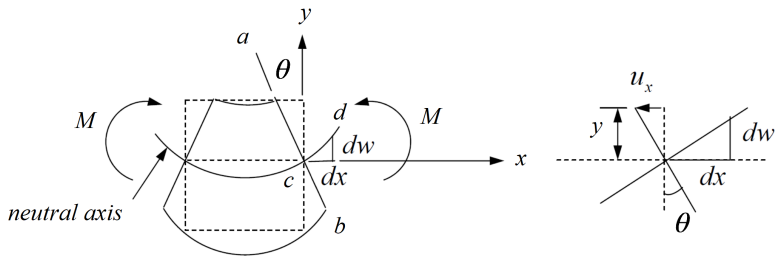

Figure 3.1: Schematic of an infinitesimal element of the beam.

Considering Green's Strain [100], u_x and u_y are displacements of the member at any point in the x and y direction, respectively. x is along the axis of the beam and y perpendicular to the axis. u and w are displacements of the point at the middle plane of the beam along $x-$ and $y-$directions, respectively, as shown in Figure 3.1. The middle plane deflections of the beam u, w, can be related to u_x, u_y, the deflections of any point on the beam from Kirchhoff's Hypothesis [83, 114].

Since the bending moment and physical properties are all constant along the beam's span, the deformation of the beam is identical at all points along its axis. This results in a constant curvature, i.e. the beam deforms into a curve of constant curvature as a circular arc, as illustrated in Figure 3.1. In the initial configuration (cf. dashed reactangle in Figure 3.1), a cross-section of the beam is a plane (line in 2D) perpendicular to the axis of the beam x-direction. For a more realistic problem, e.g. a finite length beam with specific boundary conditions and applied transverse loads, the bending moment distribution varies along the span and the symmetry arguments used for the above idealized problem no longer apply [7].

By the first Euler–Bernoulli assumption, the displacement field in the plane of the cross-section consists only of one rigid body translation $u_y = w(x)$, which is the vertical deflection of the neutral axis.

The second Euler–Bernoulli assumption implies an axial displacement field consisting of a rigid body translation u_x, and rigid body rotations $\theta(x)$ as shown in Figure 3.1

$$u_x(x) = u - y\theta(x) \tag{3.1}$$

As depicted in Figure 3.1 the plane $a - b$ remains perpendicular to the neutral axis $c - d$ by the third Euler–Bernoulli assumption . This implies the equality of the slope of the beam and of the rotation of the section $\theta = \frac{\partial w}{\partial x}$ [7].

The normal and shear strains can be evaluated from the displacement field by employing the fundamental assumption of linear elasticity as follows

$$\begin{gathered} \epsilon_{yy} = \frac{\partial u_y}{\partial y} = \frac{\partial w}{\partial y} = 0, \quad \epsilon_{xx} = \frac{\partial u_x}{\partial x} = \frac{\partial u}{\partial x} - y\frac{\partial^2 w(x)}{\partial x^2}, \\ \gamma_{xy} = \frac{\partial u_x}{\partial y} + \frac{\partial w}{\partial x} = 0 \end{gathered} \tag{3.2}$$

The following notation for the sectional deformations which depend only on the spanwise variable can be introduced

$$\bar{\epsilon} = \frac{du}{dx}, \quad \kappa = \frac{\partial \theta}{\partial x} \approx \frac{\partial^2 w}{\partial x^2}, \tag{3.3}$$

where $\bar{\epsilon}$ is is the sectional axial strain, κ the curvature along the beam and θ is the slope of the deformed beam. Using these sectional strains, the axial strain distribution ϵ_{xx} in (3.2), over the cross-section becomes

$$\epsilon_{xx} = \bar{\epsilon} - y\kappa. \tag{3.4}$$

As mentioned above, the beam is assumed to be made of a linearly elastic, isotropic material that obeys Hooke's law $\sigma = E\epsilon_{xx}$ where E is the Young modulus. Note that the normal and shear stresses in the y or z directions are considered to be zero. Therefore, the resultant normal force is zero.

$$\int_A \sigma dA = \int_A E\epsilon_{xx} dA = E\bar{\epsilon} \int_A dA - E\kappa \int_A y dA. \tag{3.5}$$

Since the $x-$axis passes through the centroid of the cross-section of the beam $\int_A y dA = 0$. The resultant bending moment is expressed as

$$M(x,t) = \int_A \sigma y dA = E\epsilon_{xx} \int_A y dA - E\kappa \int_A y^2 dA = -EI\kappa, \tag{3.6}$$

where $I = \int_A y^2 dA$ is the moment of inertia.

3.2 Plate Equation of Motion

In order to derive the equation of motion for transverse motion of a flexible structure (thin plate in this study or beam as a general example), there are various levels of complexity which can be added to the problem. The effects of shear distortion, rotatory inertia and the effect of axial forces and axial deformation can be mentioned as examples [27, 83]. Including all of these factors can lead to a complicated model which would be difficult to solve and distract us from the scope of our fluid-structure interaction investigation of the axial deformation and the transverse motion of a thin plate.

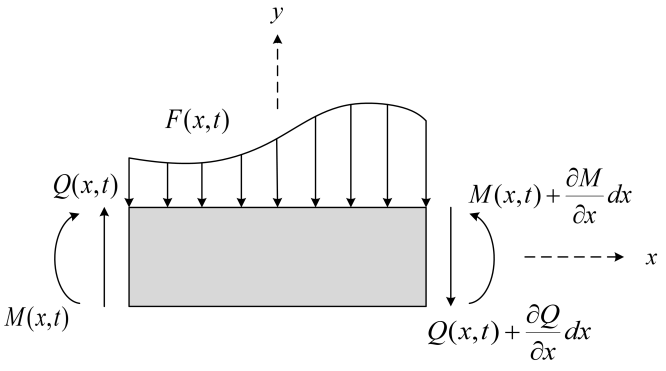

Figure 3.2: Schematic of a plate under end bending moments and applied load.

As shown in Figure 3.2, a plate (beam) element of length dx is considered. $F(x,t)$ represents the applied transverse force, $Q(x,t)$ is the internal shear

force, $M(x,t)$ denotes the internal moment, $m_s = \rho_s h$ is the mass per unit length of the structure, h is the thickness. $w(x,t)$ is the vertical deflection of the thin plate. The equilibrium of forces in the vertical direction gives

$$F(x,t)dx + \left(Q(x,t) + \frac{\partial Q}{\partial x}dx\right) - Q(x,t) = m_s dx \frac{\partial^2 w}{\partial t^2}, \tag{3.7}$$

$$F(x,t) + \frac{\partial Q}{\partial x} = m_s \frac{\partial^2 w}{\partial t^2}. \tag{3.8}$$

An equation for the shear force is required, $Q(x,t)$, which will be obtained by the sum of moments from the center of the beam element in Figure 3.2.

$$-\left(M(x,t) + \frac{\partial M}{\partial x}dx\right) + M(x,t) + \left(Q(x,t) + \frac{\partial Q}{\partial x}dx\right)\frac{dx}{2} + Q(x,t)\frac{dx}{2} = 0. \tag{3.9}$$

Which simplifies

$$Q(x,t) = \frac{\partial M}{\partial x} \tag{3.10}$$

Inserting (3.6) and (3.10) into (3.8), results in

$$m_s \frac{\partial^2 w}{\partial t^2} + \frac{\partial^2}{\partial x^2} K_B \frac{\partial^2 w}{\partial x^2} = F(x,t), \tag{3.11}$$

where K_B is the flexural rigidity or bending stiffness of the plate which is defined as $K_B(x) = EI(x)$, E is the elastic Young modulus and $I(x)$ is the moment of inertia. The flexural rigidity can be expressed as

$$K_B = \frac{Eh^3}{12(1-\nu^2)}, \tag{3.12}$$

where h is the flexible plate thickness and ν is Poisson's ratio [108].

3.3 Modal Analysis

For the eigenvalue problem of the Euler–Bernoulli beam, i.e. free oscillation case $\mathbf{F}(x,t) = 0$, the thin plate equation of motion Eq. (3.11) becomes

$$m_s \frac{\partial^2 w}{\partial t^2} + K_B \frac{\partial^4 w}{\partial x^4} = 0 \tag{3.13}$$

Transverse oscillation of the plate is an initial-boundary value problem (IBVP) and involves a second order derivative with respect to time and a fourth order derivative with respect to the space coordinates. Therefore, both initial and boundary conditions are required to obtain a unique solution

$w(x,t)$. The solution to the problem given by Eq. (3.13) can be produced by first obtaining the natural frequencies and mode shapes, and then expressing the general solution as a summation of modal responses [81]. In each mode, the system will oscillate in a fixed shape at a constant frequency, which allows to separate the displacement function into two separate time and space functions [115]. Thus, the displacement can be defined as

$$w(x,t) = A(x)B(t) \tag{3.14}$$

where $A(x)$ and $B(t)$ take into account the spatial and temporal behaviour of the plate. By inserting Eq. (3.14) into the eigenvalue problem Eq. (3.13) and rearranging it, the free oscillation solution is obtained as

$$\frac{1}{B(t)}\frac{d^2B(t)}{dt^2} = -\frac{\alpha}{A(x)}\frac{d^4A(x)}{dx^4} = -\Omega_m^2 \tag{3.15}$$

where $\alpha = \frac{K_B}{m_s}$. The constancy of the terms can be inferred by the independence of both sides to each other. Taking the constant value as the eigenfrequency Ω_m^2, i.e, the natural frequency of the beam, the two ordinary differential equations can be obtained as

$$\frac{d^4A(x)}{dx^4} - k_m^4 A(x) = 0 \tag{3.16}$$

$$\frac{d^2B(t)}{dt^2} + \Omega_m^2 B(t) = 0 \tag{3.17}$$

where $k_m^4 = \frac{\Omega_m^2}{\alpha}$. Solving these two ordinary differential equations (ODE), the general solution of the problem based on linear combination of trigonometric functions can be obtained.

The solution of Eq. (3.16) can be expressed as

$$A(x) = C_1\cos(k_m x) + C_2\sin(k_m x) + C_3\cosh(k_m x) + C_4\sinh(k_m x) \tag{3.18}$$

where the constants C_i, $i = 1, ..., 4$ can be found by the imposed boundary conditions from the specific physical problem.

The solution of Eq. (3.17) can be expressed as

$$B(t) = C_5\cos(\Omega t) + C_6\sin(\Omega t) \tag{3.19}$$

where the constants C_5 and C_6 can be found by the initial conditions.

Thus, the general solution of displacement $w(x,t) = A(x)B(t)$, yields to

$$w(x,t) = \Big(C_1\cos(k_m x) + C_2\sin(k_m x) + C_3\cosh(k_m x) + C_4\sinh(k_m x)\Big)\cdot\Big(C_5\cos(\Omega t) + C_6\sin(\Omega t)\Big) \tag{3.20}$$

Finally, the angular eigenfrequencies, i.e. natural frequencies of the beam can be calculated as

$$\Omega_m = \beta_m^2\sqrt{\frac{K_B}{m_s}} \tag{3.21}$$

The values $\beta_m = k_m L$, where L is the characteristic length of the beam, are solutions to an eigenvalue equation depending on the boundary conditions, as explained in the following sections.

3.3.1 Cantilevered Plate

The cantilevered beam is clamped at the leading edge and free at the trailing edge where no constraints are applied and it can deflect freely. In this case, the boundary conditions at the leading edge for the displacement $w(x = 0) = 0$, and the slope of the tangent of the deformed beam $\frac{\partial w}{\partial x}\Big|_{x=0} = 0$. At the trailing edge the bending moment $\frac{\partial^2 w}{\partial x^2}\Big|_{x=L} = 0$ and the shear force $\frac{\partial^3 w}{\partial x^3}\Big|_{x=L} = 0$. Solving the linear system derived for the four constants from Eq. (3.20), gives

$$\begin{aligned} C_1 &= -C_3 \\ C_2 &= -C_4 = C_3\tfrac{\cos(k_m L)+\cosh(k_m L)}{\sin(k_m L)+\sinh(k_m L)} \end{aligned} \tag{3.22}$$

Therefore, the cantilevered beam has the following natural modes

$$\begin{aligned} A_m(x) = C_3\Bigg(&\Big(\cosh(k_m x) - \cos(k_m x)\Big) \\ &-\tfrac{\cosh(k_m L)+\cos(k_m L)}{\sinh(k_m L)+\sin(k_m L)}\Big(\sinh(k_m x) - \sin(k_m x)\Big)\Bigg) \\ m = 1, 2, 3, \ldots &\infty \end{aligned} \tag{3.23}$$

where C_3 denotes the amplitude scaling constant and $k_m = \beta_m/L$ the characteristic wavenumber obtained by finding the roots of an eigenvalue equation. The coefficients β_m are obtained from

$$\cosh(\beta_m)\cos(\beta_m) + 1 = 0, \tag{3.24}$$

The five first values of β_m, $m = 1, ..., 5$, are rounded: 1.8751, 4.6941, 7.8548, 10.9955, 14.1372. The modal configurations of the cantilevered plate are shown in Figure 3.3.

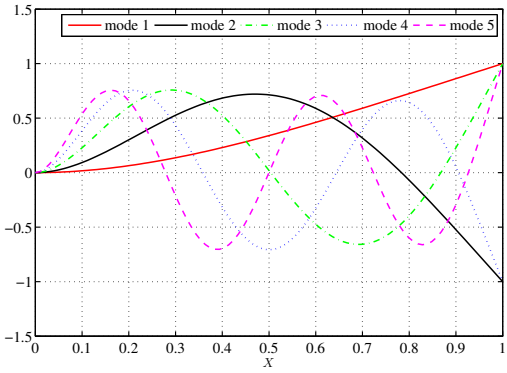

Figure 3.3: The first five eigenfunctions $A_m(x)$ for cantilevered flexible plate with $C_3 = 1$ in Eq.(3.23).

3.3.2 Hinged Free-End Plate

This model is similar to the previous one except that at the leading edge a hinge, i.e. a support mechanism, permits the beam to rotate. In this case the boundary conditions at the leading edge for the displacement $w(x = 0) = 0$ and the bending moment $\frac{\partial^2 w}{\partial x^2}\Big|_{x=0} = 0$. At the trailing edge the bending moment $\frac{\partial^2 w}{\partial x^2}\Big|_{x=L} = 0$ and the shear force $\frac{\partial^3 w}{\partial x^3}\Big|_{x=L} = 0$. The constants can be obtained as

$$\begin{aligned} C_1 &= C_3 = 0 \\ C_2 &= C_4 \frac{\sinh(k_m L)}{\sin(k_m L)} \end{aligned} \tag{3.25}$$

The eigenfunction can be expressed as

$$\begin{aligned} &A_m(x) = C_2 \left(\sin(k_m x) + \frac{\sin(k_m L)}{\sinh(k_m L)} \sinh(k_m x) \right) \\ &m = 1, 2, 3, \ldots \infty \end{aligned} \tag{3.26}$$

where C_2 denotes the amplitude. The coefficients β_m are obtained from

$$\tan(\beta_m) - \tanh(\beta_m) = 0, \tag{3.27}$$

The five first values of β_m, $m = 1, ..., 5$, are rounded: 0, 3.9266, 7.0686, 10.2102, 13.3518. Note that the first mode associated to the first solution of the singularity condition corresponding to the system has a rigid rotation at the leading edge [81]. The modal configurations of the hinged free-end plate are shown in Figure 3.4.

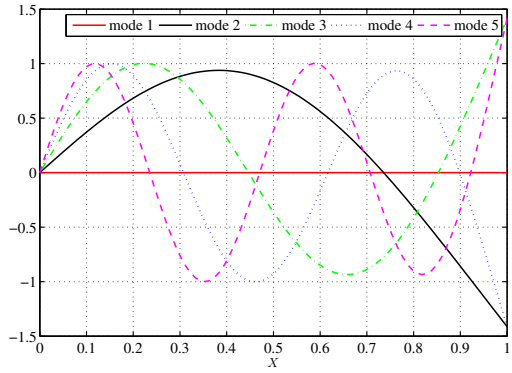

Figure 3.4: The first five eigenfunctions $A_m(x)$ for hinged free-end flexible plate with $C_2 = 1$ in Eq.(3.26).

3.4 Inextensible Plate

The various flexible structural models can be categorized based on whether the extensibility of the structure (beam) is considered in the model or not. If a model neglects this extensibility, the structure is said to be inextensible [36]. That is, the arc length of the structure always remains the same as it initially was. On the other hand, if a model can not preserve its initial arc length the structural model is said extensible. When a external force is applied to the structure in this case, the structure can be compressed or elongated [60].

In this section, a beam model that models the thin plate as an inextensible thin plate will be described. Moreover, in this model we assume that the plate deflections remain small. In this model, a two-dimensional section of the plate is represented. Described within a Lagrangian coordinate s (defined as the arc length along the plate measured from the leading edge), $\mathbf{X}(s,t)$ describes the instantaneous configuration of the plate.

To develop the governing equations, the free body diagram of a thin plate (beam) element subjected to an applied load is considered as illustrated in Figure 3.5. The geometrical configuration of the plate is $\mathbf{X} = (x(s,t), y(s,t))^T$ where s is the arc length along the Lagrangian coordinate. $M(s,t)$ is the bending moment, $Q(s,t)$ is the transverse shear force, and $\mathbf{F}(s,t)$ is the Lagrangian force exerted on the flexible plate and $T(s,t)$ is the applied axial force called tension.

The local normal $\mathbf{n}$ which points towards the local curvature center and tangent vector $\boldsymbol{\tau}$ are defined as

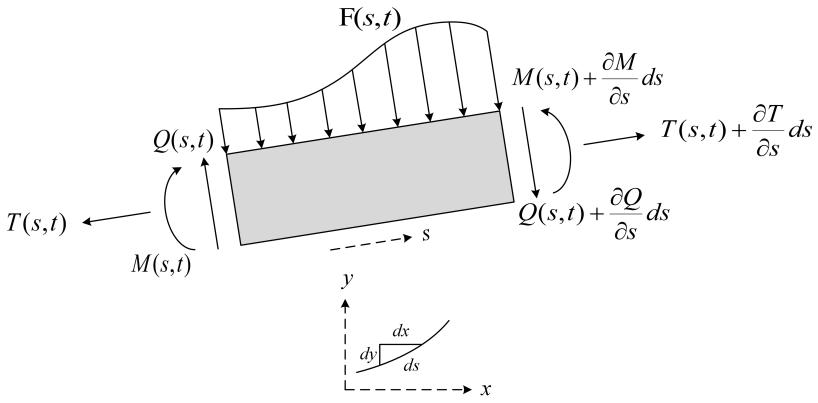

Figure 3.5: Schematic of an element under end bending moments, applied load, internal shear load and applied axial force.

$$\boldsymbol{\tau} = \frac{\partial \mathbf{X}}{\partial s}, \quad \mathbf{n} = \frac{\partial \boldsymbol{\tau}}{\partial s} = \frac{\partial^2 \mathbf{X}}{\partial s^2}. \tag{3.28}$$

Under the Euler–Bernoulli assumption (cf., Section 3.1), i.e. plane sections preserve their planarity and are normal to the deflected plate axis, the moment can be expressed as a function of curvature along the beam κ

$$M = -K_B \kappa = -K_B \frac{\partial^2 \mathbf{X}}{\partial s^2} \cdot \mathbf{n}, \tag{3.29}$$

where $K_B = EI$ is the flexural rigidity of the plate (bending stiffness) with E the Young modulus and I the moment of inertia of the cross-section of the thin plate, κ is the curvature. This curvature is defined as the rate of change of the direction of the tangent line with respect to the arc length s. Since a uniform plate is assumed in the formulation, the bending stiffness is not variable along the plate length. Therefore, the transverse shear force can be obtained by using the Euler–Bernoulli assumption as

$$Q(s,t) = \frac{\partial M}{\partial s} = -\frac{\partial}{\partial s}\Big(K_B \frac{\partial^2 \mathbf{X}}{\partial s^2}\Big) \cdot \mathbf{n}. \tag{3.30}$$

Imposing the translational equilibrium for an infinitesimal element perpendicularly loaded and neglecting higher order infinitesimal contributions, the equilibrium condition of forces leads to

$$\mathbf{F}(s,t)ds + \Big(T(s,t)\boldsymbol{\tau}(s,t) + \frac{\partial}{\partial s}\Big((T(s,t)\boldsymbol{\tau}(s,t)\Big)ds\Big) - T(s,t)\boldsymbol{\tau}(s,t) + \Big(Q(s,t) + \frac{\partial Q}{\partial s}ds\Big) - Q(s,t) = m_s ds \frac{\partial^2 \mathbf{X}(s,t)}{\partial t^2}. \tag{3.31}$$

Inserting Eq. (3.30) into Eq. (3.31) and cancelling terms result in

$$\mathbf{F}(s,t) + \frac{\partial}{\partial s}\Big(T(s,t)\boldsymbol{\tau}(s,t)\Big) - \frac{\partial^2}{\partial s^2}\Big(K_B \frac{\partial^2 \mathbf{X}}{\partial s^2}\Big) = m_s \frac{\partial^2 \mathbf{X}(s,t)}{\partial t^2}, \tag{3.32}$$

where m_s is the excessive mass per unit length of the structure, i.e. $m_s = \rho_s h$, where ρ_s is the density of the plate, and h is its thickness. $\boldsymbol{\tau}(s,t)$ is the tangent unit vector and $T(s,t)$ is the tension. The tension $T(s,t)$ functions as a Lagrangian multiplier (in the same spirit as pressure for incompressibility) to enforce the inextensibility constraint of the plate, such that the local stretching of the plate satisfies $\frac{d}{dt}|\frac{\partial \mathbf{X}}{\partial s}| = 0$. The inextensibility constraint of the plate [50, 118], can be expressed as

$$\frac{\partial \mathbf{X}}{\partial s} \cdot \frac{\partial \mathbf{X}}{\partial s} = 1. \tag{3.33}$$

Following the previous studies [50, 118], the tension T in this model is determined by a Poisson equation derived by inserting the constraint of inextensibility Eq. (3.33) into the dot product of $\frac{\partial \mathbf{X}}{\partial s}$ and the $s-$derivative of the plate dynamical equation Eq. (3.32)

$$\frac{\partial \mathbf{X}}{\partial s} \cdot \frac{\partial^2}{\partial s^2}\Big(T\frac{\partial \mathbf{X}}{\partial s}\Big) = \frac{m_s}{2}\frac{\partial^2}{\partial t^2}\Big(\frac{\partial \mathbf{X}}{\partial s} \cdot \frac{\partial \mathbf{X}}{\partial s}\Big) - m_s \frac{\partial^2 \mathbf{X}}{\partial t \partial s} \cdot \frac{\partial^2 \mathbf{X}}{\partial t \partial s} - \frac{\partial \mathbf{X}}{\partial s} \cdot \frac{\partial}{\partial s}\Big(\mathbf{F}_B + \mathbf{F}\Big), \tag{3.34}$$

where $\mathbf{F}_B = \frac{\partial Q}{\partial s}$ is the bending force which is obtained by Eq. (3.30).

The boundary conditions are specified at the leading edge ($s = 0$) and at the trailing edge ($s = L$) of the plate. The free-end boundary condition at the trailing edge is imposed by assuming that the tension, bending moment and shear force are zero

$$T(L,t) = 0, \quad \frac{\partial^2 \mathbf{X}}{\partial s^2}\Big|_{s=L} = 0, \quad \frac{\partial^3 \mathbf{X}}{\partial s^3}\Big|_{s=L} = 0. \tag{3.35}$$

At the leading edge two types of boundary conditions can be considered as mentioned in Section 3.3. One is the hinged boundary condition (support mechanism),

$$\mathbf{X}|_{s=0} = \mathbf{X}_0, \quad \frac{\partial^2 \mathbf{X}}{\partial s^2}\Big|_{s=0} = 0. \tag{3.36}$$

The other one is the clamped boundary condition which is expressed as

$$\mathbf{X}|_{s=0} = \mathbf{X}_0, \quad \frac{\partial \mathbf{X}}{\partial s}\Big|_{s=0} = (\cos\theta, \sin\theta). \tag{3.37}$$

3.5 Numerical Methods for Euler–Bernoulli Beam Model

3.5.1 Newmark Time Integration Method

The Newmark method also known as the Newmark-beta method has been one of the most commonly used integration scheme for problems in structural dynamics since Nathan M. Newmark introduced it in 1959 [82], mainly because of its improved stability characteristics [18]. This method approximates the displacement and the velocity at time $t + \Delta t$ by employing truncated Taylor expansions and assuming that the displacement, velocity and acceleration are known at the time instant t. The Taylor series employed to express the derivation are as follows

$$w_{t+\Delta t} = w_t + \Delta t \dot{w}_t + \frac{\Delta t^2}{2}\ddot{w}_t + \frac{\Delta t^3}{6}\dddot{w}_t + \dots \tag{3.38}$$

$$\dot{w}_{t+\Delta t} = \dot{w}_t + \Delta t \ddot{w}_t + \frac{\Delta t^2}{2}\dddot{w}_t + \dots \tag{3.39}$$

where $\dot{w}, \ddot{w}$ and $\dddot{w}$ denote $\frac{\partial w}{\partial t}$, $\frac{\partial^2 w}{\partial t^2}$ and $\frac{\partial^3 w}{\partial t^3}$, respectively. Neglecting the high order terms and modifying the highest order terms in (3.38) and (3.39) yields

$$w_{t+\Delta t} = w_t + \Delta t \dot{w}_t + \frac{\Delta t^2}{2}\ddot{w}_t + \beta \dddot{w}_t, \tag{3.40}$$

$$\dot{w}_{t+\Delta t} = \dot{w}_t + \Delta t \ddot{w}_t + \gamma \dddot{w}_t, \tag{3.41}$$

where β and γ are parameters that define the method. By assuming linear acceleration in each time step

$$\dddot{w} = \frac{\ddot{w}_{t+\Delta t} - \ddot{w}_t}{\Delta t}, \tag{3.42}$$

The equations are truncated and expressed as the standard form of the Newmark's equations

$$w_{t+\Delta t} = w_t + \Delta t \dot{w}_t + \Big((\frac{1}{2} - \beta)\ddot{w}_t + \beta \ddot{w}_{t+\Delta t}\Big)\Delta t^2, \tag{3.43}$$

$$\dot{w}_{t+\Delta t} = \dot{w}_t + \Big((1-\gamma)\ddot{w}_t + \gamma \ddot{w}_{t+\Delta t}\Big)\Delta t. \tag{3.44}$$

Unconditional stability is guaranteed for $2\beta \geqslant \gamma \geqslant \frac{1}{2}$. The most accurate scheme of the Newmark family which preserves energy for linear systems is the trapezoidal rule, for which the parameters are $\beta = \frac{1}{4}$ and $\gamma = \frac{1}{2}$ [6, 52].

3.5.2 Finite Difference Method

The partial differential equations for a small deflection of a thin plate are converted to a system of simultaneous algebraic equations employing finite difference operators. The standard second order central difference approximation at grid point x_i, is written as follows

$$\frac{\partial^2 w(x_i)}{\partial x^2} \approx \frac{w_{i+1} - 2w_i + w_{i-1}}{\Delta x^2}. \tag{3.45}$$

Furthermore, the standard second order difference operator for the fourth derivative is obtained by applying twice the difference operator $D_{xx} = \frac{\delta_x^2}{\Delta x^2}$ defined by the right hand side of (3.45). Therefore, using a similar approximation twice, the fourth order spatial derivatives can be approximated as

$$\frac{\partial^4 w(x_i)}{\partial x^4} \approx \frac{w_{i+2} - 4w_{i+1} + 6w_i - 4w_{i-1} + w_{i-2}}{\Delta x^4}. \tag{3.46}$$

3.6 Numerical Methods for Inextensible Plate

The discretisation of the governing equation of the plate motion (3.32) along s is performed on a staggered grid following [50]. The plate is discretized with a finite number of Lagrangian points $\mathbf{X}_i$. The plate tension is defined at the interfaces of the grid cells, and other variables are defined at the primary grid points in the centers of the grid cells, as shown in Figure 3.6.

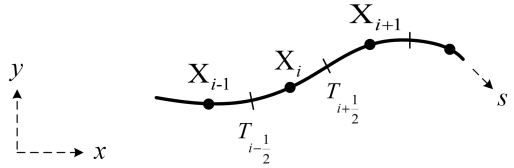

Figure 3.6: Schematic diagram of staggered grid discretization on the plate along its Lagrangian coordinate s.

Then, the numerical procedure for the non-dimensionalised form of Eqs. (3.32) and (3.34) is as follows

$$\mathbf{X}^* = 2\mathbf{X}_i^n - \mathbf{X}_i^{n-1}, \tag{3.47}$$

$$\mathbf{F}_B^* = -D_{ss}(K_B\ D_{ss}\mathbf{X}^*)_i^n, \tag{3.48}$$

$$\begin{aligned}(D_s\mathbf{X}^*)_{i+\frac{1}{2}} \cdot \Big(D_s(D_s(T_{i+\frac{1}{2}}^{n+\frac{1}{2}} D_s\mathbf{X}^*))\Big) = \\ m_s\frac{1 - 2(D_s\mathbf{X}\cdot D_s\mathbf{X})_{i+\frac{1}{2}}^n + (D_s\mathbf{X}\cdot D_s\mathbf{X})_{i+\frac{1}{2}}^{n-1}}{2\Delta t^2} - \\ m_s(D_s\mathbf{V}\cdot D_s\mathbf{V})_{i+\frac{1}{2}}^n - (D_s\mathbf{X}^*)_{i+\frac{1}{2}}^n \cdot \Big(D_s(\mathbf{F}_B^* + \mathbf{F}^n)\Big)_{i+\frac{1}{2}},\end{aligned} \tag{3.49}$$

$$m_s\frac{\mathbf{X}_i^{n+1} - \mathbf{X}_i^*}{\Delta t^2} = \Big(D_s(T^{n+\frac{1}{2}} D_s\mathbf{X}^{n+1})\Big)_i + (\mathbf{F}_B)^{n+1} + \mathbf{F}_i^n, \tag{3.50}$$

where D_s and D_{ss} are the second order accurate difference operators for the first and second derivatives along s, respectively, and $\mathbf{X}^*$ is the predicted position of the plate. Employing $\mathbf{X}^*$ to calculate the tension helps to reduce the error. The tension is computed at the intermediate time step, i.e. $t^{n+\frac{1}{2}}$ and is employed to update the position of the plate, i.e. $\mathbf{X}^{n+1}$. The velocity of the plate is defined as $\mathbf{V}_i^n = (\mathbf{X}_i^n - \mathbf{X}_i^{n-1})/\Delta t$. $\mathbf{F}^n$ denotes the force exerted externally on the structure and is obtained explicitly at time level n. Equations (3.49) and (3.50) constitute diagonally dominant tri- and pentadiagonal linear systems, which are solved by LU decomposition without pivoting, i.e. by the Thomas algorithm and a similar algorithm for the pentadiagonal linear system. The condition for diagonal dominance of the matrix in Eq. (3.50) is $K_B\frac{\Delta t^2}{\Delta s^4} \leqslant \frac{1}{4}$.

CHAPTER 4

Arbitrary Lagrangian–Eulerian Method

This chapter provides a brief overview on the arbitrary Lagrangian–Eulerian (ALE) method for fluid-structure interaction (FSI). The formulation of the ALE approach for our FSI solver is presented. The technique of re-meshing is discussed.

4.1 Introduction

There are two different mathematical representations of continuum materials: the Lagrangian formulation and the Eulerian formulation. In the Lagrangian approach, the individual material particles can easily be tracked because the coordinate system moves with material. However, the coordinate system is fixed in the Eulerian approach and the material particles pass through a stationary closed domain. Since the main weakness of the Lagrangian description is that it suffers to follow large distortions in the computational domain, a purely Lagrangian method for the kinematical description of the fluid domain is not able to conveniently track strong distortions happening often in the fluid domain [21]. However, if fluid motions are described in Eulerian coordinates, strong distortions can easily be handled because the coordinate system is fixed in space and convection terms are used to describe the fluid transport [21]. Applying an ALE formulation to FSI, the governing equations for the fluid flow can be modeled in a purely Eulerian formulation, while the purely Lagrangian formulation is employed to model the structure domain. The arbitrary Lagrangian–Eulerian (ALE) method provides a hybrid description of the Lagrangian method and the Eulerian method [48]. The coordinate system in the ALE method is associated with a moving mesh, allowing a smooth transition between the Lagrangian method and the Eulerian method.

Using the ALE method, the fluid grid is permitted to deform at an arbitrary velocity to guarantee a body-conforming fluid grid. The significant

advantage of a body-conforming grid is the correspondence of the moving boundary with the grid lines such that the geometrical discontinuities can be accurately incorporated in the computation. Furthermore, no approximation is required for the analysis of quantities at the moving boundary, i.e., wall shear stress and pressure.

In the ALE formulation of a deforming fluid grid, the velocity of the moving walls is imposed. In the FSI case the velocity at the interface is equal to the velocity of the solid material at the interface (no-slip condition). The grid velocity $\hat{\mathbf{u}}$ has to be included in the Navier–Stokes equations as follows

$$\frac{D}{Dt} = \frac{\partial}{\partial t} + (\mathbf{u} - \hat{\mathbf{u}}) \cdot \nabla \tag{4.1}$$

Note that the time derivative of material changes $\frac{D}{Dt}$ observed at a given point in the Lagrangian formulation, is transformed into the Eulerian formulation by $\frac{D}{Dt} = \frac{\partial}{\partial t} + \mathbf{u} \cdot \nabla$. When the ALE formulation (4.1) is applied to a computational mesh, the case $\hat{\mathbf{u}} = 0$ yields the Eulerian formulation for a stationary domain, while $\hat{\mathbf{u}} = \mathbf{u}$ yields the Lagrangian formulation. Grid point positions and velocities in the fluid domain are determined by the motion of the structure at the boundary.

This body-conforming mesh method causes some difficulties when applied to FSI problems. The process of mesh generation is still manual in most of the cases. Generation of a body-conforming grid automatically is not always possible. Therefore, it is preferable to eliminate the user intervention and to seek an automatic meshing procedure. Furthermore, in many cases, the quality of the generated mesh is not satisfactory. If the boundaries move too much, the quality of the fluid grid definitely degenerates and the large displacement of a point may cause the volume of the element or cell to become negative, giving rise to the failure of the simulation [13, 109]. For small deformations of the structure, the moving mesh method is often employed to deform the grid points and to provide the motion of the boundary. On the contrary, for large geometrical deformation of the structure, using moving mesh may lead to highly distorted meshes and eventually cause a breakdown of the calculation as mentioned above. In the case of moving mesh, the topology of the mesh and the resolution of the computational domain should be adjusted. This can be performed by re-meshing along with information mapping. Information mapping is employed for transferring the flow field data from the old grid to the new one. This may, however, cause numerical errors. Since frequent re-meshing slows down the computation, it is in most cases undesirable [13, 109].

4.2 Arbitrary Lagrangian–Eulerian Formulation for the Compressible Navier–Stokes Equations

In this section, the ALE approach is formulated to handle the fluid flow in Eulerian description using moving fluid grids and the flexible structure in a Lagrangian formulation using stationary structure grids. For moving meshes, i.e., time-dependent geometries, the coordinate transformation will also depend on time. Thus, for each time instant the mapping (Eq. (2.8)) will change. The time-dependent coordinate transformation can be expressed as

$$\begin{aligned} t &= \tau, \\ x &= x(\xi, \eta, \tau), \\ y &= y(\xi, \eta, \tau), \end{aligned} \tag{4.2}$$

where τ is the time in transformed coordinates. The transformed 2D compressible Navier–Stokes equations in perturbation form [91] can be expressed as

$$\hat{\mathbf{U}}'_\tau + \hat{\mathbf{F}}'_\xi + \hat{\mathbf{G}}'_\eta = 0, \tag{4.3}$$

where $\hat{\mathbf{U}}' = J^{-1}\mathbf{U}'$, and the transformed flux vectors are

$$\begin{aligned} \hat{\mathbf{F}}' &= J^{-1}\Big(\xi_t \mathbf{U}' + \xi_x(\mathbf{F}^{c\prime} - \mathbf{F}^{v\prime}) + \xi_y(\mathbf{G}^{c\prime} - \mathbf{G}^{v\prime})\Big), \\ \hat{\mathbf{G}}' &= J^{-1}\Big(\eta_t \mathbf{U}' + \eta_x(\mathbf{F}^{c\prime} - \mathbf{F}^{v\prime}) + \eta_y(\mathbf{G}^{c\prime} - \mathbf{G}^{v\prime})\Big). \end{aligned} \tag{4.4}$$

The chain rule for partial differentiation provides the expressions for Cartesian derivatives in the viscous flux vectors $\mathbf{F}^{v\prime}$ and $\mathbf{G}^{v\prime}$, e.g.

$$\begin{aligned} u'_x &= u'_\xi \xi_x + u'_\eta \eta_x, \\ u'_y &= u'_\xi \xi_y + u'_\eta \eta_y. \end{aligned} \tag{4.5}$$

The Jacobian determinant of the transformation is $J^{-1} = x_\xi y_\eta - x_\eta y_\xi$ and time-dependent metric terms are

$$\begin{aligned} J^{-1}\xi_x = y_\eta, \quad J^{-1}\xi_y = -x_\eta, \quad \xi_t = -x_\tau \xi_x - y_\tau \xi_y, \\ J^{-1}\eta_x = -y_\xi, \quad J^{-1}\eta_y = x_\xi, \quad \eta_t = -x_\tau \eta_x - y_\tau \eta_y. \end{aligned} \tag{4.6}$$

In the time-dependent coordinate transformation of the fluid flow domain, the local velocities of the fluid domain $\dot{x} = x_\tau$ and $\dot{y} = y_\tau$ are subtracted from the fluid velocity to define the contravariant velocity components $U = \xi_x(u - \dot{x}) + \xi_y(v - \dot{y})$ and $V = \eta_x(u - \dot{x}) + \eta_y(v - \dot{y})$ which yield simple expressions for the transformed inviscid flux vectors $\hat{\mathbf{F}}^c$ and $\hat{\mathbf{G}}^c$ [94]. The $\xi-$ and $\eta-$ directions in (4.6) are discretized by the globally fourth order accurate SBP operator (2.23). Moving mesh is implemented to update the whole fluid domain in each time step.

Solving fluid flow on a moving mesh, the numerical scheme should satisfy the Geometric Conservation Law (GCL) for mathematical consistency [128]. This law states that

$$(J^{-1})_\tau + (J^{-1}\xi_t)_\xi + (J^{-1}\eta_t)_\eta = 0, \tag{4.7}$$

where the time derivatives of the computational coordinates ξ and η are calculated from the grid point velocities $\dot{x} = x_\tau,\ \dot{y} = y_\tau$ as follows, cf. (4.6)

$$\xi_t = -\xi_x\dot{x} - \xi_y\dot{y}, \quad \eta_t = -\eta_x\dot{x} - \eta_y\dot{y}. \tag{4.8}$$

Then, the 2D Navier–Stokes equations in ALE formulation [91] are given by

$$\mathbf{U}'_\tau = \tfrac{1}{J^{-1}}(-\hat{\mathbf{F}}'_\xi - \hat{\mathbf{G}}'_\eta - (J^{-1})_\tau\mathbf{U}'), \tag{4.9}$$

where the transformed flux vectors $\hat{\mathbf{F}}'$ and $\hat{\mathbf{G}}'$ are defined in (4.4).

4.3 Moving Mesh

The multi-block structured grid approach discussed in Section 2.3 is employed to accommodate geometric flexibility with high order operators in order to represent the simplified geometry in the upper airways.

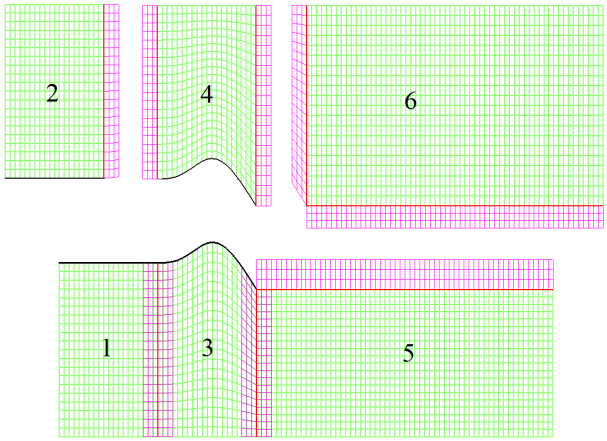

Figure 4.1: Multi-block topology of the computational domain for the simplified geometry of the upper airways. The three upper blocks are detached in the figure for illustration of the three-point overlap, shown with magenta lines.

Figure 4.1 shows 6 blocks to decompose the computational domain as an example. Blocks 1, 3 and 5 have the lower channel wall as their southern

boundaries and the rigid plate, flexible plate and the line between the trailing edge of the flexible plate and the outlet, respectively, as their northern boundaries, cf. lower plot in Figure 4.1. The upper neighbouring blocks 2, 4 and 6 with the upper channel wall as their northern boundaries are set apart in the upper plot of Figure 4.1 to show the overlapping regions.

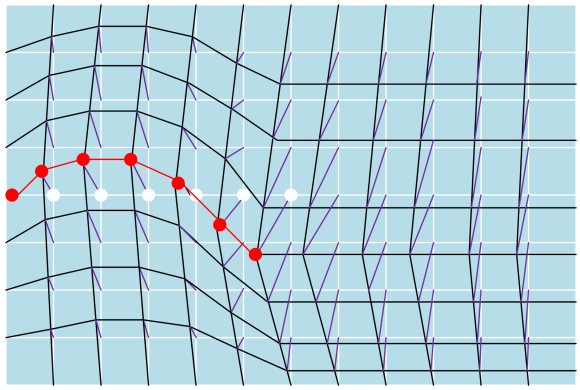

Figure 4.2: Schematic of how the deformed mesh is generated, given the displacement of the structure (red dots) and initial configuration (white dots).

The computation using mesh update is parallelized by dividing the blocks into smaller blocks with overlaps. However, the mesh structure and resolution in a sub-domain are often strongly affected by the other sub-domain. The mesh is updated by an automatic remesh in each time step using the positions and velocities of the flexible structure at the boundary and a linear interpolation for interior points in the fluid domain as shown in Figure 4.2. The white lines represent the initial configuration of the structure and computational domain. Black lines are the new mesh of the domain, the red lines and circles illustrate the structure deformation and the purple lines show the displacement of the grid nodes at the new time level compared to the initial ones.

CHAPTER 5

Immersed Boundary Method

This chapter provides a general overview on the state-of-the-art immersed boundary methods. The developed model is defined and the procedures for applying it to complex geometries and moving boundaries are presented.

5.1 Introduction

The term *immersed boundary method* was initially introduced by Peskin in 1972 [87] and particularly designed to deal with elastic (deforming) boundaries to simulate blood flow in a cardiovascular system. Since then, the immersed boundary method (IBM) which is a Cartesian grid-based method has gained a growing interest in computational fluid dynamics for solving complex and moving boundary problems. Nowadays, the immersed boundary methods can broadly be classified into two major categories, namely a continuous forcing approach and a discrete (or direct) forcing [75]. These approaches are also called diffuse and sharp interface methods, respectively.

In the first category which was originated by Peskin [87, 88], a continuous forcing function is included in the momentum equation in the entire domain. Thus, a diffused boundary representing the effect of a solid body on the flow field is associated with the force distribution on the fluid. Many methods have been developed to determine the body force on the fluid. In the case of elastic boundaries, the IB is represented by a set of massless elastic fibres and the location of these fibres is tracked using Lagrangian method by allowing a few massless points to move with the local fluid flow velocity. The forcing function can be defined by a sharp delta function with a smooth distribution to represent the applied force by the IB on the fluid flow. The boundary force can be determined by a distribution function on a particular segment at a time instant obtained by the boundary configuration at that time [87, 89]. If a rigid boundary is considered, a feedback forcing can be

used [34, 61, 99]. The main idea is to make the fluid at rest on the immersed surface (no-slip boundary condition) by applying a body force. Since the applied body force is unknown, it must be calculated in some feedback way to employ the velocity on the boundary. Therefore, the force is dependent on the difference between the interpolated velocity at the boundary and the desired boundary condition. This approach and its subsequent developments have been successfully used for a multitude of applications in incompressible fluid flow [131]. The significant advantage of continuous forcing approaches is that they are independent of the underlying spatial discretization. However, the major drawbacks of these types of IBM are that they may not only induce spurious oscillations, but also numerical instability issues particularly for unsteady flows at high Reynolds numbers due to the inherent stiffness of the source terms [34, 35].

Conversely, in the discrete forcing approach (sharp interface method), the governing equations are discretized on a Cartesian grid without computing any forcing term directly. In this approach, the presence of the solid surface imposed on the fluid is considered by adjusting the discretization in the vicinity of the immersed boundary in order to take the boundary conditions at the IB into account directly. Therefore, these sharp-interface approaches are better suited for higher accuracy than the diffuse-interface approaches. The sharp-interface methods have also been developed in different distinct formulations to deal with the fluid-solid interface.

For instance, Ye et al. [132] proposed an approach for simulating convection dominated flows on a collocated (non-staggered) grid called a cut-cell method (also named Cartesian grid method). This method was firstly introduced by Clarke et al. [17] for inviscid flows and has then been applied to viscous flows [122, 124, 132]. In the cut-cell method, a finite volume scheme is designed to represent the conservation laws for cells cut by the immersed boundary, while the flow away from the IB can be discretized by using standard methods. Since the cut-cell method is based on the finite volume method, it strictly preserves the conservation of mass, momentum and energy particularly in the vicinity of the immersed boundary. Therefore, the significant advantage of this method is to precisely impose the boundary conditions at the body and to be conservative. However, the wide range of possibilities of geometrical shapes for cut-cells (complex polyhedral cells) causes to difficulties in extending the method to 3D and implementing it for arbitrarily complex geometries. Furthermore, a large number of special treatments is needed to implement and formulate the boundary conditions in cells cut by the immersed boundary. Nevertheless, there have been some improvements in its implementation in recent years [39, 45, 59, 101, 102].

In another group of sharp-interface methods, the presence of forcing term

is taken into account at the fluid nodal points in the vicinity of the fluid-solid interface as a velocity corrector such that the boundary conditions at the immersed body are satisfied. In this way, a forcing term does not need to be calculated, but the boundary conditions are incorporated through the reconstruction of the local flow field around the immersed interface. Thus, the flow field is locally reconstructed by satisfying the actual values of the boundary conditions through appropriate interpolation. The main advantage of this method is that a forcing term never needs to be evaluated, because the forcing is directly realized by the boundary conditions. Therefore, the method is termed as the direct forcing approach. The approach was first proposed by Mohd–Yusof [76] for spectral methods. In this work, the effect of the body force is calculated by determining the difference between the mirrored velocity at the internal points inside the body with the velocity at the external points outside the body to enforce the tangential velocity at the immersed boundary. In this procedure, the presence of force counteracts the errors between the calculated velocities and the physical velocity profile at the immersed body.

Fadlun et al. [26] further implemented the discrete-time forcing approach to a three-dimensional finite difference method on a standard marker-and-cell (MAC) staggered grid, as suggested by [76] and showed that this approach is more efficient. In contrast to the work by Mohd–Yusof [76], their interpolation scheme does not depend on the mirrored velocity points inside the solid body. Linear interpolations for reconstruction of velocity at the grid point nearby the solid body boundary is used. The interpolation directions in the method proposed by Fadlun et al. [120] was either the streamwise direction or the transverse one (as illustrated in Figure 5.1(a)). The choice of direction which is arbitrary, makes it problematic for complex configuration.

A better reconstruction scheme of the fluid points near the immersed boundary was proposed by Balaras [4], who performs the reconstruction along the normal line to the body surface (as illustrated in Figure 5.1(b)). This approach eliminates the ambiguities associated with interpolation along grid lines used by Fadlun et al. [26]. However, this method was applicable to flows with immersed boundaries that are aligned with one coordinate direction, e.g, two-dimensional or axisymmetric shapes [33]. This restriction is alleviated by Gilmanov et al. [32, 33] who extends the method to arbitrarily complex, three-dimensional immersed boundaries by employing an unstructured, triangular grid for discretizing the body surface. They also extended their immersed boundary methods to moving-body simulations at different Reynolds numbers [32, 130]. Gilmanov et al. [32] extended the method to arbitrarily complex moving bodies by employing a second order hybrid staggered/non-staggered grid approach. The reconstruction is

carried out along the normal line to the body surface based on [33] by employing a quadratic interpolation scheme. Yang and Balaras [130] developed embedded-boundary formulations for laminar and turbulent flows interacting with moving boundaries. They introduced the concept of *field-extension* to treat the points emerging from a moving solid body to the fluid [130].

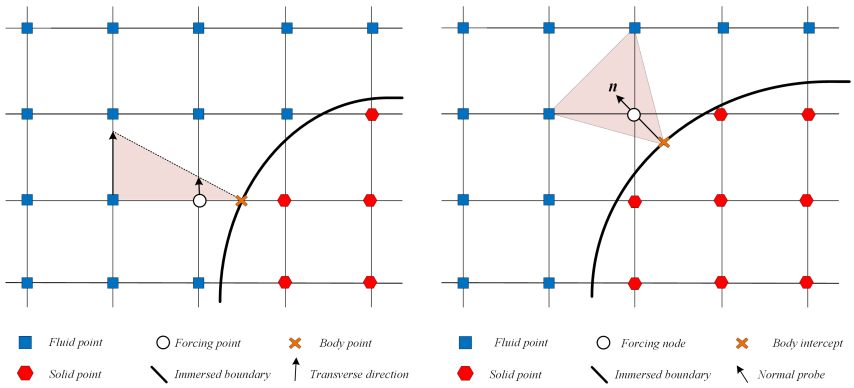

(a) Unidirectional interpolations. (b) Interpolation along normal line.

Figure 5.1: Illustration of the flow field reconstruction near the immersed boundary employing different interpolation stencils to obtain the values at the forcing points.

Tseng and Ferziger [120] developed the concept of immersed boundary approaches proposed by Fadlun et al. [26] and Verzicco et al. [126] by means of a ghost cell approach originated in [71]. In their approach, a higher order representation of the IB is accomplished by employing ghost cells inside the solid body (as shown in Figure 5.2(a)) rather than fluid points in the vicinity of the IB. Ghost cells are defined as cells within the solid body having at least one neighbouring cell inside the fluid domain. The significant concept behind this approach was to compute the flow variables at these ghost cells such that the boundary condition at the IB are satisfied. This approach is commonly referred to the ghost cell immersed boundary method (GCIBM). In this approach, an interpolation scheme needs to be devised for each ghost cell to directly incorporate the boundary conditions at the immersed body surface. To overcome the issues of reconstruction schemes, Majumdar et al. [71] and Kim et al. [58] investigated linear and quadratic stencils for a variety of two-dimensional laminar flows with finite difference and finite volume solvers. Ghias et al. [29] developed a finite difference-based ghost cell method for compressible viscous flows. Mittal et al. [74] showed the large potential of the ghost cell approach to deal with different problems, including highly complex geometries, moving and deforming bodies. They

[29, 74] constructed interpolation operators in the normal direction to the IB in order to simplify the implementation of Neumann boundary conditions at the IB. Furthermore, the concept of the image point is introduced, which is the mirror of the *ghost-cell* point along the normal direction of the body surface (as shown in Figure 5.2(b)).

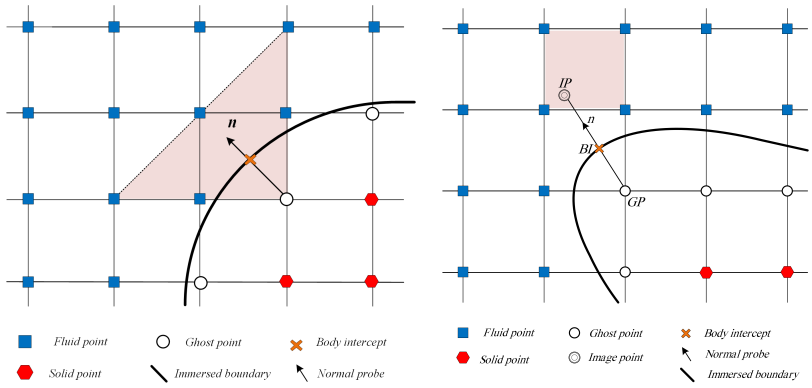

(a) Schematic of interpolation stencil with ghost point.

(b) Schematic of interpolation stencil using image point.

Figure 5.2: Illustration of the flow field reconstruction near the immersed boundary using different interpolation stencils to find the values at the ghost points.

The main difference between the works by Fadlun et al. [26], Balaras [4] and Gilmanov et al. [33] and the ghost cell immersed boundary method is that, in [29, 74, 120], the velocity field at the so-called forcing nodes (fluid points with at least one neighbouring point inside the solid body) is reconstructed by employing a linear interpolation scheme along either an arbitrary grid line or a well-defined normal line (cf. Figure 5.1). On the other hand, in the ghost cell IB by Mittal et al. [74] and Tseng and Ferziger [120], the solution is reconstructed at the ghost cells to impose the geometric existence of the immersed boundary and to satisfy the discretization stencil at the closest fluid point to the immersed boundary (cf. Figure 5.2). Both aforementioned strategies adopt the solid wall boundary conditions directly in their formulations. Therefore, they can represent the immersed boundary sharply.

The major advantage of this group of sharp interface methods (direct forcing) is that they will potentially result in a direct control over the overall numerical accuracy and stability, even though they are highly dependent on the discretization stencil. In comparison to the other sharp interface methods such as the cut-cell method, the direct forcing or flow-reconstruction approach is simpler in implementation and formulation. In contrast to other

methods, the implementation does not increase the computational cost significantly. The interpolation is the key principle for the reconstruction in this IB method. There are a number of options available for constructing the interpolation schemes in [71]. Higher order interpolation methods can be used as better options for problems in which the higher accuracy at the near-wall region with sufficient local resolution is required.

However, most attention on immersed boundary methods has been devoted to incompressible flow [75]. Although a few IB methods for viscous compressible flows and acoustic wave propagation problems have been developed [104], works on viscous compressible flows are still scarce. De Palma et al. [19] and de Tullio et al. [20] developed an IB methods to deal with compressible turbulent flows over a circular cylinder and an airfoil using a direct forcing approach with a linear interpolation and inverse-distance weighted interpolation, respectively. Even though in the study by [20] local grid refinement is used, both of these methods lead to locally first order accurate approaches. In the compressible IB method of Ghias et al. [29], a finite difference based ghost cell method is developed using a bilinear interpolation to determine the ghost cell values. Their method was successfully tested for flows over a circular cylinder and an airfoil at low Mach numbers showing second order accuracy locally and globally.

Furthermore, the vast majority of existing immersed boundary formulations particularly for viscous compressible flows are up to second order accurate except for the studies by [12, 104]. Since Reynolds numbers are the reason to increase the resolution in the simulation, employing a high order approach could immensely boost the capability of the immersed boundary method. It is of interest to develop a high order approach to expand the applications of the immersed boundary method [136], especially for compressible flows where acoustics is of great importance. Acoustic field computations need high order formulations in order to minimize the dispersion and dissipation errors. In addition, not only the order of accuracy of the approximation in the interior and at the boundary of the fluid domain, but also the sharpness of the interface is important in order to restrict the amplitude and phase errors produced by waves interacting with the boundary [104].

In recent years, several efforts have been made to develop high order immersed boundary methods [12, 30, 62, 67, 104, 135]. The higher order ghost cell IBM for solving the linearized perturbed compressible equations for acoustic problems using a compact finite difference scheme was developed by Seo and Mittal [104]. Zhou et al. [135] developed a high order matched interface for elliptic equations with discontinuous coefficients and singular sources, and showed that it can be combined with an explicit high order finite

difference method to discretize the whole computational domain. Multiple ghost nodes along each spatial direction are used to treat the jump conditions across the immersed boundary. A fourth order IBM for the Laplace and heat equations was developed by Gibou and Fedkiw [30], where the Laplacian is discretized employing a five-point finite difference stencil. The values of the variables at the two layers of ghost nodes are determined by one-dimensional polynomial extrapolations. Linnick and Fasel [67] presented a fourth order immersed boundary method based on a compact scheme for solving the incompressible Navier–Stokes equations in a stream-function-vorticity formulation. High order correction terms for the jump conditions across the interface are introduced in their boundary treatment. The Poisson equation is not solved by a high order approach. Their method has the advantage of keeping the order of accuracy at the interface through the use of a jump function by modifying the differentiation scheme at the interface. That IBM was successfully applied to compressible flow by Brehm et al. [12]. The main feature of their new immersed boundary method [12] is that the coefficients of the irregular finite difference stencils in the vicinity of the immersed boundary are optimized to promote numerical stability.

5.2 Immersed Boundary Treatment

In this study, a multi-dimensional ghost point methodology is employed to impose the boundary conditions at the immersed boundary. The method is devised from the beginning for efficient and accurate solution of flows with complex and moving boundaries [55–57].

The basic idea in this method is to compute the value of the flow variables at each of the ghost points (referring to three layers of points inside the solid body adjoining the immersed boundary) such that the boundary conditions at the immersed boundary are satisfied. As illustrated in Figure 5.3, the procedure begins by determining the immersed boundary and then identifying the solid points, i.e. the nodes lying inside the solid body, and the fluid points, i.e. the nodes lying outside the body in the fluid domain. The ghost points (denoted by GP) are identified as the solid nodes that lie adjacent to the immersed boundary and have at least one neighbour node in the fluid domain with the standard sixth order central difference stencil at the ghost point. The image point (denoted by IP) can be found by extending a normal probe, i.e. a line normal to the immersed boundary, from the ghost point to intersect with the immersed boundary at the body intercept point (denoted by BI) such that the body intercept point lies at the midpoint of the line connecting the ghost point and the image point. Once the flow variables at the image point are computed, the ghost point variables can be determined

by imposing the boundary conditions.

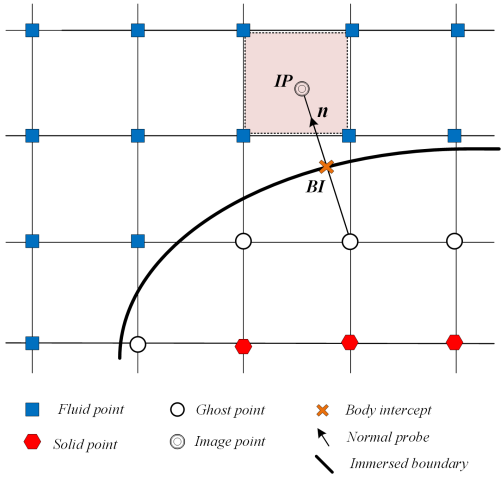

Figure 5.3: Schematic of points used to determine the flow variables at a ghost point adjacent to an immersed boundary.

The first step is to identify the ghost points. Therefore, it needs to specify whether a grid node is a fluid point or a solid point. This task is the classical problem of point-in-polygon for a 2D problem in computational geometry, i.e. given a point in space and a polygon whose geometry is defined by its boundaries (edges), determining whether the point is located inside or outside the polygon. The ray-casting algorithm is used in this study [43]. The ray-casting method works by casting a random half-infinite $x-$ray from a given point and counting the number of intersections between the ray and polygon edges. Once the intersections are identified it is straightforward to determine the grid point status. If the number of intersections is odd then the point is located inside the polygon (point B in Figure 5.4(a)), otherwise it is located outside (point A in Figure 5.4(a)).

Once the task of identifying of ghost points is accomplished, the normal distance is calculated to find the body intercept point and then the image point is determined by extending the normal line an equal distance across the boundary. The normal distance d from the ghost grid point to the surface of the geometry is obtained by a point-line distance algorithm. The surface of the geometry is discretized by body marker points making up the surface segment. The normal vector $\mathbf{n}$ at the surface segment is calculated from the geometric coordinates of the points involved in the surface segment. Once the vector $\mathbf{r}$ between the ghost point and the closest body marker point is identified, the normal distance is computed by projecting this vector onto

the normal vector of the corresponding surface segment as illustrated in Figure 5.4(b).

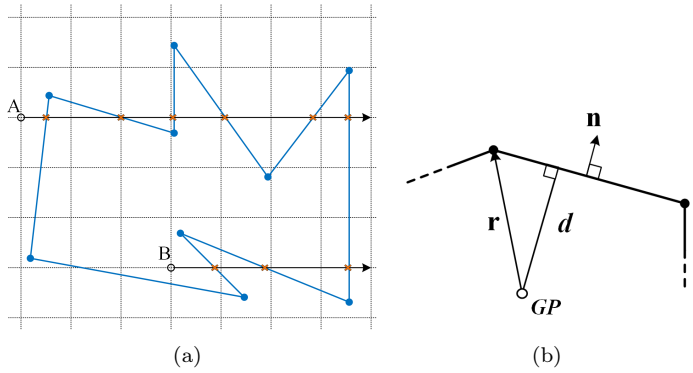

Figure 5.4: (a) Schematic of ray-casting method for 2D point-in-polygon problem. (b) Schematic of point-normal line distance algorithm.

Once the BI and the corresponding IP have been identified, a reconstruction procedure is needed to find the values at the ghost points by taking into account the boundary conditions directly.

5.2.1 Reconstruction Procedure

The reconstruction is built by a polynomial employing the nodal values in the fluid domain and the boundary conditions at the interface. Two kinds of interpolation methods are considered in the present study: bilinear interpolation and weighted least squares method which are analyzed and discussed in detail in our Paper III [56] and Paper IV [55].

5.2.1.1 Bilinear Interpolation

In the case of bilinear interpolation in 2D, the interpolating polynomial involves four nodes and hence four nodal values need to be specified. The bilinear interpolation for a generic variable ϕ can be expressed as

$$\phi(x, y) = C_1 + C_2 x + C_3 y + C_4 xy \tag{5.1}$$

The four unknown coefficients $C_i, i = 1, .., 4$, can be determined using values at the four nodes surrounding the image point. Thus, the variable at the image point is reconstructed through bilinear interpolation using unknown coefficients and known flow variables at surrounding fluid nodes. However,

the approach can be reformulated such that new coefficients are only dependent on the coordinates of the image point and the geometry of the grids [56, 74]. Thus, the image point value can be expressed as

$$\phi_{\mathrm{IP}} = \sum_{i=1}^{4} \alpha_i \phi_i, \tag{5.2}$$

where $\alpha_i, i = 1, ..., 4$, are coefficients depending on the coordinates only. The reformulation is discussed in detail in the Appendix C of our Paper III [56].

There might occur some spacial cases when a ghost point is close to the immersed boundary such that, its corresponding image point does not have four surrounding fluid points. One case would be that the ghost point itself is part of the interpolation scheme. Since the ghost point value in an interpolation scheme would be unknown, the ghost point is then replaced by the body intercept point where the values are determined by the boundary conditions, cf. Figure 5.5(a).

The second case would be that two interpolation points lie inside the immersed body, one at the corresponding ghost point itself and one at another ghost point. The procedure we used to handle this case is to repeat the above steps for the other ghost point as well, cf. Figure 5.5(b).

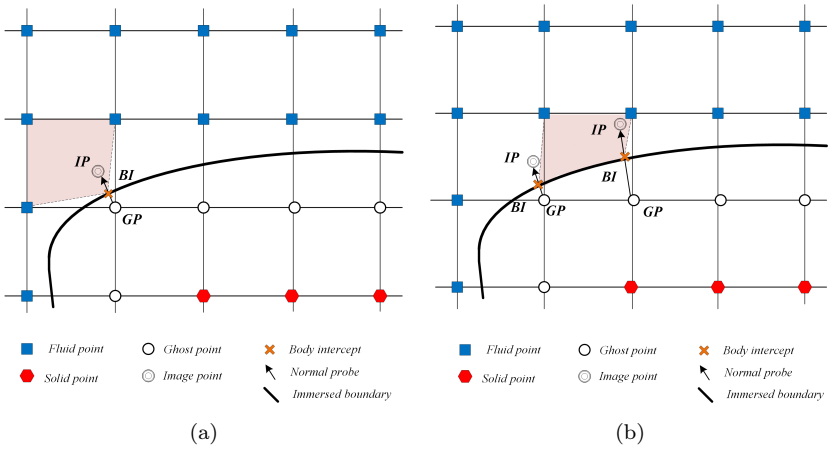

Figure 5.5: (a) Schematic of the situation when one surrounding interpolation point is a body intercept. (b) Schematic of the situation when two of the surrounding interpolation points are body intercepts.

Therefore, the value of the variable at the ghost point is computed by employing a linear approximation along the normal probe which takes into account the boundary condition at the body intercept. For a Dirichlet bound-

ary condition at the body $\phi(x_{\mathrm{BI}}, y_{\mathrm{BI}}) = \phi_{\mathrm{BI}}$, the ghost point value can generally be obtained from $\frac{1}{2}(\phi_{\mathrm{IP}} + \phi_{\mathrm{GP}}) = \phi_{\mathrm{BI}}$, which can be expressed as

$$\phi_{\mathrm{GP}} = \left(2 - \sum_{j \in \mathcal{G}} \alpha_j\right) \phi_{\mathrm{BI}} - \sum_{i \notin \mathcal{G}} \alpha_i \phi_i, \tag{5.3}$$

where $\mathcal{G}$ is the set of body intercepts that are part of the interpolation stencil in special cases.

For a Neumann boundary condition at the immersed boundary $\frac{\partial \phi(x_{\mathrm{BI}}, y_{\mathrm{BI}})}{\partial n} = (\frac{\partial \phi}{\partial n})_{\mathrm{BI}}$, the second order central difference approximation is applied along the normal probe. Note that for Neumann boundary condition the value of $(\frac{\partial \phi}{\partial n})_{\mathrm{BI}}$ are part of the interpolation points, in those spacial cases mentioned above. Therefore, the value at the image point can generally be obtained as

$$\phi_{\mathrm{IP}} = \sum_{j \in \mathcal{G}} \alpha_j \left(\frac{\partial \phi}{\partial n}\right)_{\mathrm{BI}} + \sum_{i \notin \mathcal{G}} \alpha_i \phi_i \tag{5.4}$$

Thereby to second order, the general formulation for a inhomogeneous Neumann boundary condition is obtained form $\frac{\phi_{\mathrm{IP}} - \phi_{\mathrm{GP}}}{\triangle l} = \left(\frac{\partial \phi}{\partial n}\right)_{\mathrm{BI}}$, which can be expressed as

$$\phi_{\mathrm{GP}} = \left(\sum_{j \in \mathcal{G}} \alpha_j - \triangle l\right) \left(\frac{\partial \phi}{\partial n}\right)_{\mathrm{BI}} + \sum_{i \notin \mathcal{G}} \alpha_i \phi_i, \tag{5.5}$$

where $\triangle l$ is the length of the normal probe from the ghost point to the image point.

5.2.1.2 Weighted Least Squares Method

To extend the boundary treatment to high order and to obtain more accurate values at the ghost points that are close to the immersed boundary, a high order polynomial interpolation combined with the weighted least squares method [69, 104] is used, here referred to as WLSQ method. In this approach, the value at the ghost point is determined by imposing the boundary condition at the body intercept point employing a third order polynomial to ensure at least fourth order accuracy of the flow reconstruction. In particular, a generic variable ϕ is approximated around the body intercept point $(x_{\mathrm{BI}}, y_{\mathrm{BI}})$ as follows

$$\phi(x', y') \approx \sum_{i=0}^{r} \sum_{j=0}^{r} C_{i,j}\ {x'}^{i}\ {y'}^{j}, \qquad i + j \leqslant r, \tag{5.6}$$

where r is the order of the polynomial, $x' = x - x_{\mathrm{BI}}$ and $y' = y - y_{\mathrm{BI}}$ are the local coordinates, and $C_{i,j}$ are the coefficients which link the boundary

intercept point to neighbouring points. The number of polynomial coefficients to be determined is $p = (f(r) =)10$ for a third order polynomial in the 2D case. Following [69, 104], the data points are chosen within a circular (spherical in 3D) region of radius R around the body intercept point, as shown in Figure 5.6.

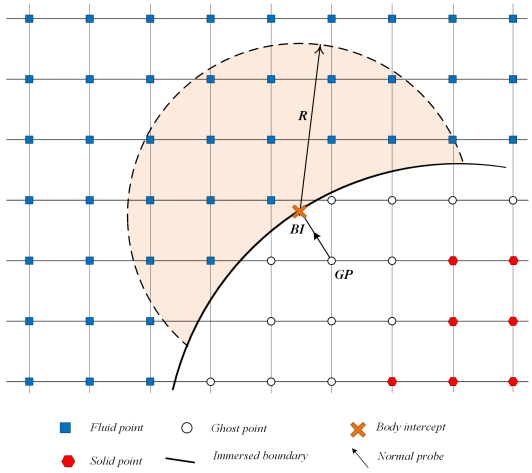

Figure 5.6: Schematic of polynomial approach for boundary treatment.

The unknown coefficients $\mathbf{C}$ can be determined by minimizing the weighted least squares error for q data points.

$$\min_{\mathbf{C}} \sum_{n=1}^{q} (w_n(\mathbf{V}_n\mathbf{C} - \phi_n))^2, \tag{5.7}$$

where n is the n^{th} data point and w_n is the weighting function. The choice of weighting function and more discussions of WLSQ method can be found in our Paper IV [55]. $\mathbf{V}$ is the Vandermonde matrix $\mathbf{V} = \{\mathbf{V}_1^T, \mathbf{V}_2^T, ..., \mathbf{V}_q^T\}^T$ and

$$\mathbf{V}_n = \{1, x^1y^0, x^0y^1, ..., x^{r-1}y^0, x^0y^{r-1}, ..., x^{r-2}y^{r-1}, x^{r-1}y^{r-2}, x^ry^0, x^0y^r\}. \tag{5.8}$$

The coefficients $C_{i,j}$ which are the solution of the weighted least squares problem in Eq. (5.7) are given by

$$\mathbf{C} = (\mathbf{WV})^+\mathbf{W}\phi, \tag{5.9}$$

where the superscript + indicates the pseudo-inverse of a matrix. $\mathbf{C}$ and ϕ are the coefficients and the data variables $\phi_n(x', y')$, respectively. $\mathbf{W}$ is the

weighting matrix. The pseudo-inverse of matrix ($\mathbf{WV}$) is computed by singular value decomposition (SVD) [93]. Multiplying by the weighting matrix gives $\mathbf{M} = (\mathbf{WV})^{+}\mathbf{W}$ which is a $p \times q$ matrix.

Therefore, for a given Dirichlet boundary condition at the body, $\phi(x_{\mathrm{BI}}, y_{\mathrm{BI}}) = \phi_{\mathrm{BI}}$, the ghost point value can be evaluated as

$$\phi_{\mathrm{GP}} = \frac{\phi_{\mathrm{BI}} - \sum_{n=2}^{q} M(1,n) \cdot \phi(x'_n, y'_n)}{M(1,1)}. \tag{5.10}$$

For a given Neumann boundary condition at the body, $\frac{\partial \phi}{\partial n}(x_{\mathrm{BI}}, y_{\mathrm{BI}}) = \zeta$, the ghost point value is computed as

$$\phi_{\mathrm{GP}} = \frac{\zeta - \sum_{n=2}^{q} \Big(n_x M(2,n) + n_y M(3,n) \Big) \cdot \phi(x'_n, y'_n)}{n_x M(2,1) + n_y M(3,1)}, \tag{5.11}$$

where n_x and n_y are the components of the unit vector normal to the boundary.

5.3 Immersed Boundary Method for Summation-by-parts Operators

As mentioned in Section 2.2.2, the high order SBP operators employed in this study for spatial discretization correspond to the sixth order central finite difference method at interior grid points. Thus, they require three layers of ghost points inside the immersed boundary in order to maintain the overall high order of accuracy, as shown in Figure 5.7.

Determining the ghost point values along the aforementioned normal probe works well for handling all layers of ghost points inside the solid body. However, it is constrained to second order accuracy [74], as investigated in detail in our Paper III [56] and Paper IV [55]. To achieve higher accuracy for the IBM, the WLSQ can also be used. Despite the advantage of the WLSQ obtaining high order accuracy, it has to be noted that because in this approach the ghost point is part of the interpolation formulation and it is located outside the domain, it needs to keep the ghost point close to the body intercept point by using fine grids. Furthermore, care has to be taken to have a sufficient number of data points to ensure that the solution is well-defined. On the other hand, by using the image point and bilinear interpolation a second order accurate solution will be achieved. For image points located too close to the immersed boundary, i.e., where one or two ghost points might be part of the interpolation scheme as discussed above in Section 5.2.1.1, the body intercept points need to be used instead which leads to losing a bit of

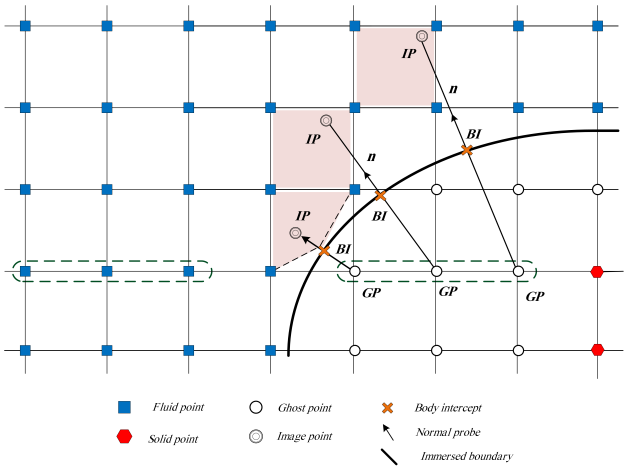

Figure 5.7: Schematic of 3 layers of ghost points inside immersed body on a Cartesian mesh.

accuracy in the weighting coefficients in the interpolation scheme. Therefore, to take advantage of the good features of these two approaches and make it compatible to our solver, a hybrid treatment is employed. In this approach, each layer of ghost points is treated differently. The first layer of ghost points is treated by using a third-order polynomial combined with the WLSQ in order to obtain a higher accuracy near the IB. The second and third layers of ghost points are treated by finding the image points of the corresponding ghost points and using bilinear interpolation to find the values at the image points as illustrated in Figure 5.8.

In this study, second derivatives of the viscous parts of $\hat{\mathbf{F}}_\xi{}'$ and $\hat{\mathbf{G}}_\eta{}'$ in the transformed compressible Navier–Stokes equations (2.13) are approximated by applying the SBP operator for the first derivatives $\frac{\partial}{\partial\xi}$ and $\frac{\partial}{\partial\eta}$, twice. However, successively applying the first derivative operator makes the stencil wider, which requires a special treatment for the immersed boundary method. For the proper treatment to avoid wider stencils in computing the second derivative, the first derivatives of the viscous fluxes are computed up to and including the ghost points in the third layer of ghost points as boundary points and using the globally fourth order SBP operator (2.23) as discussed in Section 2.2.2. The first derivatives of the viscous and inviscid fluxes, i.e. $\hat{\mathbf{F}}'_\xi$ and $\hat{\mathbf{G}}'_\eta$ in Eq. (2.13) are approximated by the standard sixth order central difference method. Using this procedure, we ensure that also the derivatives of the inviscid and viscous fluxes at the fluid points closest to the immersed boundary are computed with high order. Note that the

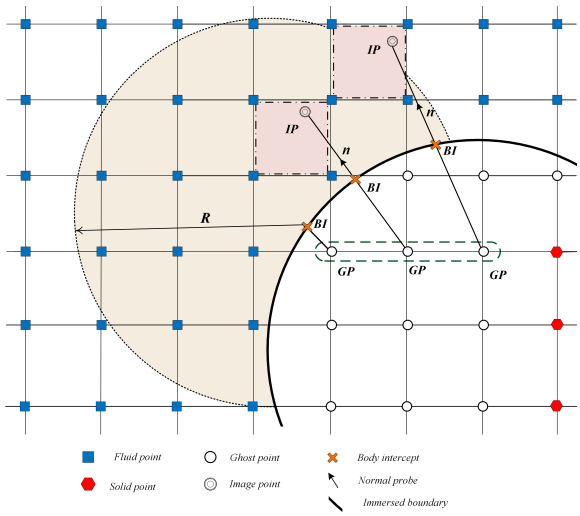

Figure 5.8: Schematic of hybrid treatment, WLSQ method is used for the first layer of ghost point and bilinear interpolation for the second and third layers.

values at the points flagged as solid points are enforced to be zero at the end of each Runge–Kutta stage to avoid obtaining non-physical values for these points lying inside the solid body.

5.4 Moving Boundaries

In this immersed boundary method, the ghost point values need to be updated when the boundaries move. Since the fluid flow equations are solved on a Cartesian grid, all that is needed is to update the values at the ghost points at the beginning of each stage of the Runge–Kutta method. Moving the solid body to the new location at the new time level $n+1$, cf. Figure 5.9, the body intercept points are updated. Next, it is required to recompute the values at the image points and then to obtain the ghost point values prior to advancing the fluid flow equations in time. The algorithm of IBM for moving boundaries from time level n to $n+1$ is described in detail in our Paper V [57].

5.5 Freshly Emerged Fluid Points

One issue encountered with moving boundaries in sharp interface methods is the so-called *fresh-cell* problem [123, 125] or freshly emerged fluid point. This term refers to the situation where a node inside the solid body which

is a solid point at one time step, emerges into the fluid domain at the next time step as the immersed boundary moves across the fixed Cartesian grid. Figure 5.9 shows a 2D schematic where the boundary motion from time level n to time level $n+1$ leads to the appearance of freshly emerged fluid points.

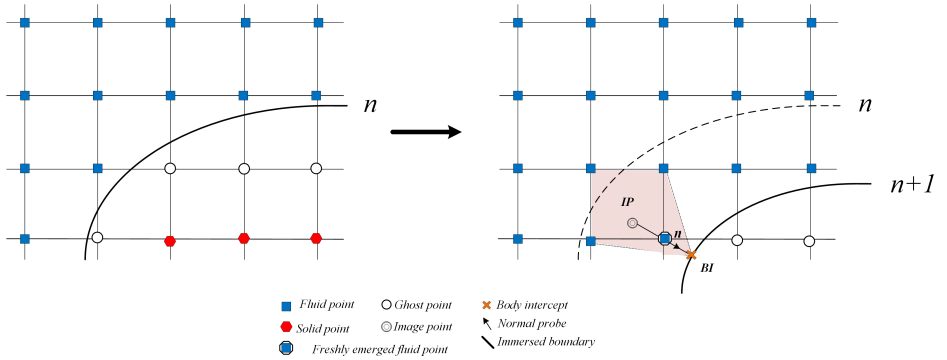

Figure 5.9: Schematic of emergence of fresh fluid points due to the boundary motion from time level n to time level $n+1$, the interpolation stencil is in color for one representative freshly emerged fluid point.

Basically, the spatial discontinuity causes a temporal discontinuity, i.e. the solution at a node changing from solid to fluid from one time step to the next is discontinuous in time because of the moving boundary. Obviously, it is not possible to devise a straightforward temporal discretization of the governing equations for these fresh fluid points, because these points do not have a settled time history [11]. Udaykumar et al. [123] dealt with this issue by combining the freshly emerged fluid points with adjoining fluid points for the first time step right after appearing the freshly emerged fluid point in the fluid domain. In Udaykumar et al. [125] a relatively different approach was chosen to address this issue. The velocity in the freshly emerged fluid point was determined for one time step by applying an interpolation procedure taking the neighbouring points into account [11].

A similar strategy [74, 123] is adopted in the present study. The values of the fresh fluid points are initialized from the neighbouring points surrounding it. As illustrated in Figure 5.9, a normal probe is extended from the fresh fluid node to the immersed boundary at the new time level $n+1$ and this intersects at the body intercept point (BI). An image point (IP) corresponding to the body intercept is then determined and the four nodes surrounding the image point are identified. One of these nodes is necessarily the fresh fluid point itself which is replaced by the body intercept point. Applying a bilinear interpolation in the quadrilateral defined by the four

points surrounding the image point, i.e. three fluid points and the BI point at time level $n + 1$, the value at the fresh fluid point is obtained.

It is worth mentioning that since the explicit numerical methods are constrained by the CFL condition, the immersed boundary motion and thus the time step size is also subject to a similar constraint. Therefore at any given time step the layer of fresh fluid points can at most be one grid layer deep [74]. Therefore, any node that is a freshly emerged fluid point at a given time step was necessarily a ghost point at the previous time step. This is particularly true, in the current IBM where three layers of ghost points are employed.

CHAPTER 6

Summaries of Thesis Papers

This chapter provides a brief overview on the papers listed in the thesis and presents some selected results.

6.1 Paper I: Interaction Between a Simplified Soft Palate and Compressible Viscous Flow

This paper presents numerical simulations of the fluid-structure interaction (FSI) of a simplified 2D model of the upper airways [53], as illustrated in Figure 6.1. This is a well-established model wherein a flexible plate representing the soft palate is mounted at the trailing edge of a rigid plate representing the hard palate. The rigid plate separates the upper and lower channel flows modeling the flow in the oral and nasal tracts, which interact with the flexible plate and then combine into a single channel flow representing the flow in the pharynx [5, 117].

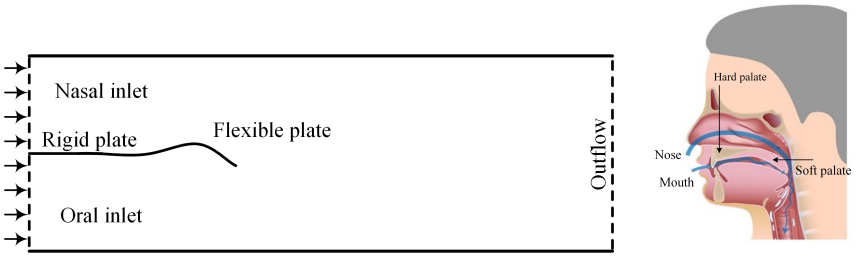

(a) Schematic of the computational model

(b) The anatomy of upper airways.

Figure 6.1: (a) Computational model and (b) real geometry.

The flow-induced oscillation of the soft palate in the pharynx is studied. The soft palate in this paper is modeled as a flexible plate by the linearized

Euler–Bernoulli thin beam theory. The arbitrary Lagrangian–Eulerian formulation is used for handling FSI. The modal analysis of the cantilevered plate is carried out and the computed frequencies of the plate are compared with the corresponding second mode eigenfrequencies of the structure. We tested plates with different mass, stiffness and damping parameters to investigate the oscillation behavior of the flexible plate under different material parameters. We looked into the total, kinetic and strain energies for all cases considered, and found that the oscillation of the plate remains stable.

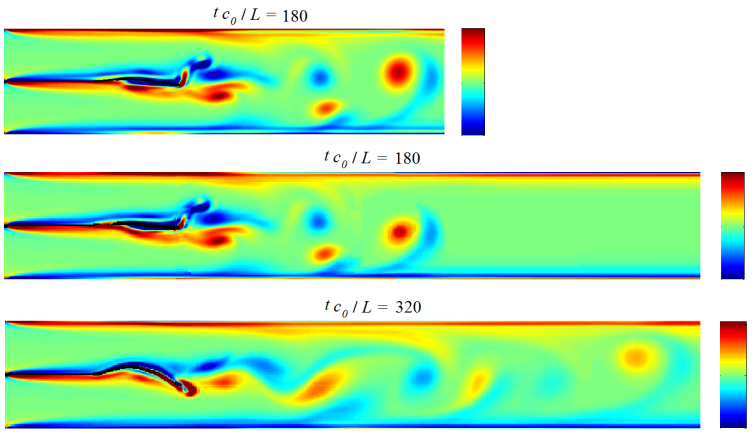

Figure 6.2: Time sequence showing vorticity contour plots, both inlets are open at Re = 378 and Ma = 0.01. The contour levels are from -0.2 s^{-1} to 0.2 s^{-1} corresponding to $-5 \times 10^{-5} \leqslant (\bigtriangledown \times \mathbf{U})_z L/c_0 \leqslant 5 \times 10^{-5}$ and $-5 \times 10^{-3} \leqslant (\bigtriangledown \times \mathbf{U})_z L/U \leqslant 5 \times 10^{-3}$. Snapshots at $tc_0/L = 180$ for large and elongated channels, respectively. Snapshot at $tc_0/L = 320$ for elongated channel.

In Figure 6.2, the vorticity contours for the case when both inlets are open at Re = 378 and Ma = 0.01 is shown. To ensure that the outlet boundary conditions in this channel do not affect the vortices, we repeated this simulation for a longer channel. Figure 6.2 shows the results. The length of the outlet blocks (from trailing edge of the plate towards outlet boundary and the number of grid points in these blocks have been doubled ($6L$ instead of $3L$ in Figure 1 of the paper [53]). The first and second snapshots show the status of the vortices at the same time for these two different channels. The results for the two different channel lengths are in good agreement. The third snapshot in Figure 6.2 shows the vorticity contours for elongated channel at $tc_0/L = 320$.

The acoustic pressure signal is analyzed to study the effect of plate oscillation on generating sound. Although at the given boundary conditions the quarter wave mode, i.e. $f_0 = (1 - Ma^2)(\frac{c}{4L_t})$ where Ma is Mach number, c

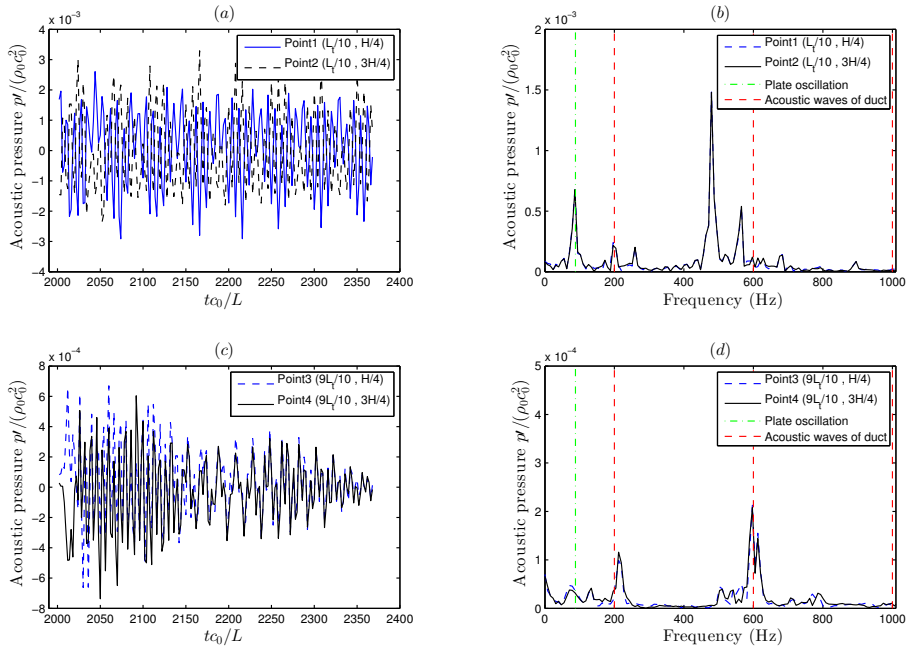

Figure 6.3: (a) and (c) Time history of acoustic pressure $p'/(\rho_0 c_0^2)$ at inlet and outlet, respectively; (b) and (d) Spectrum of pressure signal. The fluid flow is at $\mathrm{Re} = 378$ and $\mathrm{Ma} = 0.01$. The flexible plate was released at $tc_0/L = 2000$.

the speed of sound and L_t is the total length of the channel, is identified as the dominant frequency, the frequency of the sound produced by the plate oscillation is in good agreement with the frequency of the plate oscillation $f = 91.5$Hz. However, the quarter wave frequency and its harmonics dominate the oscillation frequency, as long as the acoustic waves have not yet decayed sufficiently. Figure 6.3 illustrates the time history of the acoustic pressure and the frequency of the acoustic pressure spectrum for this simulation. After turning on the fluid-structure interaction at $tc_0/L = 2000$, the frequency of the oscillation of the flexible plate can be observed better due to the decayed acoustic wave amplitudes.

6.2 Paper II: Computational Study of Flow-induced Oscillation of a Simplified Soft Palate

This paper is an extension of Paper I where a more faithful biomechanical system by modeling the motion of a two-dimensional inextensible flexible plate is studied [54]. This paper presents a two-dimensional numerical simulation to study fluid-structure interaction of a simplified model of the soft palate in the pharynx for uniform inhalation.

In many previous studies [5, 47, 116], linear structural mechanics was taken into account by using the one-dimensional Euler–Bernoulli beam equation. In this study another structural model has been developed by including an inextensibility condition, however, only for a hinged free-end flexible plate.

Vortex dynamics is assessed for the coupled fluid-structure system when both inlets are open. Closer inspection of the pressure fields shows that the plate oscillation produces a strong acoustic wave near the trailing edge of the plate. The complexity of the reflections and the vicinity of the inlet boundary, where uniform flow is imposed to the trailing edge lead to a build-up of vortices near the inlet as shown in Figure 6.4.

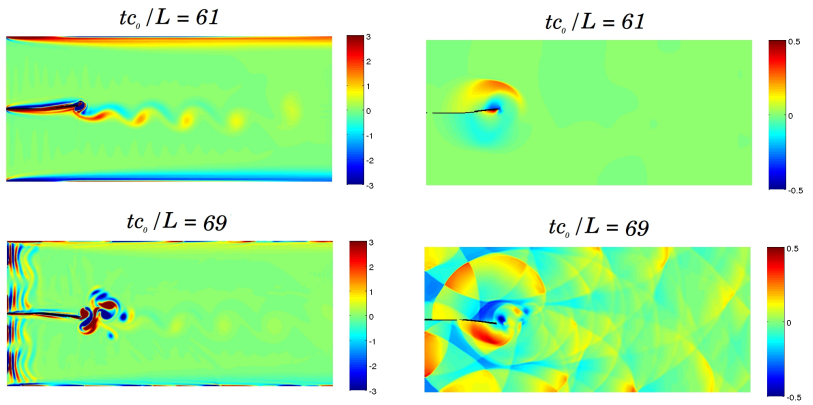

Figure 6.4: The left column shows the time sequence of vorticity contour plots, $\frac{\omega_z L}{c_0}$, and the right column presents the corresponding acoustic pressure contour plots, $\frac{p'}{\rho_0 c_0}$, at Re = 378 and Ma = 0.1.

6.3 Paper III: Immersed Boundary Method for the Compressible Navier–Stokes Equations Using High Order Summation-by-parts Difference Operators

This paper introduces the initial development of the immersed boundary method for our fluid solver [56]. In this paper, the ghost point IB approach has been adopted for a high order finite difference method based on summation-by-parts (SBP) operators to provide an accurate and efficient approach for studying low Mach number compressible viscous flows. The immersed boundaries are treated as sharp interfaces by enforcing the solid wall boundary conditions via flow variables at ghost points using bilinearly interpolated flow variables at the image points of corresponding ghost points. Using this strategy, second order convergence is achieved even by using a fourth order finite difference method, as we investigated in this paper.

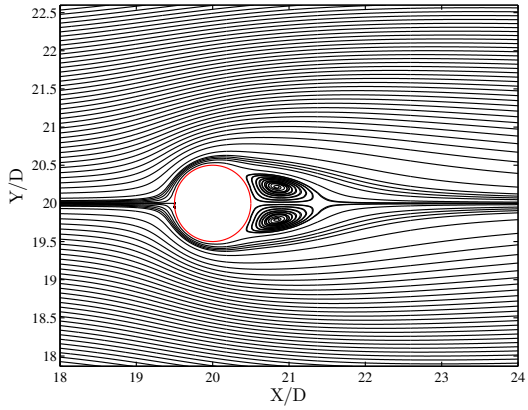

Figure 6.5: Streamlines for computed flow past a circular cylinder at Re = 20 and Ma = 0.03.

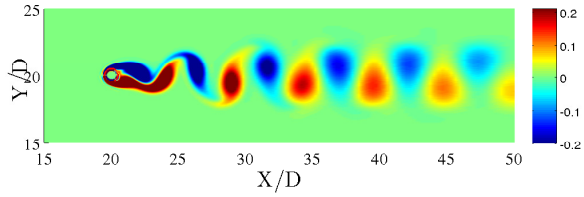

Figure 6.6: Vorticity contours for computed flow past a circular cylinder at Re = 100 and Ma = 0.25.

The methodology is applied to compute steady and unsteady flow problems to demonstrate its versatility as well as its accuracy. The flow past a circular cylinder for moderate values of Reynolds number and Mach number is assessed. Figure 6.5 shows streamlines for Re = 20 and Ma = 0.03. Figure 6.6 presents the instantaneous spanwise vorticity ω_z contours for Re = 100 and Ma = 0.25 indicating the presence of the von Kármán vortex street.

6.4 Paper IV: High Order Immersed Boundary Method for Viscous Compressible Flows based on Summation-by-parts Operators

This paper is a significant extension of Paper III, because in this paper, a high order immersed boundary method is devised [55]. Two different interpolation schemes are tested to compute values at the ghost points. The first method provides the bilinearly interpolated flow variables at the image points of the corresponding ghost points, as we discussed in Paper III, and the second method applies the boundary condition at the immersed boundary by using the weighted least squares (WLSQ) method with high order polynomials. The spatial accuracy of the two different reconstruction procedures are separately verified by solving the steady state heat equation. High order accuracy is achieved by the WLSQ method. A hybrid treatment is used for flow past a circular cylinder. The convergence results for flow past a circular cylinder at Re = 20 and Ma = 0.03 and Ma = 0.1 confirm that the current fluid flow solver with the hybrid treatment of the immersed boundary is globally third order accurate, as shown in Figure 6.7 for Re = 20 and Ma = 0.1. Figure 6.7 shows the norms of the relative errors of the primitive variables ρ, u, v, p when the grid size changes.

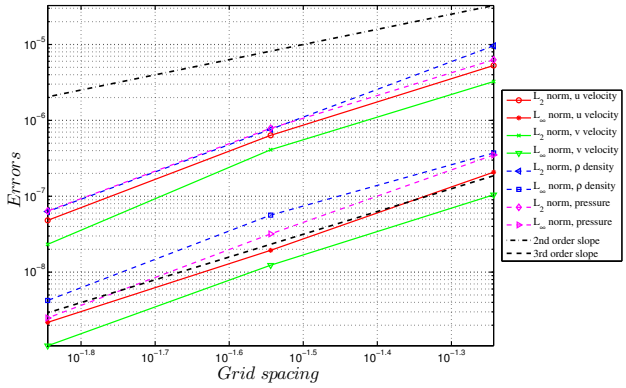

Figure 6.7: L_2 and L_∞ norms of the relative errors of the velocity components, density and pressure computed at various grid levels for flow past a circular cylinder at Re = 20 and Ma = 0.1.

Finally, the versatility of the present method in dealing with complex immersed boundaries is demonstrated by simulating flows in the sagittal cross-section of the upper airways of an obstructive sleep apnea patient. In the present study, the cross-section of the upper airways for a patient in the study by [77], a 67-year-old man who showed great improvement in AHI

(Apnea Hypopnea Index) after a septum plastic surgery in the nasal cavity is considered. In Figure 6.8(a), the computational grid for the 2D geometry of the upper airways in the sagittal plane is shown. A Cartesian grid with a total 991×381 grid points is employed and the domain is resolved with uniform grid spacing. Figure 6.8(b) presents the vorticity contours at time instant $tc_0/D = 1060$ for fluid flow at $\mathrm{Re} = 2000$ and $\mathrm{Ma} = 0.1$.

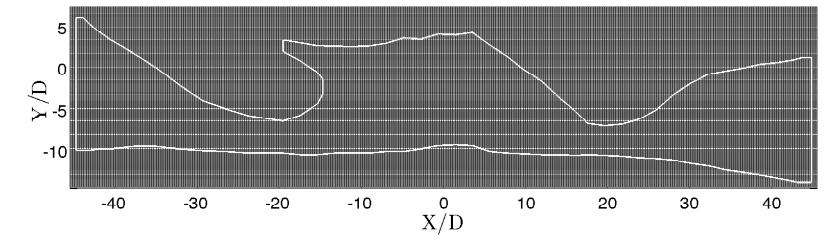

(a)

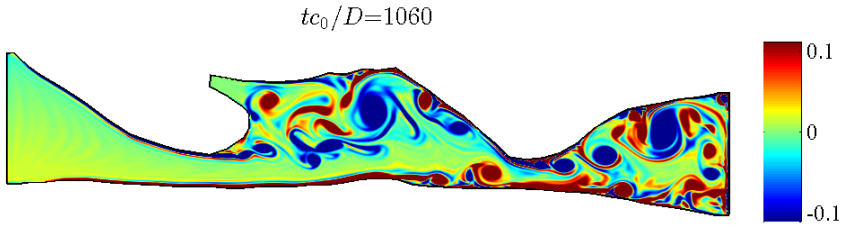

(b)

Figure 6.8: (a) Computational grid for upper airway simulation (every 3rd grid point is plotted). The boundary of the flow domain is shown in white. (b) Vorticity contours for flow in the human upper airway at $\mathrm{Re} = 2000$ and $\mathrm{Ma} = 0.1$.

6.5 Paper V: Immersed Boundary Method for Viscous Compressible Flows around Moving Bodies

In this paper, the immersed boundary method developed for moving boundaries by employing high order SBP operators is presented [57]. As in Paper III, the boundary conditions of the immersed moving boundaries are enforced through a linear reconstruction procedure employing image points and ghost points. The values at the image points are computed by bilinear interpolation using four nodal fluid points surrounding the image points. Numerical simulations for compressible viscous flows induced by a transversely oscillating circular cylinder in free-stream and a harmonic in-line oscillating circular cylinder in quiescent fluid are presented and compared with experiments and incompressible fluid flow simulations which used body-conforming grid methods.

In a transversely oscillating circular cylinder immersed in free-stream [37, 38], the oscillation amplitude A and the excitation frequency f_e are two important parameters. The transverse motion of the cylinder is given by a harmonic oscillation in y-direction. We performed the computations at $\mathrm{Re} = 185, \mathrm{Ma} = 0.25$, $\frac{A}{D} = 0.2$ where D is the diameter of the cylinder and $0.8 \leqslant f_e/f_o \leqslant 1.2$ where f_o is the natural shedding frequency for a stationary cylinder. Figure 6.9 presents the instantaneous streamlines with modulus velocity contours in the left column and instantaneous spanwise vorticity ω_z contours in the right column when the cylinder is at its highest upper position. It is observed that the wake pattern changes as f_e/f_0 increases.

In the case of an in-line oscillating cylinder in a fluid initially at rest [23], there are two non-dimensional parameters that characterize the flow induced by the motion of the cylinder. The first one is the Reynolds number $\mathrm{Re} = \frac{U_{max} D}{\nu}$ where U_{max} is the maximum velocity of the cylinder during oscillation, D the diameter of the cylinder and ν is the kinematic viscosity of the flow at rest. The second one is the Keulegan–Carpenter number $\mathrm{KC} = \frac{U_{max}}{D f_e}$ where f_e is the excitation frequency of the oscillation. The translational motion of the cylinder is given by a harmonic oscillation in x-direction.

Fig. 6.10 shows instantaneous spanwise vorticity ω_z contours in the left column when the cylinder is at two different phase positions ($2\pi f t = 0°$, 288°). The contours of the instantaneous acoustic pressure fluctuation $\tilde{p}' = p'(x, y, t) - \bar{p}'(x, y)$ non-dimensionalized by $\rho_0 c_0^2$ are presented in 6.10, in the right column clearly show the presence of the generated acoustic waves inside the domain. The pressure perturbation $p'(x, y, t)$ is reduced by the mean pressure $\bar{p}'(x, y)$ integrated over some periods of vortex shedding.

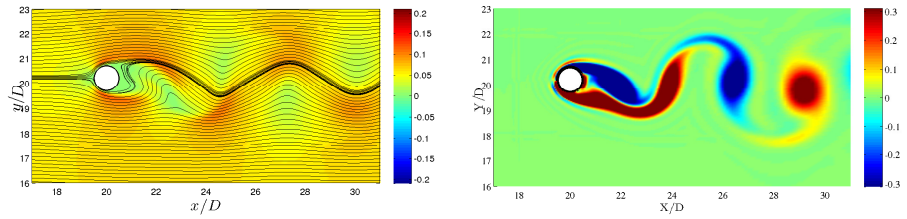

(a) $f_e/f_o = 0.8$

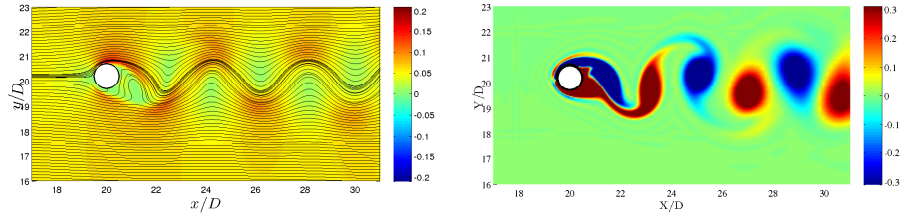

(b) $f_e/f_o = 1$

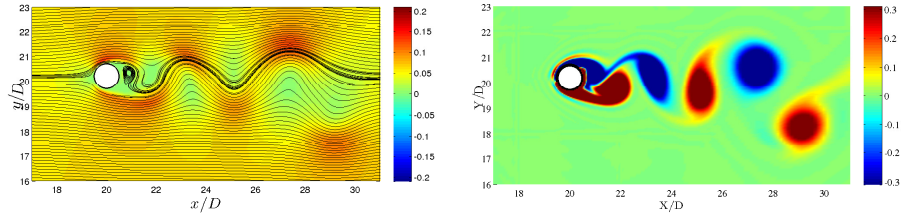

(c) $f_e/f_o = 1.2$

Figure 6.9: Instantaneous streamlines and velocity modulus distribution (left column) and instantaneous vorticity contours (right column) of transversely oscillation of cylinder at Re = 185, Ma = 0.25 and $A/D = 0.2$ for different $f_e/f_0 = 0.8, 1, 1.2$. In all frames, the location of the cylinder is at its extreme upper position for all values.

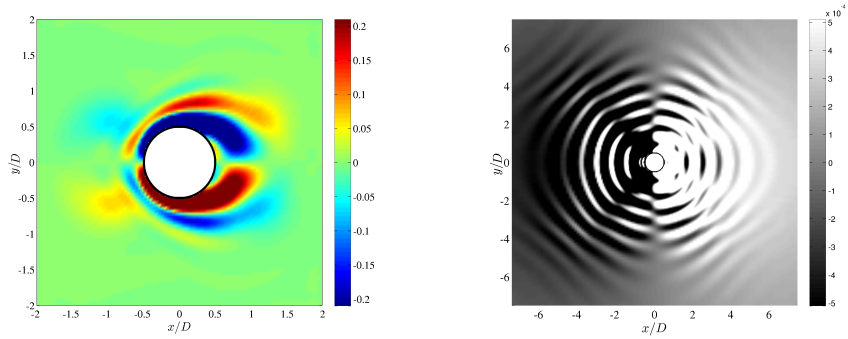

(a) 0°

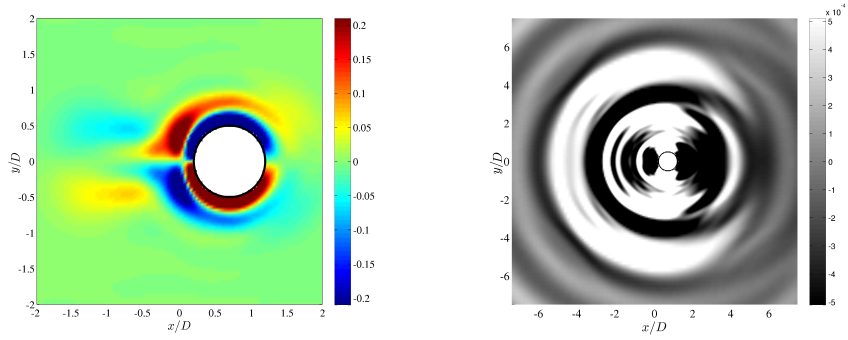

(b) 288°

Figure 6.10: Instantaneous vorticity contours of in-line oscillation in left column and instantaneous acoustic pressure fluctuation $\tilde{p}'$ in right column, for two different phase angle positions $2\pi f_e t =$ (a) 0°, (b) 288° at Re = 100, KC = 5 and Ma =0.03.

6.6 Contributions to Papers

The manuscripts were written by me. The numerical simulations and the analysis of numerical results reported in the manuscripts were performed by me. M. Larsson and B. Müller contributed with insightful comments around the details of the manuscripts and reported results and the arrangements of the contents. The compressible Navier–Stokes code based on SBP operators for body-conforming grids using NSCBC was developed by B. Müller and extended to an ALE solver by M. Larsson before starting my Ph.D. project. The structural models were developed by me. Implementation of the multi-block approach using MPI and development of the IBM were performed by me. M. Larsson contributed with suggestions and discussions around the details of the implementation.

CHAPTER 7

Concluding Remarks

7.1 Conclusions

The main findings and achievements of both fluid-structure interaction simulations for a simplified model of the upper airways and the immersed boundary method to study fluid flow over bodies with complex and moving boundaries are discussed.

7.1.1 FSI Simulation on the Upper Airways

To take a step towards the understanding of disorders of the obstructive sleep apnea syndrome and snoring induced by fluid-structure interaction (FSI), we have developed a simplified model of the upper airways. The inspiratory airflow is described by the 2D compressible Navier–Stokes equations, and the soft palate is modeled as a flexible plate by the linearized Euler–Bernoulli thin beam theory and further by a 2D inextensible beam. FSI is handled by the arbitrary Lagrangian–Eulerian (ALE) formulation. Moving mesh compatibility with high order SBP operators is achieved by developing a multi-block approach. The dynamics of the vortices produced by the interaction of the fluid flow and the structure is investigated. Several cases are presented to investigate the oscillation behaviour of the flexible plate under different material parameters of mass, damping and stiffness. For all cases considered, the oscillation of the plate remains stable. In order to identify the effect of plate oscillation as a source of sound generation, the acoustic pressure is analyzed.

7.1.2 IBM for Complex and Moving Boundaries

Aside from good features of body-conforming methods like the ALE method for CFD and FSI problems as discussed in Section 1.3, body-conforming ap-

proaches face some issues related to the mesh generation and mesh deformation for complex geometries.

A ghost-point immersed boundary for the compressible Navier–Stokes equations to deal with complex and moving boundaries on fixed Cartesian grids is devised by employing high order SBP difference operators. The immersed boundaries are treated as sharp interfaces by enforcing the solid wall boundary conditions via flow variables at ghost points using either bilinearly interpolated flow variables at image points or a high-order interpolation using a weighted least squares method. A hybrid method is applied to achieve an efficient and high order immersed boundary method (IBM) formulation with SBP operators. The methodology is applied to compute steady and unsteady flow problems demonstrating its versatility as well as its accuracy. The present method is then applied to the sagittal cross-section of the real geometry of a human upper airways to demonstrate its capability for dealing with complex geometries in practical applications.

The current IBM is extended to handle moving boundaries. The new IBM is verified and validated for a transversely oscillating circular cylinder and an in-line oscillating circular cylinder.

7.2 Future Outlook

There are many opportunities for extending the scope of this dissertation. This section presents some of these directions.

In the present dissertation, a preliminary study was performed to examine the fluid-structure interaction in the upper airways. The development of FSI models for diagnosis and treatment of OSAS or snoring may favour simplified and efficient models for clinical analysis. However, idealised models need to be verified and validated by realistic models and clinical experiments, respectively, in order to appropriately assess their accuracy and assumptions. Therefore, three-dimensional (3D) FSI models with patient-specific features permitting to study OSAS and snoring in detail are required.

In this study, a linear elastic deformation model is used with thin plate mechanics. However, the soft tissues involved in the upper airways and the soft palate undergo displacements and deformations beyond the linear range. Therefore, non-linear elastic models with thickness can represent them more accurately.

In order to ensure the energy transfer between the numerical methods of the fluid and structure solvers, the traction boundary condition can be derived in the simultaneous approximation terms (SAT) framework to obtain a strictly stable method. Furthermore, more acoustic studies can be

performed to investigate the relations between the frequency spectrum of sound waves and model parameters.

There is room for improvement of the present ghost-point immersed boundary method. It would be desirable to increase the second order spatial accuracy of enforcing boundary conditions at ghost points using bilinearly interpolated flow variables at image points. Future research can consider alternative formulations of enforcing boundary conditions using irregular discrete operators near the immersed boundary. Higher order polynomial methods can be used to obtain the values at the image points for high Reynolds number flows. Applying SBP finite difference operators for self-adjoint operators can improve the overall accuracy for second derivatives as well.

Moreover, the block structured grid employed in the present study can be improved by employing adaptive mesh refinement (AMR) approaches. AMR methods can be used to obtain solutions with the same accuracy as the uniform grid methods on fine grids, but at a lower computational cost by distributing the structured mesh more efficiently in certain regions.

We found the developed IB method to be robust, versatile and ready to be applied to other settings. The solver can be further developed to accommodate more complex simulations, particularly 3D patient specific geometries of the upper airways. Therefore, 3D flows around stationary, flexible surfaces and flow-induced vibrations can be explored in the future for applications in biological flows.

While the IBM was only applied to fluid flows around moving bodies, the interaction between fluid flows and deforming bodies can be investigated by the same strategy.

Bibliography

[1] Agrawal, S., Stone, P., McGuinness, K., Morris, J., Camilleri, A., 2002. Sound frequency analysis and the site of snoring in natural and induced sleep. Clinical Otolaryngology 27 (3), 162–166.

[2] Araghi, M. H., Chen, Y.-F., Jagielski, A., Choudhury, S., Banerjee, D., Hussain, S., Thomas, G. N., Taheri, S., 2013. Effectiveness of lifestyle interventions on obstructive sleep apnea (OSA): Systematic review and meta-analysis. Sleep 36 (10), 1553–1562.

[3] Ayappa, I., Rapoport, D. M., 2003. The upper airway in sleep: Physiology of the pharynx. Sleep Medicine Reviews 7 (1), 9–33.

[4] Balaras, E., 2004. Modeling complex boundaries using an external force field on fixed Cartesian grids in large-eddy simulations. Computers & Fluids 33 (3), 375–404.

[5] Balint, T., Lucey, A., 2005. Instability of a cantilevered flexible plate in viscous channel flow. Journal of Fluids and Structures 20 (7), 893–912.

[6] Bathe, K., Saunders, H., 1984. Finite element procedures in engineering analysis. American Society of Mechanical Engineers, New York.

[7] Bauchau, O. A., Craig, J. I., 2009. Structural Analysis: With Applications to Aerospace Structures. Springer, New York.

[8] Bearpark, H., Elliott, L., Grunstein, R., Cullen, S., Schneider, H., Althaus, W., Sullivan, C., 1995. Snoring and sleep apnea. a population study in Australian men. American Journal of Respiratory and Critical Care Medicine 151 (5), 1459–1465.

[9] Bertram, C. D., 2008. Flow-induced oscillation of collapsed tubes and airway structures. Respiratory Physiology & Neurobiology 163 (1), 256–265.

[10] Borazjani, I., Ge, L., Sotiropoulos, F., 2008. Curvilinear immersed boundary method for simulating fluid structure interaction with complex 3D rigid bodies. Journal of Computational Physics 227 (16), 7587–7620.

[11] Brehm, C., Barad, M. F., Kiris, C. C., 2016. An immersed boundary method for solving the compressible Navier-Stokes equations with fluid-structure interaction. In: 54th AIAA Aviation and Aeronautics Forum, Washington, DC.

[12] Brehm, C., Hader, C., Fasel, H. F., 2015. A locally stabilized immersed boundary method for the compressible Navier–Stokes equations. Journal of Computational Physics 295, 475–504.

[13] Cai, S., 2016. Computational fluid-structure interaction with the moving immersed boundary method. Ph.D. thesis, Université de Technologie de Compiègne.

[14] Carpenter, M. H., Gottlieb, D., Abarbanel, S., 1994. Time-stable boundary conditions for finite-difference schemes solving hyperbolic systems: Methodology and application to high-order compact schemes. Journal of Computational Physics 111 (2), 220–236.

[15] Cebral, J. R., 1996. Loose coupling algorithms for fluid-structure interaction. Ph.D. thesis, George Mason University.

[16] Childress, S., 1981. Mechanics of swimming and flying. Vol. 2. Cambridge University Press, Cambridge.

[17] Clarke, D. K., Hassan, H., Salas, M., 1986. Euler calculations for multielement airfoils using Cartesian grids. AIAA journal 24 (3), 353–358.

[18] De Jalon, J. G., Bayo, E., 2012. Kinematic and dynamic simulation of multibody systems: The real-time challenge. Springer Science & Business Media, New York.

[19] De Palma, P., De Tullio, M., Pascazio, G., Napolitano, M., 2006. An immersed-boundary method for compressible viscous flows. Computers & Fluids 35 (7), 693–702.

[20] De Tullio, M. D., De Palma, P., Iaccarino, G., Pascazio, G., Napolitano, M., 2007. An immersed boundary method for compressible flows using local grid refinement. Journal of Computational Physics 225 (2), 2098–2117.

[21] Donea, J., Giuliani, S., Halleux, J., 1982. An arbitrary Lagrangian-Eulerian finite element method for transient dynamic fluid-structure interactions. Computer Methods in Applied Mechanics and Engineering 33 (1), 689 – 723.

[22] Donea, J., Huerta, A., Ponthot, J.-P., Rodriguez-Ferran, A., 2004. Encyclopedia of computational mechanics vol. 1: Fundamentals., Chapter 14: Arbitrary Lagrangian-Eulerian methods.

[23] Dütsch, H., Durst, F., Becker, S., Lienhart, H., 1998. Low-Reynolds-number flow around an oscillating circular cylinder at low Keulegan–Carpenter numbers. Journal of Fluid Mechanics 360, 249–271.

[24] Eckert, D. J., Malhotra, A., 2008. Pathophysiology of adult obstructive sleep apnea. Proceedings of the American Thoracic Society 5 (2), 144–153.

[25] Epstein, L., Kristo, D., Strollo, P., Friedman, N., Malhotra, A., P. Patil, S., Ramar, K., Rogers, R., Schwab, R. J., M. Weaver, E., Weinstein, M. D., 2009. Clinical guideline for the evaluation, management and long-term care of obstructive sleep apnea in adults. Journal of Clinical Sleep Medicine 5 (3), 263.

[26] Fadlun, E., Verzicco, R., Orlandi, P., Mohd-Yusof, J., 2000. Combined immersed-boundary finite-difference methods for three-dimensional complex flow simulations. Journal of Computational Physics 161 (1), 35–60.

[27] Gatti, P., Ferrari, V., 1999. Applied Structural and Mechanical Vibrations: Theory, Methods and Measuring Instrumentation. E & FN Spon, London.

[28] Gehr, P., 1994. Annexe A. Anatomy and morphology of the respiratory tract. Annals of the ICRP 24 (1), 121–166.

[29] Ghias, R., Mittal, R., Dong, H., 2007. A sharp interface immersed boundary method for compressible viscous flows. Journal of Computational Physics 225 (1), 528–553.

[30] Gibou, F., Fedkiw, R., 2005. A fourth order accurate discretization for the Laplace and heat equations on arbitrary domains, with applications to the stefan problem. Journal of Computational Physics 202 (2), 577–601.

[31] Giles, T. L., Lasserson, T. J., Smith, B., White, J., Wright, J., Cates, C. J., 2006. Continuous positive airways pressure for obstructive sleep apnoea in adults. Cochrane Database Systematic Reviews 3 (3).

[32] Gilmanov, A., Sotiropoulos, F., 2005. A hybrid Cartesian/immersed boundary method for simulating flows with 3D, geometrically complex, moving bodies. Journal of Computational Physics 207 (2), 457 – 492.

[33] Gilmanov, A., Sotiropoulos, F., Balaras, E., 2003. A general reconstruction algorithm for simulating flows with complex 3D immersed boundaries on Cartesian grids. Journal of Computational Physics 191 (2), 660–669.

[34] Goldstein, D., Handler, R., Sirovich, L., 1993. Modeling a no-slip flow boundary with an external force field. Journal of Computational Physics 105 (2), 354–366.

[35] Goldstein, D., Handler, R., Sirovich, L., 1995. Direct numerical simulation of turbulent flow over a modelled riblet-covered surface. Journal of Fluid Mechanics 302 (10), 333–376.

[36] González, C., LLorca, J., 2005. Stiffness of a curved beam subjected to axial load and large displacements. International Journal of Solids and Structures 42 (5), 1537–1545.

[37] Gu, W., Chyu, C., Rockwell, D., 1994. Timing of vortex formation from an oscillating cylinder. Physics of Fluids 6 (11), 3677–3682.

[38] Guilmineau, E., Queutey, P., 2002. A numerical simulation of vortex shedding from an oscillating circular cylinder. Journal of Fluids and Structures 16 (6), 773–794.

[39] Günther, C., Meinke, M., Schröder, W., 2014. A flexible level-set approach for tracking multiple interacting interfaces in embedded boundary methods. Computers & Fluids 102, 182–202.

[40] Gustafsson, B., 2008. High order difference methods for time dependent PDE. Springer, Berlin.

[41] Gustafsson, B., Kreiss, H.-O., Oliger, J., 1995. Time dependent problems and difference methods. John Wiley & Sons, New York.

[42] Häggström, M., 2014. Medical gallery of blausen medical. Wikiversity Journal of Medicine 1 (2).

[43] Haines, E., 1994. Point in polygon strategies. Graphics Gems IV 994, 24–26.

[44] Han, S. M., Benaroya, H., Wei, T., 1999. Dynamics of transversely vibrating beams using four engineering theories. Journal of Sound and Vibration 225 (5), 935 – 988.

[45] Hartmann, D., Meinke, M., Schröder, W., 2011. A strictly conservative Cartesian cut-cell method for compressible viscous flows on adaptive grids. Computer Methods in Applied Mechanics and Engineering 200 (9), 1038–1052.

[46] Hou, G., Wang, J., Layton, A., 2012. Numerical methods for fluid-structure interaction-a review. Communications in Computational Physics 12 (2), 337–377.

[47] Howell, R., Lucey, A., Carpenter, P., Pitman, M., 2009. Interaction between a cantilevered-free flexible plate and ideal flow. Journal of Fluids and Structures 25 (3), 544–566.

[48] Hu, H. H., Patankar, N. A., Zhu, M., 2001. Direct numerical simulations of fluid-solid systems using the arbitrary Lagrangian–Eulerian technique. Journal of Computational Physics 169 (2), 427–462.

[49] Huang, L., 1995. Flutter of cantilevered plates in axial flow. Journal of Fluids and Structures 9 (2), 127–147.

[50] Huang, W.-X., Shin, S. J., Sung, H. J., 2007. Simulation of flexible filaments in a uniform flow by the immersed boundary method. Journal of Computational Physics 226 (2), 2206–2228.

[51] Hübner, B., Walhorn, E., Dinkler, D., 2004. A monolithic approach to fluid–structure interaction using space-time finite elements. Computer Methods in Applied Mechanics and Engineering 193 (23), 2087–2104.

[52] Hughes, T. J., 2012. The finite element method: Linear static and dynamic finite element analysis. Courier Corporation, New York.

[53] Khalili, M., Larsson, M., Müller, B., 2016. Interaction between a simplified soft palate and compressible viscous flow. Journal of Fluids and Structures 67, 85–105.

[54] Khalili, M. E., Larsson, M., Müller, B., 2017. Computational study of flow-induced oscillation of a simplified soft palate. In: Coupled Problems in Science and Engineering VII. CIMNE, pp. 582–593.

[55] Khalili, M. E., Larsson, M., Müller, B., 2017. High order immersed boundary method for compressible viscous flows based on summation-by-parts operators. Submitted for Journal Publication.

[56] Khalili, M. E., Larsson, M., Müller, B., 2017. Immersed boundary method for the compressible Navier–Stokes equations using high order summation-by-parts difference operators. In: Proceedings of the 12th International Conference on Computational Fluid Dynamics In the Oil & Gas, Metallurgical and Process Industries. SINTEF, pp. 233–242.

[57] Khalili, M. E., Larsson, M., Müller, B., 2017. Immersed boundary method for viscous compressible flows around moving bodies. Submitted for Journal Publication.

[58] Kim, J., Moin, P., 1985. Application of a fractional-step method to incompressible Navier-Stokes equations. Journal of Computational Physics 59 (2), 308–323.

[59] Kirkpatrick, M., Armfield, S., Kent, J., 2003. A representation of curved boundaries for the solution of the Navier–Stokes equations on a staggered three-dimensional Cartesian grid. Journal of Computational Physics 184 (1), 1–36.

[60] Lacarbonara, W., Paolone, A., Yabuno, H., 2004. Modeling of planar nonshallow prestressed beams towards asymptotic solutions. Mechanics Research Communications 31 (3), 301–310.

[61] Lai, M.-C., Peskin, C. S., 2000. An immersed boundary method with formal second-order accuracy and reduced numerical viscosity. Journal of Computational Physics 160 (2), 705–719.

[62] Laizet, S., Lamballais, E., 2009. High-order compact schemes for incompressible flows: A simple and efficient method with quasi-spectral accuracy. Journal of Computational Physics 228 (16), 5989–6015.

[63] Lam, J., Sharma, S., Lam, B., 2010. Obstructive sleep apnoea: Definitions, Epidemiology & Natural history. Indian Journal of Medical Research 131, 165–170.

[64] Larsson, M., Müller, B., 2012. High–order numerical simulation of fluid–structure interaction in the human larynx. Progress in Computational Fluid Dynamics, an International Journal 12 (2-3), 164–175.

[65] Lasheras, J. C., 2007. The biomechanics of arterial aneurysms. Annual Review of Fluid Mechanics 39, 293–319.

[66] Lim, J., Lasserson, T. J., Fleetham, J., Wright, J. J., 2006. Oral appliances for obstructive sleep apnoea. The Cochrane Library 1, 1–73.

[67] Linnick, M. N., Fasel, H. F., 2005. A high-order immersed interface method for simulating unsteady incompressible flows on irregular domains. Journal of Computational Physics 204 (1), 157–192.

[68] Lumeng, J. C., Chervin, R. D., 2008. Epidemiology of pediatric obstructive sleep apnea. Proceedings of the American Thoracic Society 5 (2), 242–252.

[69] Luo, H., Mittal, R., Zheng, X., Bielamowicz, S. A., Walsh, R. J., Hahn, J. K., 2008. An immersed-boundary method for flow–structure interaction in biological systems with application to phonation. Journal of Computational Physics 227 (22), 9303–9332.

[70] MadaniKermani, S., 2014. Application of immersed boundary method to rlexible riser problem. Ph.D. thesis, Brunel University London.

[71] Majumdar, S., Iaccarino, G., Durbin, P., 2001. RANS solvers with adaptive structured boundary non-conforming grids. Annual Research Briefs, Center for Turbulence Research, Stanford University, 353–466.

[72] Malhotra, A., Huang, Y., Fogel, R. B., Pillar, G., Edwards, J. K., Kikinis, R., Loring, S. H., White, D. P., 2002. The male predisposition to pharyngeal collapse: Importance of airway length. American Journal of Respiratory and Critical Care Medicine 166 (10), 1388–1395.

[73] McNicholas, W., Bonsignore, M., of EU Cost Action B26, M. C., et al., 2007. Sleep apnoea as an independent risk factor for cardiovascular disease: Current evidence, basic mechanisms and research priorities. European Respiratory Journal 29 (1), 156–178.

[74] Mittal, R., Dong, H., Bozkurttas, M., Najjar, F., Vargas, A., von Loebbecke, A., 2008. A versatile sharp interface immersed boundary method for incompressible flows with complex boundaries. Journal of Computational Physics 227 (10), 4825–4852.

[75] Mittal, R., Iaccarino, G., 2005. Immersed boundary methods. Annual Review of Fluid Mechanics 37, 239–261.

[76] Mohd-Yusof, J., 1997. Combined immersed-boundary/B-spline methods for simulations of flow in complex geometries. Center for Turbulence Research Annual Research Briefs, 317 – 325.

[77] Moxness, M. H. S., Nordgård, S., 2014. An observational cohort study of the effects of septoplasty with or without inferior turbinate reduction in patients with obstructive sleep apnea. BMC Ear, Nose and Throat Disorders 14 (1), 11.

[78] Müller, B., 1996. Computation of compressible low Mach number flow. Habilitation Thesis, ETH Zurich.

[79] Müller, B., 2008. High order numerical simulation of aeolian tones. Computers & Fluids 37 (4), 450–462.

[80] Namtvedt, S. K., Randby, A., Einvik, G., Hrubos-Strøm, H., Somers, V. K., Røsjø, H., Omland, T., 2011. Cardiac arrhythmias in obstructive sleep apnea (from the Akershus Sleep Apnea Project). The American Journal of Cardiology 108 (8), 1141–1146.

[81] Natali, D., 2015. Modeling the interaction of biomimetical slender structures with a fluid flow. Ph.D. thesis, Universitá Degli Studi di Genova.

[82] Newmark, N. M., 1959. A method of computation for structural dynamics. Journal of the Engineering Mechanics Division 85 (3), 67–94.

[83] Nishawala, V. V., 2011. A study of large deflection of beams and plates. Rutgers The State University of New Jersey-New Brunswick.

[84] Osborne, J., Osman, E., Hill, P., Lee, B., Sparkes, C., 1999. A new acoustic method of differentiating palatal from non-palatal snoring. Clinical Otolaryngology & Allied Sciences 24 (2), 130–133.

[85] Païdoussis, M. P., 1998. Fluid-structure interactions: Slender structures and axial flow. Vol. 1. Academic press, California.

[86] Papaioannou, G., Yue, D., Triantafyllou, M., Karniadakis, G., 2008. On the effect of spacing on the vortex-induced vibrations of two tandem cylinders. Journal of Fluids and Structures 24 (6), 833–854.

[87] Peskin, C. S., 1972. Flow patterns around heart valves: A numerical method. Journal of Computational Physics 10 (2), 252–271.

[88] Peskin, C. S., 1977. Numerical analysis of blood flow in the heart. Journal of Computational Physics 25 (3), 220–252.

[89] Peskin, C. S., 2002. The immersed boundary method. Acta Numerica 11, 479–517.

[90] Pevernagie, D. A., De Meyer, M. M., Claeys, S., 2005. Sleep, breathing and the nose. Sleep Medicine Reviews 9 (6), 437–451.

[91] Peyret, R., Viviand, H., Smolderen, J., 1975. Computation of viscous compressible flows based on the Navier-Stokes equations. NASA STI/Recon Technical Report N 76, 11380.

[92] Poinsot, T. J., Lele, S., 1992. Boundary conditions for direct simulations of compressible viscous flows. Journal of Computational Physics 101 (1), 104–129.

[93] Press, W. H., Teukolsky, S. A., Vetterling, W. T., Flannery, B. P., 2007. Numerical recipes third edition: The art of scientific computing. Cambridge University Press.

[94] Pulliam, T. H., Steger, J. L., 1980. Implicit finite-difference simulations of three-dimensional compressible flow. AIAA Journal 18 (2), 159–167.

[95] Quinn, S., Huang, L., Ellis, P., Williams, J. F., 1996. The differentiation of snoring mechanisms using sound analysis. Clinical Otolaryngology 21 (2), 119–123.

[96] Rappai, M., Collop, N., Kemp, S., et al., 2003. The nose and sleep-disordered breathing: What we know and what we do not know. Chest Journal 124 (6), 2309–2323.

[97] Rudy, D. H., Strikwerda, J. C., 1980. A nonreflecting outflow boundary condition for subsonic Navier-Stokes calculations. Journal of Computational Physics 36 (1), 55–70.

[98] Ryzhakov, P., Rossi, R., Idelsohn, S., Oñate, E., 2010. A monolithic Lagrangian approach for fluid–structure interaction problems. Computational Mechanics 46 (6), 883–899.

[99] Saiki, E., Biringen, S., 1996. Numerical simulation of a cylinder in uniform flow: Application of a virtual boundary method. Journal of Computational Physics 123 (2), 450–465.

[100] Schäfer, M., 2006. Computational engineering: Introduction to numerical methods. Springer, Berlin.

[101] Schneiders, L., Günther, C., Meinke, M., Schröder, W., 2016. An efficient conservative cut-cell method for rigid bodies interacting with viscous compressible flows. Journal of Computational Physics 311, 62–86.

[102] Schneiders, L., Hartmann, D., Meinke, M., Schröder, W., 2013. An accurate moving boundary formulation in cut-cell methods. Journal of Computational Physics 235, 786–809.

[103] Schwab, R. J., Goldberg, A. N., 1998. Upper airway assessment: Radiographic and other imaging techniques. Otolaryngologic Clinics of North America 31 (6), 931–968.

[104] Seo, J. H., Mittal, R., 2011. A high-order immersed boundary method for acoustic wave scattering and low-Mach number flow-induced sound in complex geometries. Journal of Computational Physics 230 (4), 1000–1019.

[105] Series, F., St Pierre, S., Carrier, G., 1992. Effects of surgical correction of nasal obstruction in the treatment of obstructive sleep apnea. The American Review of Respiratory Disease 146 (5 Pt 1), 1261–5.

[106] Sesterhenn, J., Müller, B., Thomann, H., 1999. On the cancellation problem in calculating compressible low Mach number flows. Journal of Computational Physics 151 (2), 597–615.

[107] Sieber, G., 2002. Numerical simulation of fluid-structure interaction using loose coupling methods. Ph.D. thesis, Technische Universität Darmstadt.

[108] Sokolnikoff, I. S., 1956. Mathematical theory of elasticity. McGraw-Hill book company, New York.

[109] Souli, M., Benson, D. J., 2013. Arbitrary Lagrangian Eulerian and fluid-structure interaction: Numerical simulation. John Wiley & Sons, New Jersey.

[110] Standring, S., 2015. Gray's Anatomy E-Book: The Anatomical Basis of Clinical Practice. Elsevier Health Sciences.

[111] Strand, B., 1994. Summation by parts for finite difference approximations for d/dx. Journal of Computational Physics 110 (1), 47–67.

[112] Su, W., Cesnik, C. E., 2014. Strain-Based Analysis for Geometrically Nonlinear Beams: A modal approach. Journal of Aircraft 51 (3), 890–903.

[113] Svärd, M., Nordström, J., 2014. Review of summation-by-parts schemes for initial-boundary-value problems. Journal of Computational Physics 268, 17–38.

[114] Szilard, R., 1974. Theory and analysis of plates: Classical and numerical methods. Prentice-Hall.

[115] Takács, G., Rohal'-Ilkiv, B., 2012. Model predictive vibration control: Efficient constrained MPC vibration control for lightly damped mechanical structures. Springer Science & Business Media, New York.

[116] Tang, L., Païdoussis, M. P., Jiang, J., 2009. Cantilevered flexible plates in axial flow: Energy transfer and the concept of flutter-mill. Journal of Sound and Vibration 326 (1), 263–276.

[117] Tetlow, G., Lucey, A. D., 2009. Motions of a cantilevered flexible plate in viscous channel flow driven by a constant pressure drop. Communications in Numerical Methods in Engineering 25 (5), 463–482.

[118] Tornberg, A.-K., Shelley, M. J., 2004. Simulating the dynamics and interactions of flexible fibers in Stokes flows. Journal of Computational Physics 196 (1), 8–40.

[119] Triantafyllou, M. S., Triantafyllou, G., Yue, D., 2000. Hydrodynamics of fishlike swimming. Annual Review of Fluid Mechanics 32 (1), 33–53.

[120] Tseng, Y.-H., Ferziger, J. H., 2003. A ghost-cell immersed boundary method for flow in complex geometry. Journal of Computational Physics 192 (2), 593–623.

[121] Turek, S., Hron, J., 2006. Proposal for numerical benchmarking of fluid-structure interaction between an elastic object and laminar incompressible flow. Lecture Notes in Computational Science and Engineering 53, 371.

[122] Udaykumar, H., Kan, H.-C., Shyy, W., Tran-Son-Tay, R., 1997. Multiphase dynamics in arbitrary geometries on fixed Cartesian grids. Journal of Computational Physics 137 (2), 366 – 405.

[123] Udaykumar, H., Mittal, R., Rampunggoon, P., Khanna, A., 2001. A sharp interface Cartesian grid method for simulating flows with complex moving boundaries. Journal of Computational Physics 174 (1), 345–380.

[124] Udaykumar, H., Mittal, R., Shyy, W., 1999. Computation of solid-liquid phase fronts in the sharp interface limit on fixed grids. Journal of Computational Physics 153 (2), 535 – 574.

[125] Udaykumar, H., Mittal, R., Shyy, W., 1999. Computation of solid-liquid phase fronts in the sharp interface limit on fixed grids. Journal of Computational Physics 153 (2), 535–574.

[126] Verzicco, R., Fatica, M., Iaccarino, G., Orlandi, P., 2004. Flow in an impeller-stirred tank using an immersed-boundary method. AIChE Journal 50 (6), 1109–1118.

[127] Vichnevetsky, R., Bowles, J. B., 1982. Fourier analysis of numerical approximations of hyperbolic equations. SIAM.

[128] Visbal, M. R., Gaitonde, D. V., 2002. On the use of higher-order finite-difference schemes on curvilinear and deforming meshes. Journal of Computational Physics 181 (1), 155–185.

[129] Wall, W. A., Rabczuk, T., 2008. Fluid–structure interaction in lower airways of CT-based lung geometries. International Journal for Numerical Methods in Fluids 57 (5), 653–675.

[130] Yang, J., Balaras, E., 2006. An embedded-boundary formulation for large-eddy simulation of turbulent flows interacting with moving boundaries. Journal of Computational Physics 215 (1), 12–40.

[131] Yang, X., Zhang, X., Li, Z., He, G.-W., 2009. A smoothing technique for discrete delta functions with application to immersed boundary method in moving boundary simulations. Journal of Computational Physics 228 (20), 7821–7836.

[132] Ye, T., Mittal, R., Udaykumar, H., Shyy, W., 1999. An accurate Cartesian grid method for viscous incompressible flows with complex immersed boundaries. Journal of Computational Physics 156 (2), 209–240.

[133] Young, T., Palta, M., Dempsey, J., Skatrud, J., Weber, S., Badr, S., 1993. The occurrence of sleep-disordered breathing among middle-aged adults. New England Journal of Medicine 328 (17), 1230–1235.

[134] Young, T., Skatrud, J., Peppard, P. E., 2004. Risk factors for obstructive sleep apnea in adults. JAMA 291 (16), 2013–2016.

[135] Zhou, Y., Zhao, S., Feig, M., Wei, G.-W., 2006. High order matched interface and boundary method for elliptic equations with discontinuous coefficients and singular sources. Journal of Computational Physics 213 (1), 1–30.

[136] Zhu, C., Luo, H., Li, G., 2016. High-order immersed-boundary method for incompressible flows. AIAA Journal 54 (9), 2734–2741.

[137] Zozula, R., Rosen, R., 2001. Compliance with continuous positive airway pressure therapy: Assessing and improving treatment outcomes. Current Opinion in Pulmonary Medicine 7 (6), 391–398.

Appended Papers

Paper I [53]

Interaction between a simplified soft palate and compressible viscous flow

M. Khalili, M. Larsson, B. Müller

Journal of Fluids and Structures 67 (2016), 85–105.

Interaction between a simplified soft palate and compressible viscous flow

M. Ehsan Khalili[a,*], Martin Larsson[b], Bernhard Müller[a]

[a] *Department of Energy and Process Engineering, Norwegian University of Science and Technology (NTNU), Kolbjørn Hejes vei 2, NO-7491 Trondheim, Norway*
[b] *SINTEF Materials and Chemistry, S. P. Andersens vei 15B, Trondheim, Norway*

Abstract

Fluid–structure interaction in a simplified 2D model of the upper airways is simulated to study flow–induced oscillation of the soft palate in the pharynx. The goal of our research has been a better understanding of the mechanisms of the Obstructive Sleep Apnea Syndrome and snoring by taking into account compressible viscous flow. The inspiratory airflow is described by the 2D compressible Navier–Stokes equations, and the soft palate is modeled as a flexible plate by the linearized Euler–Bernoulli thin beam theory. Fluid–structure interaction is handled by the arbitrary Lagrangian–Eulerian formulation. The fluid flow is computed by utilizing 4^{th} order accurate summation by parts difference operators and the 4^{th} order accurate classical Runge–Kutta method which lead to very accurate simulation results. The motion of the cantilevered plate is solved numerically by employing the Newmark time integration method. The numerical schemes for the structure are verified by comparing the computed frequencies of plate oscillation with the associated second mode eigenfrequency in vacuum. Vortex dynamics is assessed for the coupled fluid-structure system when both airways are open and when one airway is closed. The effect of mass ratio, rigidity and damping coefficient of the plate on the oscillatory behaviour is investigated. An acoustic analysis is carried out to characterize the acoustic wave propagation induced by the plate oscillation. It is observed that the acoustic wave corresponding to the quarter wave mode along the length of the duct is the dominant frequency. However, the frequency of the plate oscillation is recognizable in the acoustic pressure when reducing the amplitude of the quarter wave mode.

Keywords: Fluid-structure interaction (FSI); High order finite difference method; Cantilevered flexible plate; Acoustics; Obstructive sleep apnea syndrome (OSAS)

1. Introduction

Fluid structure interaction (FSI) refers to a phenomenon where a flow field interacts with compliant or elastic structures. The behaviour of many dynamic systems is influenced by the interaction between the fluid flow and structural components that are involved in the system. This interaction happens in a wide range of phenomena such as flapping of insect wings, the flutter of flags, the vibration of bridges and structures and the aeroelasticity of aircraft wings. With growing interest in the multidisciplinary field of biomedical and biomechanical engineering, a vast amount

*Corresponding author
Email address: mohammadtaghi.khalili@ntnu.no (Mohammadtaghi Khalili)

of research has been conducted to comprehend fluid-structure interaction in physiological systems in the human body (Tian et al., 2014; Wu and Cai, 2014; Larsson and Müller, 2012).

One of the prime examples of FSI in biomechanical systems is the dynamics of the upper airways where the interaction between inspiratory and expiratory airflow with soft tissues may lead to flow-induced instabilities. Disorders of the upper airways are often associated with respiratory syndromes. Among these, obstructive sleep apnea (OSA) and snoring are closely related to the flow conditions in the upper airways. Obstructive sleep apnea syndrome (OSAS) is one of the most prevalent types of sleep-disordered breathing caused by repetitive collapse of the soft tissues in the upper airways. Estimates show that OSAS affects 2–4% of the adult population (Young et al., 1993). The significant consequence of OSAS is sleep fragmentation which can lead to increased daytime sleepiness, fatigue-related accidents and risk of cardiovascular diseases (Malhotra and White, 2002). Even though snoring does not necessarily mean that one has sleep apnea, estimates show that 10% of snorers are at risk of OSAS (Bertram, 2008).

In recent years, the fluid flow over a cantilevered plate has been a reliable theoretical model not only for many engineering applications but also for many biomechanical systems like human palatal snoring (Kuhl and DesJardin, 2012; Huang and Zhang, 2013). Computational models have been increasingly employed to model upper airways. In most of the investigations, inviscid flow has been assumed to develop numerical models for flow-induced instabilities (Guo and Païdoussis, 2000; Howell et al., 2009; Shoele and Mittal, 2016). A cantilevered beam immersed in a channel flow has been investigated by Auregan and Depollier (1995) both analytically and experimentally to understand snoring. They employed linear small deflection beam theory and neglected frictional losses. Quasi-parallel flow was assumed and the pressure on the beam was estimated by mass conservation and the Bernoulli equation. Huang (1995) modeled a cantilevered elastic plate immersed in an axial flow, and also conducted wind tunnel experiments to verify theoretical results for palatal snoring. The governing equation for linear plate bending was solved by using finite expansion of orthogonal in vacuum modes. Although the viscous effect of circulation was implicitly imposed by the Kutta–Joukowski condition at the free trailing edge of the plate, viscosity was neglected and potential flow theory was used. He found that fluid loading resulting from the interaction of the wake vortices is responsible for the irreversible energy transfer in the flow–induced instability.

Linear instability of thin elastic plates with different leading and trailing edge conditions in 2D channel flow was investigated by Guo and Païdoussis (2000). Similar to the work done by Auregan and Depollier (1995), the 1D linear plate equation was solved by applying the Galerkin method where plate deflections were recast in the form of an expansion series of orthogonal beam functions. A Fourier transform technique was applied to solve the perturbation pressure from the potential flow equations. They found that single-mode and coupled-mode flutter are dominant modes for plates with a free trailing edge and free-free edge, respectively. However, the instability of plates with either clamped or pinned boundary condition at edges may occur through first-mode divergence exceeding other types of instability modes (Guo and Païdoussis, 2000).

Tang and Païdoussis (2007, 2008) performed computational investigations of non-linear large deflection of cantilever plates using the inextensibility condition surrounded by axial flow. The flow was assumed purely inviscid even if a separate viscous drag was coupled into the plate equation, and the imposed pressure difference on the plate was estimated using an unsteady lumped vortex model. Their analytical results show that if critical flutter velocity and frequency increase, the drag coefficient will increase. Furthermore, in experimental results they observed sudden flutter vibration at critical velocities. However, the onset of oscillation will be more unlikely, if the flow

velocity is reduced from an initial plate flutter. They demonstrated the possibility of a hysteresis phenomenon by including an unsteady von Kármán vortex street in their simulation. Conducting more theoretical investigations on the effect of trailing edge wakes on plate instability, they concluded that longer plates together with higher critical frequencies cause higher ratios of plate vibration velocity to wake-induced flow velocity, and thus a smaller effect of wake-induced flow velocities on the plate.

In contrast to the studies mentioned above, Balint and Lucey (2005) and Tetlow and Lucey (2009) included viscous effects directly in their instability analysis by solving the Navier–Stokes equation in a 2D channel surrounding a cantilever plate. Whereas Balint and Lucey (2005) modeled the motion of a thin plate using linear plate theory under differential pressure, Tetlow and Lucey (2009), added a tension term defined as the skin friction force acting on both the upper and lower sides of the plate. In both studies, the finite element method was employed in order to solve the unsteady, laminar Navier–Stokes equations in a channel geometry with inlet boundaries above and below the flexible plate and to estimate fluid loads interfacing with the plate. Their fluid solver was explicitly coupled to the structural finite difference solver. Based on their numerical results, when both upper and lower inlets are open, a flutter-type instability is initiated at a critical Reynolds number, while if one of the inlets is closed, a divergence-type instability occurs at a critical velocity. Although Tetlow and Lucey (2009) imposed a constant pressure drop along the channel rather than assuming velocity-driven flow, flutter instabilities similar to those found by Balint and Lucey (2005) were observed.

In this paper, we use a compressible viscous flow model to simulate the flow-induced oscillation of the soft palate in the pharynx by a simplified 2D model (cf. Fig.1). We couple the compressible flow in the pharynx to a cantilevered thin plate model of the soft palate in an arbitrary Lagrangian-Eulerian (ALE) formulation by using a two-way explicit coupling. A high order finite difference method based on summation by parts (SBP) (Strand, 1994; Svärd and Nordström, 2014) is used for the spatial discretization of the compressible Navier–Stokes equations. The classical fourth order explicit Runge–Kutta scheme is applied for time integration for the sake of accuracy and easy parallelization. The Newmark time integration method and central finite difference method are used to solve the linearized Euler–Bernoulli thin beam model. To achieve geometric flexibility with high order operators for this simplified model in the upper airways, the multi block structured grid approach is employed. We investigate the effect of material properties on the oscillation behaviour of the flexible plate. Using compressible fluid flow permits us to investigate the acoustic waves inside the channel and also the effect of flexible plate oscillation on sound generation.

The paper is organized as follows. In Section 2, the models for fluid flow, structure and their coupling by FSI are presented. In Section 3, first the verification of the structure scheme is performed. Next, the numerical simulation of the plate oscillation for flow with artificially increased Mach numbers up to 0.02 and Reynolds numbers up to 756 is presented. Then, the effects of plate properties on the plate oscillation induced by the flow are examined, and finally the results of the acoustic analysis are shown. Conclusions are stated in Section 4.

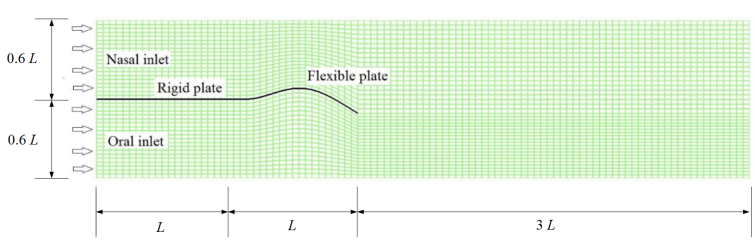

(a) Schematic of the computational model

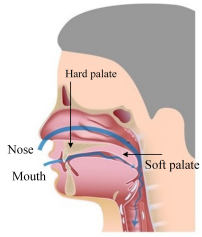

(b) The anatomy of upper airways.

Figure 1: Computational model and real geometry.

2. Model

2.1. Fluid flow

In the present study, the 2D compressible Navier–Stokes equations in perturbation form are solved. The perturbation formulation is employed to minimize cancellation errors when discretizing the Navier–Stokes equations for compressible low Mach number flow (Sesterhenn et al., 1999; Müller, 2008). The conservative form of the 2D compressible Navier–Stokes equations in perturbation formulation can be written as

$$\mathbf{U}'_t + \mathbf{F}^{c\prime}{}_x + \mathbf{G}^{c\prime}{}_y = \mathbf{F}^{v\prime}{}_x + \mathbf{G}^{v\prime}{}_y \tag{1}$$

where $\mathbf{U}' = \mathbf{U} - \mathbf{U_0}$ is the vector of conservative perturbation variables with $\mathbf{U} = (\rho, \rho u, \rho v, \rho E)^T$ the vector of the conservative variables and $\mathbf{U}_0 = (\rho_0, 0, 0, (\rho E)_0)^T$ the stagnation values.

The conservative perturbation variables $\mathbf{U}'$ and the inviscid ($\mathbf{F}^{c\prime}$, $\mathbf{G}^{c\prime}$) and viscous perturbation flux vectors ($\mathbf{F}^{v\prime}$, $\mathbf{G}^{v\prime}$) are defined by $\mathbf{F}^{c\prime} = \mathbf{F}^c(\mathbf{U}) - \mathbf{F}^c(\mathbf{U_0})$, etc.

$$\mathbf{U}' = \begin{pmatrix} \rho' \\ (\rho u)' \\ (\rho v)' \\ (\rho E)' \end{pmatrix},$$

$$\mathbf{F}^{c\prime} = \begin{pmatrix} (\rho u)' \\ (\rho u)'u' + p' \\ (\rho v)'u' \\ ((\rho H)_0 + (\rho H)')u' \end{pmatrix}, \quad \mathbf{G}^{c\prime} = \begin{pmatrix} (\rho v)' \\ (\rho u)'v' \\ (\rho v)'v' + p' \\ ((\rho H)_0 + (\rho H)')v' \end{pmatrix},$$

$$\mathbf{F}^{v\prime} = \begin{pmatrix} 0 \\ \tau'_{xx} \\ \tau'_{xy} \\ u'\tau'_{xx} + v'\tau'_{xy} + \kappa T'_x \end{pmatrix}, \quad \mathbf{G}^{v\prime} = \begin{pmatrix} 0 \\ \tau'_{yx} \\ \tau'_{yy} \\ u'\tau'_{yx} + v'\tau'_{yy} + \kappa T'_y \end{pmatrix},$$

where t is physical time and x and y are the Cartesian coordinates. ρ denotes density, u and v

the x- and y-direction velocity components, E the specific total energy, T the temperature and κ the heat conduction coefficient calculated from the constant Prandtl number $\mathrm{Pr} = 1$. ρ_0, $(\rho E)_0$ and $(\rho H)_0$ denote the stagnation values of density, total energy density and total enthalpy density, respectively. The perturbation variables are given as follows

$$\rho' = \rho - \rho_0, \quad (\rho\mathbf{u})' = (\rho\mathbf{u}), \quad (\rho E)' = \rho E - (\rho E)_0, \quad (\rho H)' = (\rho E)' + p'$$
$$\mathbf{u}' = \frac{(\rho\mathbf{u})'}{\rho_0+\rho'}, \quad \tau' = \mu(\nabla\mathbf{u}' + (\nabla\mathbf{u}')^T) - \frac{2}{3}\mu(\nabla\cdot\mathbf{u}')\mathbf{I}, \quad T' = \frac{p'/R - \rho' T_0}{\rho_0+\rho'}$$

Here, R is the specific gas constant and μ is the viscosity which is determined from the Sutherland law $\frac{\mu}{\mu_0} = (\frac{T}{T_0})^{1.5}[(1+S_c)/(\frac{T}{T_0}+S_c)]$ with non-dimensional Sutherland constant $S_c = \frac{110}{301.75}$.

Since perfect gas is considered, the pressure perturbation can be related to the conservative perturbation variables $p' = (\gamma-1)[(\rho E)' - \frac{1}{2}((\rho\mathbf{u}'\cdot\mathbf{u}'))]$, where the ratio of specific heats $\gamma = c_p/c_v = 1.4$ for air.

The viscous flux vectors $\mathbf{F}^{v\prime}$ and $\mathbf{G}^{v\prime}$ are the same as for the standard conservative form, except for using the temperature perturbation T' instead of temperature T for the heat flux terms. The momentum density and velocity perturbations are taken as the same as their unperturbed counterparts, i.e. $(\rho\mathbf{u})' = \rho\mathbf{u}$ (Larsson and Müller, 2009). For convenience the variables are non-dimensionalized with ρ_0, stagnation speed of sound c_0, L the length of the flexible plate and $\rho_0 c_0^2$ as reference values. In order to generalize the geometry for the human upper airways, the equations of motions are transformed from the physical domain (x, y) to the computational domain (ξ, η) by the following relations, and obviously for time-dependent geometry the transformation depends on time as well.

$$\begin{aligned} t &= \tau \\ x &= x(\xi,\eta,\tau) \\ y &= y(\xi,\eta,\tau). \end{aligned} \tag{2}$$

Thus, the transformed 2D compressible Navier–Stokes equations in perturbation form are expressed as

$$\hat{\mathbf{U}}'_\tau + \hat{\mathbf{F}}'_\xi + \hat{\mathbf{G}}'_\eta = 0, \tag{3}$$

where $\hat{\mathbf{U}}' = J^{-1}\mathbf{U}'$, $\hat{\mathbf{F}}' = J^{-1}(\xi_\tau\mathbf{U}' + \xi_x(\mathbf{F}^{c\prime} - \mathbf{F}^{v\prime}) + \xi_y(\mathbf{G}^{c\prime} - \mathbf{G}^{v\prime}))$ and $\hat{\mathbf{G}}' = J^{-1}(\eta_\tau\mathbf{U}' + \eta_x(\mathbf{F}^{c\prime} - \mathbf{F}^{v\prime}) + \eta_y(\mathbf{G}^{c\prime} - \mathbf{G}^{v\prime}))$. The chain rule for partial differentiation provides the expressions for Cartesian derivatives in the viscous flux vectors $\mathbf{F}^{v\prime}$ and $\mathbf{G}^{v\prime}$, e.g. $u'_x = u'_\xi\xi_x + u'_\eta\eta_x$ and $u'_y = u'_\xi\xi_y + u'_\eta\eta_y$. The Jacobian determinant of the transformation is $J^{-1} = x_\xi y_\eta - x_\eta y_\xi$ and time-dependent metric terms are

$$\begin{aligned} J^{-1}\xi_x &= y_\eta, \quad J^{-1}\xi_y = -x_\eta, \quad J^{-1}\xi_\tau = -x_\tau\xi_x + y_\tau\xi_y, \\ J^{-1}\eta_x &= -y_\xi, \quad J^{-1}\eta_y = x_\xi, \quad J^{-1}\eta_\tau = -y_\tau x_\xi + x_\tau y_\xi. \end{aligned} \tag{4}$$

2.1.1. Numerical schemes

The high order finite difference method based on SBP operators (Strand, 1994; Gustafsson, 2008; Gustafsson et al., 1995) is employed for space discretization of the compressible Navier–Stokes equations. We use a globally fourth order SBP operator to discretize the first ξ- and η-derivatives in (4) and (3) and apply them twice to approximate the viscous parts of $\hat{\mathbf{F}}_\xi{}'$ and $\hat{\mathbf{G}}_\eta{}'$. The SBP operators for $\frac{\partial}{\partial\xi}$ and $\frac{\partial}{\partial\eta}$ correspond to the sixth order central difference operator in the interior but degrade to third order accuracy near the boundary, resulting in fourth order global accuracy (Gustafsson, 2008). This approach is based on the energy method, which permits us to derive well-posedness for the continuous problem and to guarantee stability for the discrete problem. The summation by parts operators and the stability criteria are discussed in detail in the Appendix.

For the time integration process, the classical fourth order explicit Runge–Kutta method is used. A time step size $\triangle t$ corresponding to CFL = 0.333 is chosen to ensure stability.

The multi-block structured grid approach is employed to represent the simplified geometry in the upper airways. Fig. 2(a) shows that we employ 6 blocks. Blocks 1, 3 and 5 have the lower channel wall as their southern boundaries and the rigid plate, flexible plate and the line between the trailing edge of the flexible plate and the outlet, respectively, as their northern boundaries, cf. lower plot in Fig. 2(a). The upper neighbouring blocks 2, 4 and 6 with the upper channel wall as their northern boundaries are set apart in the upper plot of Fig. 2(a) to show the overlapping regions. The decomposition of the computational domain into blocks allows us to accommodate geometric flexibility with high order operators. Having an overlap region of grid points at the block interfaces, a smooth transition of the numerical solution from one block to another block is achieved. For the seven-point stencil of the standard sixth order central finite difference method, a three-point overlap at each side of inter-block boundaries is added cf. Fig.2(b). The black points are located on the non–overlapping block boundary. The three red points in the interior of the left block communicate their data to the overlapping white points of the right block. Likewise, the three green points in the interior of the right block communicate their data to the overlapping white points of the left block. The inter-block communication between neighbouring blocks is accomplished by using the Message Passing Interface (MPI) such that each block is assigned to a single process, enabling parallel solution of the flow field.

This fluid solver has been validated in previous investigations (Müller, 2008; Larsson and Müller, 2012) for single-domain structured grids.

2.1.2. Boundary conditions

Adiabatic no-slip boundary conditions are applied on the walls and the fluid-structure interface. At the inflow, the velocities in the x- and y-directions are imposed using a uniform inlet profile normal to the boundary, $u(x = 0, t) = U_0$ and $v = 0$. In addition, the inlet temperature is set to $T = T_0 = 310$ K. The outlet pressure is set to atmospheric pressure, i.e., $p' = p - p_0 = p - p_{\text{atm}} = 0$ Pa. Non-reflecting characteristic boundary conditions are employed at the inflow and outflow boundaries to minimize wave reflections. The Navier–Stokes characteristic boundary conditions (NSCBC) developed by Poinsot and Lele (1992) are employed to approximate incoming waves based on local one-dimensional inviscid (LODI) relations. The primitive variables can be related to the wave amplitude ($\mathscr{L}_i$) by LODI relations. The amplitudes of the characteristic waves are $\mathscr{L}_1 = \lambda_1(\frac{\partial p}{\partial x} - \rho c\frac{\partial u}{\partial x})$, $\mathscr{L}_2 = \lambda_2(c^2\frac{\partial \rho}{\partial x} - \frac{\partial p}{\partial x})$, $\mathscr{L}_3 = \lambda_3(\frac{\partial v}{\partial x})$ and $\mathscr{L}_4 = \lambda_4(\frac{\partial p}{\partial x} + \rho c\frac{\partial u}{\partial x})$. Since fully non-reflecting conditions may lead to an ill-posed problem (Poinsot and Lele, 1992), this approach is partially reflecting. Imposing a constant pressure at the outlet requires $\mathscr{L}_1 = -\mathscr{L}_4$. To keep the reflections low and pressure close to atmospheric pressure, the incoming wave amplitude is set to

$$\mathscr{L}_1 = K(p - p_{atm}), \tag{5}$$

where K is the relaxation coefficient. Rudy and Strikwerda proposed the relaxation coefficient as $K = \sigma(1 - \text{Ma}^2)(c/L_t)$ where Ma is the Mach number, c the sound speed, L_t the total length of the domain and σ a constant value (Rudy and Strikwerda, 1980). The optimum value $\sigma = 0.25$ derived by Rudy and Strikwerda (1980) is employed. For reverse flow (negative velocity in x-direction) at the outlet, $\mathscr{L}_1$, $\mathscr{L}_2$ and $\mathscr{L}_3$ are set to zero.

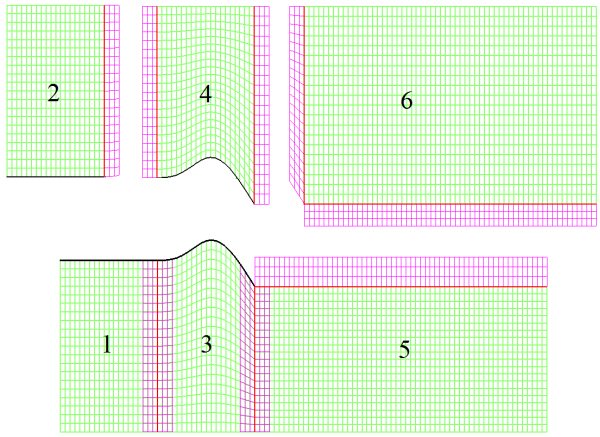

(a) Block-structure topology of the computational domain. The three upper blocks are detached in the figure for illustration of the three-point overlap, shown with magenta lines.

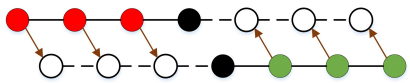

(b) Illustration of points overlapping along a line. The black points lie on the block boundary, the red and green points are internal points in different blocks, the white points are added ghost points which overlap the internal points in the other block, and the arrows indicate the direction of data transfer between blocks.

Figure 2: Multiblock topology used for the simplified geometry of the upper airways.

2.2. The structure model

In the present study, the motion of the thin plate is based on the linear Euler–Bernoulli thin beam theory. This theory provides the correlation between the deflection of the beam and the applied load. In the Euler–Bernoulli thin beam theory, the deflection is assumed to be unidirectional in the normal direction of the thin beam. Thus, deflection occurs only as a result of bending; the shear-deformation and normal strains are neglected. There is no contribution from the fluid shear stress, i.e., viscous effects on the plate are ignored and only the difference in fluid pressure is accounted for. The oscillation of the flexible plate is constrained to vertical direction without any stretch along the horizontal direction. The governing equation for the vertical displacement $\phi(x,t)$ is expressed as

$$\rho_s h \frac{\partial^2 \phi}{\partial t^2} + d\frac{\partial \phi}{\partial t} + B\frac{\partial^4 \phi}{\partial x^4} = -\delta p, \tag{6}$$

where ρ_s, h, d and B denote respectively the density, thickness, flexural rigidity and structural damping of the plate, and δp denotes the applied pressure load. The flexural rigidity B is defined by $B = Eh^3/[12(1-\nu^2)]$, where E and ν are the elastic modulus and Poisson ratio, respectively. The

variables in Eq. (6) are non-dimensionalized with respect to the stagnation density ρ_0, stagnation speed of sound c_0 and the length of the flexible plate L, in the same way as for the fluid solver.

The equation for calculating the energy of the plate per unit width can be derived by multiplying Eq. (6) by $\dot{\phi} = \frac{\partial \phi}{\partial t}$ and integrating over the length of the plate L (Balint and Lucey, 2005).

$$\frac{d}{dt}\left(\overbrace{\underbrace{\frac{1}{2}\rho_s h \int_0^L \dot{\phi}^2 dx}_{E_k} + \underbrace{\frac{1}{2}B\int_0^L (\phi_{xx})^2 dx}_{E_s}}^{E_t}\right) = \underbrace{\int_0^L (-\delta p)\dot{\phi} dx}_{\dot{W}} - \underbrace{d\int_0^L \dot{\phi}^2 dx}_{\dot{D}_\phi}. \tag{7}$$

The left hand side of the Eq. (7) is the time derivative of the total energy of the plate E_t composed of the kinetic and strain energies, E_k and E_s, respectively. The right hand side represents the rate of work done by the fluid on the plate $\dot{W}$ and the rate of energy dissipation due to damping of the plate $\dot{D}_\phi$.

2.2.1. Computational methods

The Newmark time integration method (Newmark, 1959) is employed for solving Eq.(6) implicitly. The displacement and velocity from time step t are integrated to $t + \triangle t$ using the relations

$$\dot{\phi}^{n+1} = \dot{\phi}^n + [(1-\gamma)\ \ddot{\phi}^n + \gamma\ddot{\phi}^{n+1}]\triangle t, \tag{8}$$

$$\phi^{n+1} = \phi^n + \dot{\phi}^n \triangle t + [(\frac{1}{2} - \beta)\ddot{\phi}^n + \beta\ddot{\phi}^{n+1}]\triangle t^2, \tag{9}$$

where γ and β are parameters of the Newmark scheme and $\ddot{\phi}^{n+1}$ is the acceleration at the new time level.

The most accurate, unconditionally stable scheme of the Newmark family is used. Its coefficients are $\beta = 1/4$ and $\gamma = 1/2$. The scheme is second order accurate and preserves the energy for the linear system (Hughes, 2012). The standard second order central difference discretization is used for the fourth order spatial derivative $(\phi_{xxxx})_j^{n+1} \approx \frac{1}{\triangle x^4}(\phi_{j+2}^{n+1} - 4\phi_{j+1}^{n+1} + 6\phi_j^{n+1} - 4\phi_{j-1}^{n+1} + \phi_{j-2}^{n+1})$. The integration scheme works by first computing the updated displacement and applying it to obtain the structure acceleration at the new time level, and then finding the updated velocity of the structure.

2.2.2. Boundary conditions

The cantilevered flexible plate is clamped at the leading edge and free at the trailing edge. For a clamped configuration the first two nodes are stationary. The continuous and discrete boundary conditions read

$$\begin{array}{ll} \phi(0,t) = 0, & \phi_1 = 0, \\ \frac{\partial \phi(0,t)}{\partial x} = 0, & \phi_1 = \phi_2. \end{array} \tag{10}$$

For a free end configuration it is assumed that the bending moment and shear force are zero at the last node. Thus, we have

$$\begin{array}{ll} \frac{\partial^2 \phi(L,t)}{\partial x^2} = 0, & \phi_{N-1} = 2\phi_{N-2} - \phi_{N-3}, \\ \frac{\partial^3 \phi(L,t)}{\partial x^3} = 0, & \phi_N = 3\phi_{N-2} - 2\phi_{N-3}. \end{array} \tag{11}$$

2.3. Fluid-structure interaction

The Arbitrary Lagrangian–Eulerian (ALE) formulation is employed to handle the fluid flow in Eulerian description using moving fluid grids and the plate structure in a Lagrangian formulation using stationary structure grids. In the time-dependent coordinate transformation of the fluid flow domain, the grid point velocities $\dot{x}$ and $\dot{y}$ are subtracted from the fluid velocity to define the contravariant velocity components $U = \xi_x(u - \dot{x}) + \xi_y(v - \dot{y})$ and $V = \eta_x(u - \dot{x}) + \eta_y(v - \dot{y})$ which yield simple expressions for the transformed inviscid flux vectors $\hat{\mathbf{F}}^c$ and $\hat{\mathbf{G}}^c$ (Pulliam and Steger, 1980). The mesh update is implemented by remeshing the whole fluid domain in each time step using the positions and velocities of the flexible structure at the boundary and a linear interpolation for interior points in the fluid domain.

Solving fluid flow on a moving mesh, the numerical scheme should satisfy the Geometric Conservation Law (GCL) for mathematical consistency (Visbal and Gaitonde, 2002). This law states that

$$(J^{-1})_\tau + (J^{-1}\xi_t)_\xi + (J^{-1}\eta_t)_\eta = 0, \tag{12}$$

where the time derivatives of the computational coordinates ξ and η are calculated from grid point velocities $\dot{x} = x_\tau,\ \dot{y} = y_\tau$ as follows

$$\xi_t = -\xi_x\dot{x} - \xi_y\dot{y}, \quad \eta_t = -\eta_x\dot{x} - \eta_y\dot{y}. \tag{13}$$

Then, the 2D Navier–Stokes equations in ALE formulation (Peyret et al., 1975) are given by

$$\mathbf{U}'_\tau = \tfrac{1}{J^{-1}}(-\hat{\mathbf{F}}'_\xi - \hat{\mathbf{G}}'_\eta - (J^{-1})_\tau\mathbf{U}'), \tag{14}$$

where $\hat{\mathbf{F}}' = J^{-1}(\xi_t\mathbf{U}' + \xi_x\mathbf{F}' + \xi_y\mathbf{G}')$ and $\hat{\mathbf{G}}' = J^{-1}(\eta_t\mathbf{U}' + \eta_x\mathbf{F}' + \eta_y\mathbf{G}')$ are the transformed flux vectors.

The coupling between the fluid and the structure is handled by an explicit, two-way method where forces and deformations are exchanged between the flow and the deformable structure in each time-step, as shown in Figure 3. The fluid and structure interact with each other by applying equal vertical displacement and velocity at the interface, satisfying the no-slip and adiabatic wall boundary conditions.

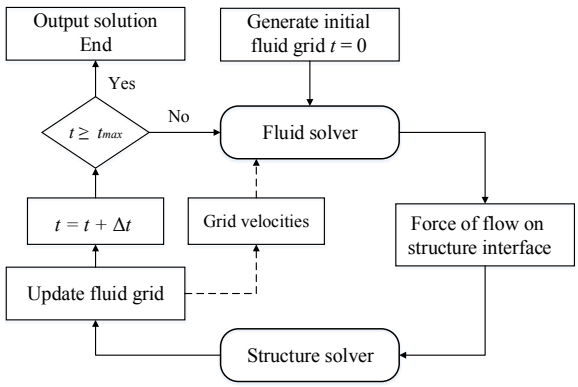

Figure 3: Schematic of two way coupling model.

3. Results and discussion

3.1. Verification of structure solver in vacuum

3.1.1. Eigenmode analysis

The numerical schemes for the structural model have been verified through the plate oscillation in vacuum associated with its eigenmodes. Following the work by Balint and Lucey (2005), d and δp in Eq. (6) are set to zero. Assuming a harmonic vibration of time dependency $e^{i\omega t}$, Eq. (6) can be rewritten based on the harmonic vibration. Thus, for vibration in vacuum, the cantilevered plate has the eigenfunctions

$$\begin{aligned}&\phi_m(x) = A\,[(\cosh(k_m x) - \cos(k_m x)) - \tfrac{\cosh(k_m L)+\cos(k_m L)}{\sinh(k_m L)+\sin(k_m L)}\,(\sinh(k_m x) - \sin(k_m x))],\\ &m = 1, 2, 3, \ldots \infty\end{aligned} \tag{15}$$

where A denotes the amplitude scaling constant and $k_m = \beta_m/L$ the characteristic wavenumber obtained by finding the roots of an eigenvalue equation. The coefficients β_m are obtained from

$$\cosh\beta_m \cos\beta_m + 1 = 0. \tag{16}$$

The five first values of β_m, $m = 1, ..., 5$, are $1.875, 4.694, 7.855, 10.996, 14.137$. The angular eigenfrequencies can be calculated as

$$\omega_m = k_m^2\sqrt{B/(\rho_s h)}. \tag{17}$$

The modal configurations of the cantilevered plate are shown in Figure 4.

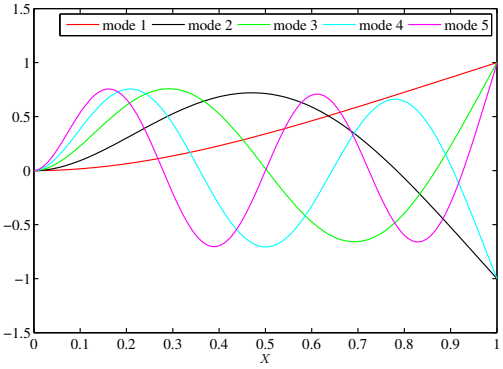

Figure 4: The first five eigenfunctions $\phi_m(x)$ with $A = 1$ in Eq.(15).

3.1.2. Comparison with analytical solution

Our numerical schemes have been first verified and tested by simulating plate oscillation in vacuum associated with the second eigenmode of the structure. The physical properties of the flexible structure were taken the same as in the study by Balint and Lucey (2005), namely $m = 2.6$ kg/m^2, $B = 4.92$ kN m and the length of the flexible structure $L = 2$ m. The number of grid points for discretizing the plate was set to $N = 201$ and the time step size was set to $\Delta t = 5 \times 10^{-6}$ s. The plate was initially deformed using the amplitude $A = 0.01$ m in Eq. (15). Figure 5 illustrates

the time variation of the plate deformation, the displacement of the tip position and the oscillating frequency. The frequency is calculated by performing a fast Fourier transform (FFT) on the time history of the tip displacement of the plate. The error between the analytical solution of the second mode eigenfrequency $\omega_2 = 38.1366$ Hz in Eq. (17) and the computed frequency $\omega_2 = 38.0906$ Hz amounts to 0.12 %.

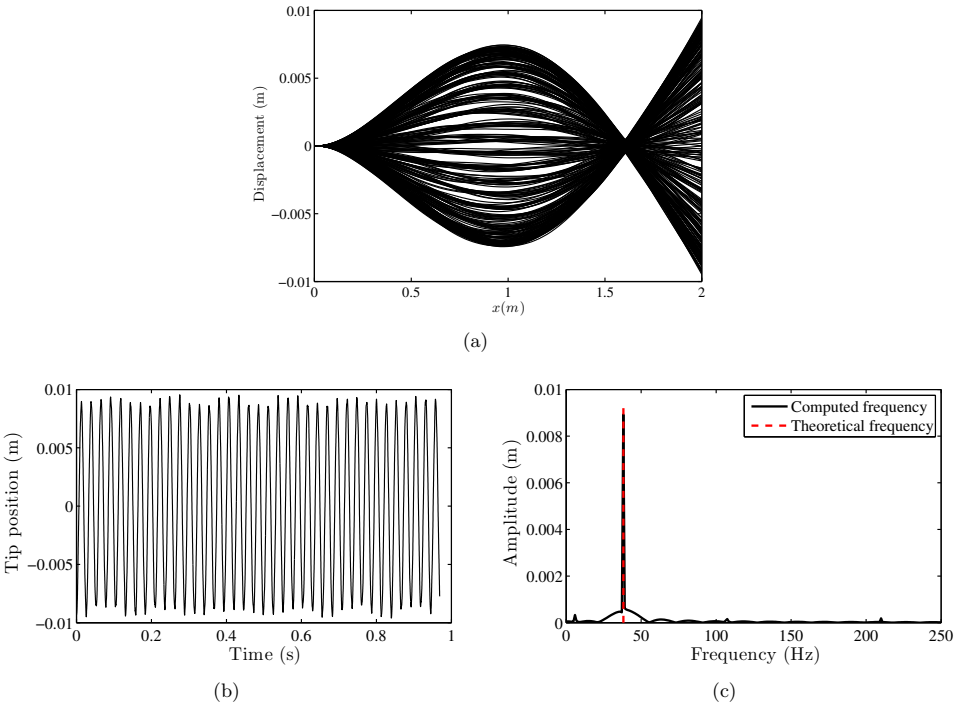

Figure 5: (a) Sequence of flexible plate deformation in the second eigenmode, (b) time history of the displacement of the trailing edge (tip), (c) oscillation frequency of displacement of trailing edge (tip).

3.2. Problem description and initial conditions for fluid–structure interaction

The problem domain consists of a horizontal channel with an interior wall representing the hard and soft palate along the center-line (cf. Fig. 1), dividing the inlet boundary into an upper and a lower inlet. We allow the inlet boundary to operate in two different configurations: one where both inlets have uniform inflow of air, and one where only the upper inlet has inflow while keeping the lower inlet at zero velocity. The flexible plate has length $L = 8$ mm, and the streamwise length and duct height (H) are 40 mm and 9.6 mm, respectively, cf. Fig.1(a).

The flexible plate is initially displaced using an eigenfunction. To initialize the flow field, we keep the flexible plate fixed in its initial position and integrate the flow solver in time from stagnant flow $\mathbf{U}' = 0$, except for the inlet velocity, until an approximately steady state flow solution has been reached. Thereafter, the flexible plate is released from its initial position and allowed to interact

with the flow.

As mentioned above, for a linear cantilevered plate with length L and flexural rigidity B, the vertical displacement $\phi_m(x)$ of the m^{th} eigenmode can be described by Eq. (15). In the present study, only the second eigenmode is considered for the initial plate displacement, mainly due to the fact that this mode has been known to be responsible for the soft palate flutter (Huang, 1995).

3.3. Verification of fluid–structure interaction

To assess the validity of the present solver, grid independence was investigated by computing the oscillation frequency of the flexible plate on coarse and fine grids. The fluid density was set to $\rho = 1.18$ kg/m^3 based on $T = 301.75$ K. We used the Reynolds number $\text{Re} = \frac{\rho UL}{\mu} = 378$ and the Mach number $\text{Ma} = \frac{U}{c_0} = 0.01$ based on inlet velocity ($U = 0.32$ m/s), speed of sound and length of the plate. The speed of sound was deliberately reduced to speed up the computation. The dynamic viscosity and other fluid properties were calculated as discussed in section 2.1. The initial tip amplitude was given by $\phi(L,0)/H = 0.2$. The elastic modulus and Poisson ratio were $E = 880$ MPa and $\nu = 0.3333$, respectively, with a plate density of $\rho_s = 2477$ kg/m^3, plate thickness of $h = 10^{-5}$ m and an undamped thin plate, i.e., $d = 0$ N s/m^3. Therefore, the plate is modeled as an infinitely thin 1D plate with the thickness parameter h chosen to obtain the desired second mode eigenfrequency. Using these values, the analytical second mode frequency in vacuum determined by Eq. (17) is 100 Hz. Numerically, the second in vacuum eigenfrequency is computed with $N = 101$ grid points and $\Delta t c_0/L = 0.001$ as 99.18 Hz which agrees well with the analytical value with a 0.82% error.

Fig. 6 shows the time history of the tip displacement from coarse to fine grids. Since the solution on the last two fine grids agree quite well, the 501×201 grid is adopted as a sufficiently fine grid. The oscillation frequency and the time variation of the plate deformation for the fine grid are shown in Fig. 7. The oscillation frequency of the flexible plate for the fine grid is obtained at 91.5 Hz (corresponding to the non-dimensional frequencies, $f^*_{c_0} = f\frac{L}{c_0} = 0.022875$ based on speed of sound c_0 and $f^*_U = f\frac{L}{U} = 2.2875$ based on inlet velocity U). Note that the in vacuum second mode frequency for the undamped flexible plate has been obtained by setting the external force (pressure difference) to zero in Eq. (6). However, in the simulation of fluid–structure interaction the pressure difference provides the external force which drives the plate oscillation. According to the measurements performed by Brietzke and Mair (2006), the palatal oscillation frequency of snoring ranges from 21 to 323 Hz with an average of 89.4 Hz.

In the following, the temporal discretization error of the fluid–structure interaction is investigated for the tip displacement of the plate. The parameters are identical to those used for the 501×201 fine grid in section 3.3 while varying the time step sizes. The tip displacement of the flexible plate is plotted versus time for five cycles of oscillation in Fig. 8. The time step sizes Δt are varied such that the CFL numbers become CFL $\approx 1/3$, $1/6$, $1/12$ and $1/24$. Fig. 8 shows that the time history of the tip displacment is hardly affected by the time step size.

3.4. Simulation of plate oscillation

3.4.1. Both inlets open

The time sequence of vorticity contours for the case when both inlets are open is shown in Fig. 9. The initial tip displacement is $\phi(L,0)/H = 0.2$, $\text{Re} = 378$ and $\text{Ma} = 0.01$. At time $tc_0/L = 0$ (when the flexible plate is released from its initial displacement after steady state has been reached), boundary layers have been established at the channel walls, rigid and flexible structures and the

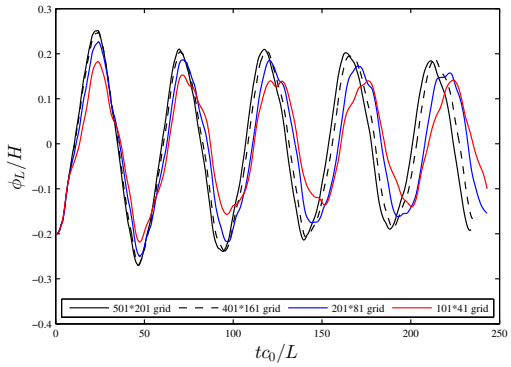

Figure 6: Test of grid independence, time history of tip displacement.

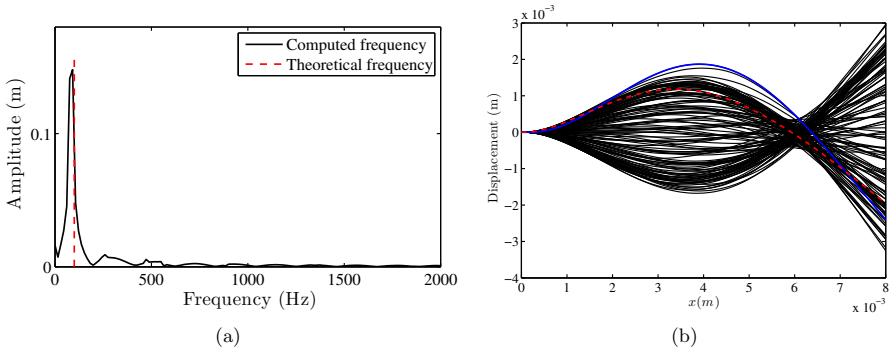

Figure 7: (a) Oscillation frequency of displacement of trailing edge (tip) for the fine grid, (b) sequence of flexible plate deformation for five cycle oscillations, the initial and final deformation are marked by solid blue line and red dashed lines, respectively.

flow is already separated from the trailing edge. At $tc_0/L = 8$ corresponding to $tU/L = 0.08$, the third vortex leaving the trailing edge is observed. The first and second vortices are about to pair and create a strong vortex at $tc_0/L = 13$. The fourth vortex is about to separate from the tip of the plate at $tc_0/L = 25$. The leading vortex rolls up at $tc_0/L = 39$. The vortex shedding from the trailing edge repeats itself almost symmetrically. The vortices formed as a result of the oscillation of the flexible plate and the interaction with the fluid flow are convected downstream. During the processes, the interaction between the vortices sometimes leads to vortex pairing.

To ensure that the outlet boundary conditions in this channel do not affect the vortices, this simulation is repeated for a longer channel. Fig. 10 shows the results. The only difference between Fig. 10 and Fig. 9 is that the length of the outlet blocks (from trailing edge of the plate towards outlet boundary in Fig. 1) and the number of grid points in these blocks have been doubled ($6L$

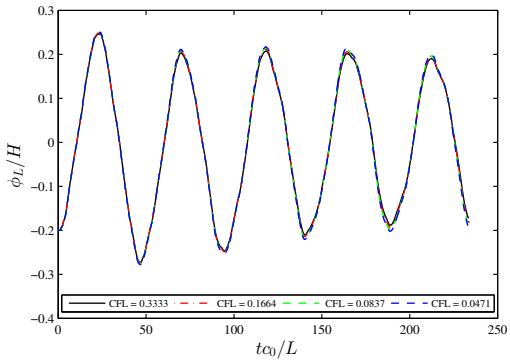

Figure 8: Test of time step independence, time history of tip displacement for five cycles of oscillation.

instead of $3L$ in Fig.1). The first and second snapshots show the status of the vortices at the same time for these two different channels. Except for the vortex close to the outlet being a little smaller and a little closer to centerline in the simulation with the longer channel at the considered time instant, the results for the two different channel lengths are in excellent agreement.

3.4.2. Lower inlet closed

Fig. 11 represents the results of vorticity contours when the lower inlet is closed. The initial tip amplitude is $\phi(L,0)/H = 0.1$, Reynolds number and Mach number based on inlet velocity U=0.64 m/s are equal to 756 and 0.02, respectively. The leading vortices are already shed before the structure was released. At $tc_0/L = 9$, the leading vortex rolls up. The vortices near the trailing edge roll down at $tc_0/L = 27$. At $tc_0/L = 48$, the leading vortex is becoming weakened and pairing of the vortices near the trailing edge is observed. The vortex shedding tends to propagate towards the lower part of the domain, since the lower inlet is closed. Clearly, the vortex shedding is unsymmetrical. Vortex pairing occurring quite often creates a complex vortical structure.

3.5. The effect of plate properties

Since one of the surgical treatments of OSAS and snoring involves soft palate implants, the flow induced oscillation of the flexible plate with different material parameters is studied in this section. The structural model is governed by three parameters: mass, damping and stiffness. We used these parameters as control parameters to investigate the oscillation behaviour of the flexible structure in the fluid flow. The non-dimensional mass, rigidity and damping are defined as

$$m^* = \frac{\rho_s h}{L\rho_0}, \quad B^* = \frac{B}{L^3\rho_0 c_0^2}, \quad d^* = \frac{d}{\rho_0 c_0}. \tag{18}$$

Dividing these non–dimensional rigidity and damping of the plate by Ma^2 and Ma, respectively, gives us the non–dimensional quantities for B and d in incompressible flow using U^2 instead of c_0^2 and U instead of c_0, respectively. In order to examine the oscillation behaviour of the flexible structure, the Reynolds number and Mach number are fixed at 378 and 0.01, respectively. Figures

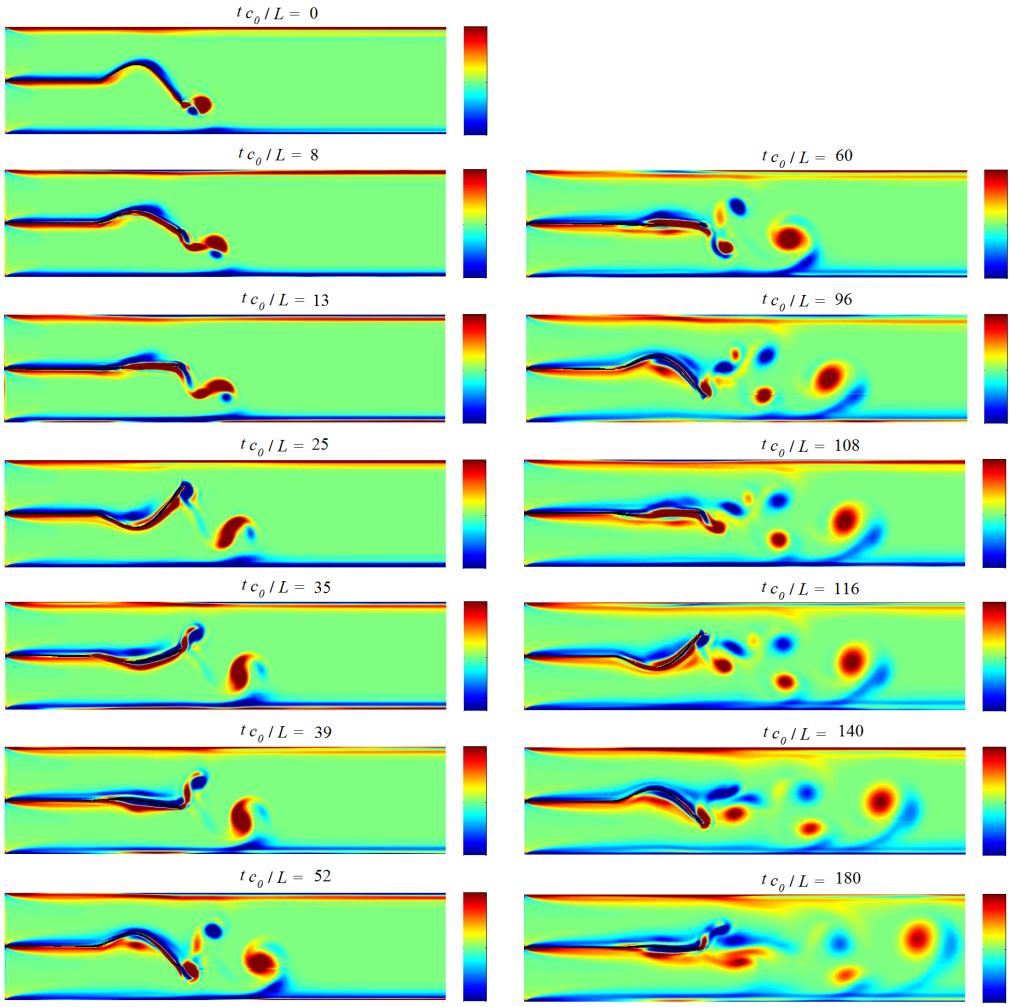

Figure 9: Time sequence showing vorticity contour plots, both inlets are open at Re = 378 and Ma = 0.01. The contour levels are from $-0.2\ \mathrm{s}^{-1}$ to $0.2\ \mathrm{s}^{-1}$ corresponding to $-5\times10^{-5} \leqslant (\bigtriangledown \times \mathbf{U})_z L/c_0 \leqslant 5\times10^{-5}$ and $-5\times10^{-3} \leqslant (\bigtriangledown \times \mathbf{U})_z L/U \leqslant 5\times10^{-3}$.

290 12, 14 and 16 illustrate the effect of changing the parameters on the displacement of the trailing edge.

The range of values of the non-dimensional mass is $m^* = 1.31 - 5.24$, as shown in Fig 12. The largest mass ratio decreases the oscillation frequency of the flexible plate to 61.06 Hz (non–dimensional frequency based on speed of sound $f^*_{c0} = f\frac{L}{c_0} = 0.015265$ and based on inlet velocity

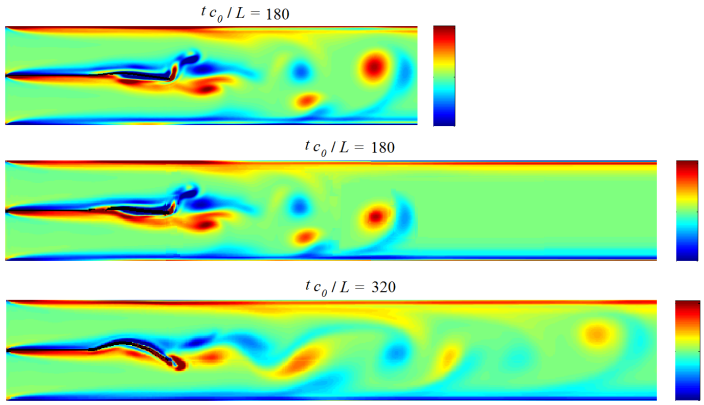

Figure 10: Time sequence showing vorticity contour plots, both inlets are open at Re = 378 and Ma = 0.01. The outlet blocks of two lower plots have a length of $6L$ instead of $3L$, cf. in Fig. 1, of the upper plot. The contour levels are from -0.2 s^{-1} to 0.2 s^{-1} corresponding to $-5 \times 10^{-5} \leqslant (\bigtriangledown \times \mathbf{U})_z L/c_0 \leqslant 5 \times 10^{-5}$ and $-5 \times 10^{-3} \leqslant (\bigtriangledown \times \mathbf{U})_z L/U \leqslant 5 \times 10^{-3}$.

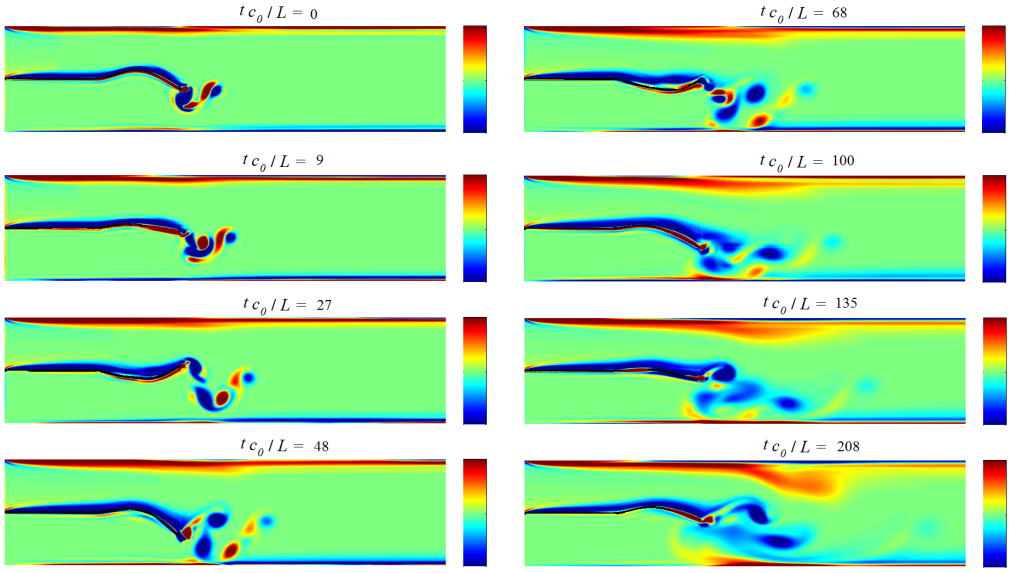

Figure 11: Time sequence showing vorticity contour plots, lower inlet is closed at Re = 756 and Ma = 0.02. The contour levels are from -0.2 s^{-1} to 0.2 s^{-1} corresponding to $-5 \times 10^{-5} \leqslant (\bigtriangledown \times \mathbf{U})_z L/c_0 \leqslant 5 \times 10^{-5}$ and $-5 \times 10^{-3} \leqslant (\bigtriangledown \times \mathbf{U})_z L/U \leqslant 5 \times 10^{-3}$.

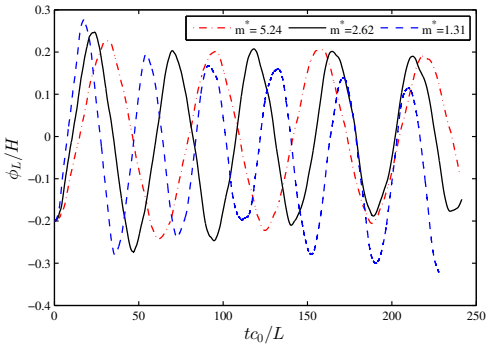

Figure 12: Time history of the tip displacement with different non-dimensional masses for undamped flexible plate (d^*=0) and fixed rigidity ($B^* = 1.3 \times 10^{-4}$).

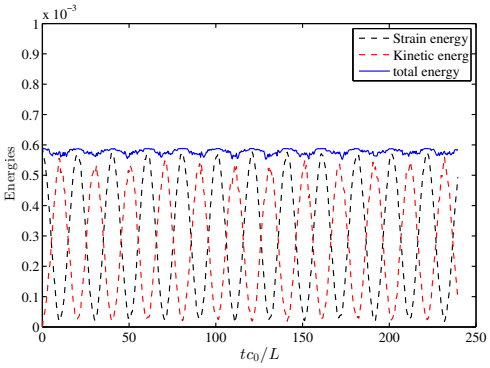

Figure 13: Evaluation of total energy E_t^*, strain energy E_s^* and kinetic energy E_k^* of the plate in vacuum for $m^* = 2.62$, $B^* = 1.3 \times 10^{-4}$ and $d^* = 0$.

$f_U^* = f\frac{L}{U} = 1.5265$) compared to the smallest one which enhances the oscillation frequency to 106.8 Hz ($f_{c_0}^* = 0.0267$ and $f_U^* = 267$). Figure 13 shows the total energy E_t^*, strain energy E_s^* and kinetic energy E_k^* of the plate in vacuum when the plate properties are $m^* = 2.62$, $B^* = 1.3 \times 10^{-4}$ and $d^* = 0$. It indicates that in the in vacuum situation the total energy of the plate remains nearly constant. Figure 14 gives the oscillation behaviour of the trailing edge as a representative of the flexible plate motion for three different non-dimensional rigidities. It is observed that for the higher rigidity case ($B^* = 2.6 \times 10^{-4}$) in the absence of damping, the oscillation frequency is higher, i.e. $f = 122$ Hz ($f_{c_0}^* = 0.0305$ and $f_U^* = 3.05$) than for $B^* = 1.3 \times 10^{-4}$ and $B^* = 6.6 \times 10^{-5}$ when $f = 91.5$ Hz ($f_{c_0}^* = 0.022875$ and $f_U^* = 2.2875$) and $f = 64$ Hz ($f_{c_0}^* = 0.016$ and $f_U^* = 1.6$), respectively. The non-dimensional total energies ($E_t^*(t) = E_s^*(t) + E_k^*(t)$) for these three different rigidities are illustrated in Fig. 15 showing oscillatory decrease (stable oscillation) of total energy for these cases. Furthermore, the transfer of energy between fluid flow and plate leads to larger amplitudes in the oscillation of the total energy compared to Fig. 13. Here, a warning is in place for the simulation with the largest stiffness $B^* = 2.6 \times 10^{-4}$. Our standard approach led to increasing total energy for $B^* = 2.6 \times 10^{-4}$, $d^* = 0$ and $m^* = 2.62$. Close inspection showed that the displacement of the structure developed high wavenumber oscillations. Solving the Euler–Bernoulli beam equation not as usual at every fluid time step, but at every other fluid time step led to a larger structure time step size, i.e., $\Delta t_s = 2\Delta t_f$. Choosing the time step size for the structure computation twice as large as the time step size for the flow computation, has a stabilizing effect and suppresses the numerical instability. Fig. 16 shows that in the presence of damping, the plate is gradually losing its oscillatory behaviour and reaches an undeformed shape. Fig. 17 compares the non-dimensional rate of work done by the fluid on the plate without damping and with two different damping coefficients. As expected, the damping coefficient has a large effect on whether the oscillations are damped or not.

3.6. Acoustic analysis

In this section, the acoustic pressure signal is analyzed to study the effect of plate oscillation on generating sound. Figs. 18 (a) and (c) demonstrate the time history of the acoustic pressure

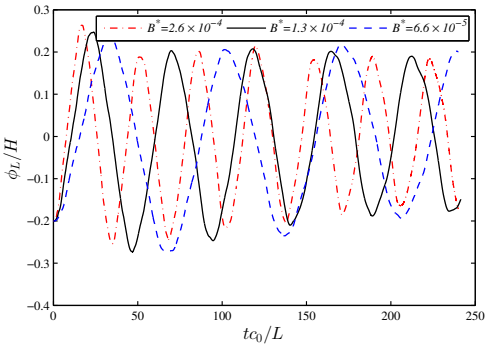

Figure 14: Time history of the tip displacement with different non-dimensional rigidities for undamped flexible plate (d^*=0) and fixed mass ($m^* = 2.62$). Note $\Delta t_s = 2\Delta t_f$ was used for $B^* = 2.6 \times 10^{-4}$.

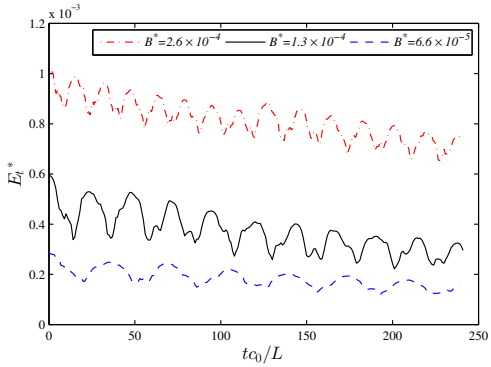

Figure 15: Evaluation of plate's total energy E_t^* for three different rigidities ($d^* = 0$, $m^* = 2.62$). Note $\Delta t_s = 2\Delta t_f$ was used for $B^* = 2.6 \times 10^{-4}$.

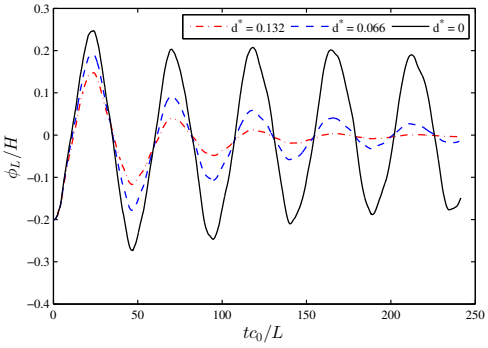

Figure 16: Time history of the tip displacement with different non-dimensional dampings and fixed mass and rigidity ($m^* = 2.62$, $B^* = 1.3 \times 10^{-4}$).

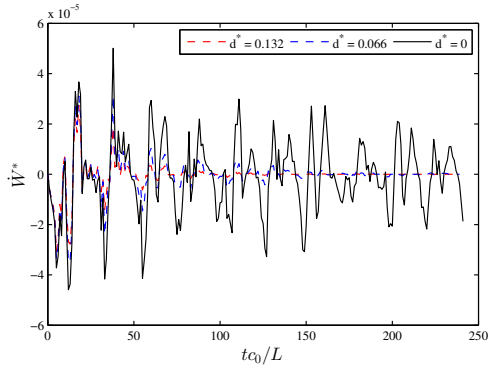

Figure 17: Variation of the non-dimensional rate of work done by the fluid on the plate ($m^* = 2.62$, $B^* = 1.3 \times 10^{-4}$).

for the simulation between $tc_0/L = 0$ and $tc_0/L = 240$. The flexible plate has its second mode initial configuration with $\phi(L,0)/H = 0.1$ as initial tip displacement. The Reynolds number and Mach number are 378 and 0.01, respectively. The initial flow field for this study was determined by simulating the flow field from $\mathbf{U}' = \mathbf{0}$, except for the inlet velocity, with the flexible plate fixed at its second mode position with $\phi(L,0)/H = 0.1$. The simulation was run until $tc_0/L = 40$, when steady state was approximately reached. The approximate solution was used as the initial condition for the present FSI for which the initial time was set as $tc_0/L = 0$. The acoustic pressure is recorded at four points, two points at $y = H/4$ and $y = 3H/4$ both near the inlet $x = L_t/10$ and near the outlet $x = 9L_t/10$, where L_t is the total length of duct and H the height of the

duct. The acoustic pressure is transformed to a spectrum by applying the fast Fourier transform (FFT), as shown in Figs. 18 (b) and (d). In the Fourier transform of the pressure signal, the frequencies as a consequence of the plate oscillation and the eigenfrequencies of the duct can be clearly distinguished.

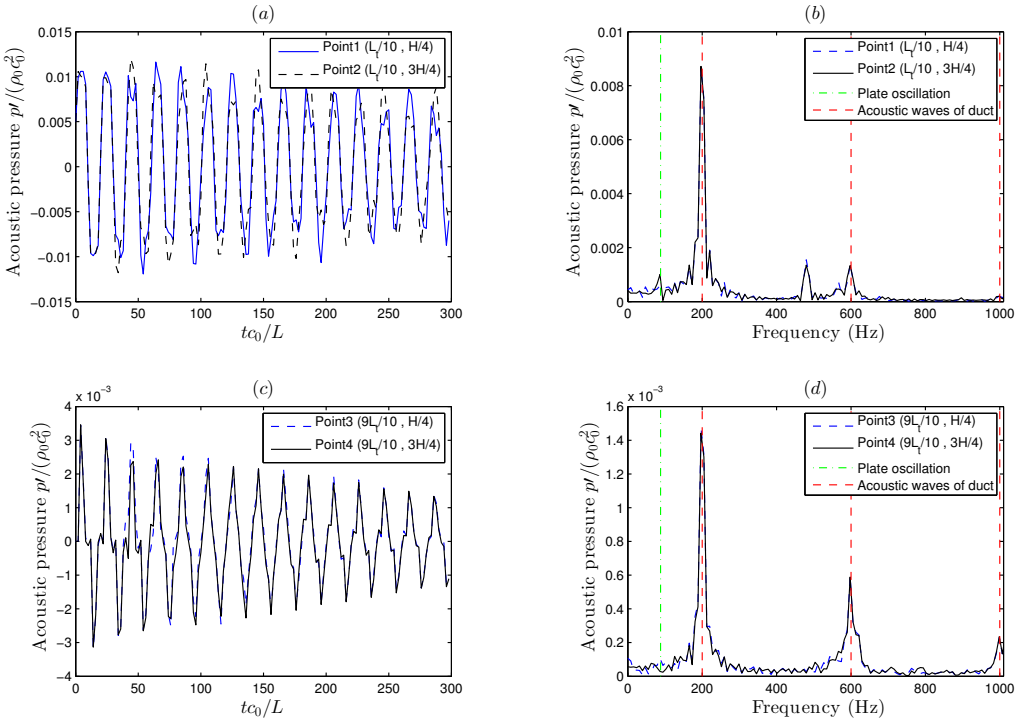

Figure 18: (a) and (c) Time history of acoustic pressure $p'/(\rho_0 c_0^2)$ at inlet and outlet, respectively; (b) and (d) Spectrum of pressure signal. The fluid flow is at Re = 378 and Ma = 0.01, the structure data are as in section 3.4, except for the initial tip displacement $\phi(L,0)/H = 0.1$. The flexible plate was released at $tc_0/L = 40$ corresponding to $tc_0/L = 0$ in plots (a) and (c).

The eigenfrequencies for an acoustically closed end duct with imposed velocity at inlet and outlet pressure (Selle et al., 2004) can be obtained as

$$f_n = (2n+1)(c/(4L_t)) \tag{19}$$

These represent the odd modes in terms of $n = 0, 1, ...$, where c is the speed of sound and L_t the total length of the duct (Selle et al., 2004). The first three modes predicted by Eq. (19) are observed in Fig. 18(b) and (d). It shows that the three first acoustic resonance frequencies of the duct appear in the spectrum of the computed pressure both near the inlet (Fig. 18(b)) and even clearer near the outlet (Fig. 18(d)).

We investigated means to reduce the reflections of the acoustic waves in the domain by means of non-reflecting boundary conditions with a simple scaling (Selle et al., 2004) and non-reflecting

boundary condition with plane wave masking (Polifke et al., 2006). However, the results using those approaches are not presented, because they were similar to the results obtained by the conditions explained in subsection 2.1.2. This similarity of the results obtained with the boundary conditions outlined in subsection 2.1.2 and with those by Selle et al. (2004) and Polifke et al. (2006) is not surprising, because those are also based on NSCBC by Poinsot and Lele (1992) like ours.

The spectrum analysis in Fig. 18(b) and (d) shows that the 1/4 wave mode (cf. Eq. (20)) pointed out by Selle et al. (2004) as the quarter wave mode frequency is dominant compared to the other harmonics and the frequency of plate oscillation.

$$f_0 = (1 - M^2)(c/(4L_t)) \tag{20}$$

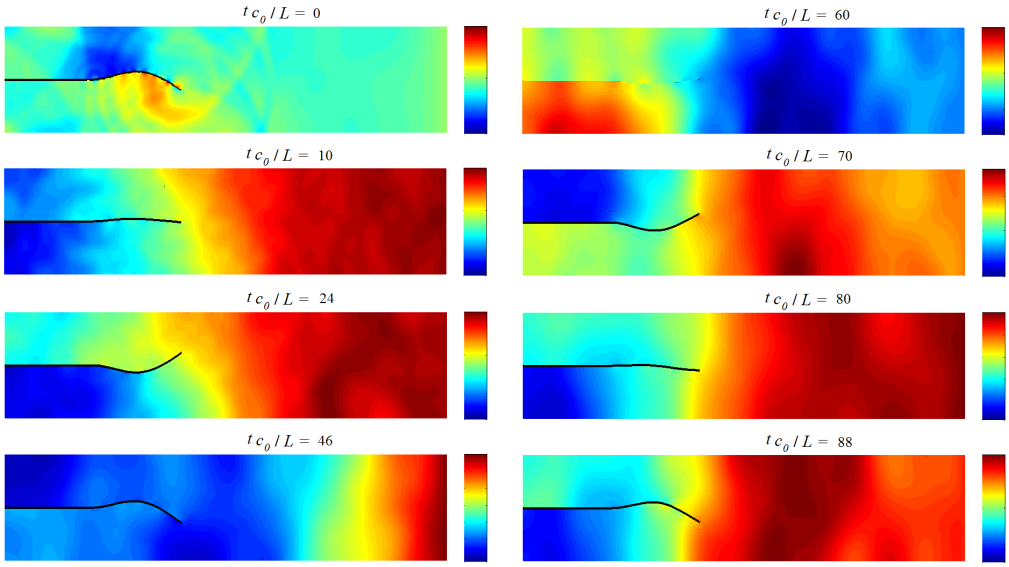

Figure 19: Time sequence showing acoustic pressure contour plots for the first two cycles of oscillation, Re = 378 and Ma = 0.01, the structure data are as in section 3.4, except for the initial tip displacement $\phi(L,0)/H = 0.1$. The outflow pressure is at $p = p_\infty$ and the contour levels are from -3 Pa to 3 Pa corresponding to $-2.48 \times 10^{-3} \leqslant p'/(\rho_0 c_0^2) \leqslant 2.48 \times 10^{-3}$.

Fig. 19 shows the acoustic pressure contours for this simulation. At $tc_0/L = 0$, low and high pressure regions are located over and below the flexible structure, respectively, because the flow there is accelerated and decelerated respectively. When the flexible structure is released at $tc_0/L = 0$, the flow field periodically changes. However, the pressure field is dominated by acoustic waves travelling back and fourth in the channel. As the inlet velocity is fixed, the acoustic pressure waves will be reflected at the inlet. When the acoustic waves hit the outlet, their amplitude will be reduced due to the partly non–reflecting property of Rudy and Strikwerda (1980) boundary treatment, cf. subsection 2.1.2. Thus, the simulated amplitudes of the acoustic pressure waves decrease by interaction with the right boundary. Viscous attenuation contributes to damping of

the acoustic waves. Eventually, the acoustic wave amplitudes decay, which can be observed in Fig. 20.

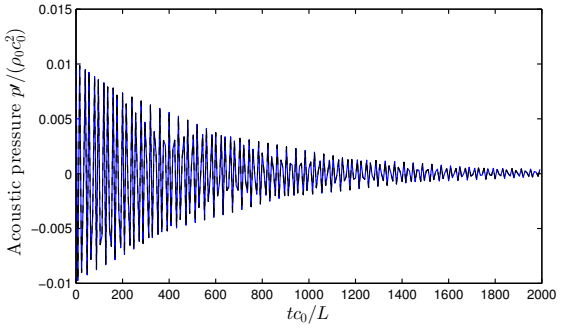

Figure 20: Time history of acoustic pressure $p'/(\rho_0 c_0^2)$ at inlet. The fluid flow is at Re = 378 and Ma = 0.01, the structure data are as in section 3.4, except for the tip displacement $\phi(L,t)/H = 0$ which the plate is a stationary straight splitter.

Therefore, we define a cutoff time $tc_0/L = 2000$ to allow the acoustic pressure to decay. The simulation is repeated with the steady state computation run until $tc_0/L = 2000$. Compared to the previous simulation, the flexible plate is not released from its second mode position with $\phi(L,0)/H = 0.1$ at $tc_0/L = 40$, but at $tc_0/L = 2000$. Fig. 21 illustrates the time history of the acoustic pressure and the frequency of the acoustic pressure spectrum for this simulation. After turning on the fluid–structure interaction at $tc_0/L = 2000$, the frequency of the oscillation of the flexible plate can be observed better due to the decayed acoustic wave amplitudes. Fig. 22 shows the results of the acoustic pressure contours for this simulation.

In Figure 21, a very noisy signal is observed compared to Fig. 18 which is associated with a very complicated behaviour of waves over a long period of time. Since the structure has a curved form, more complex reflections of the pressure waves travel through the computational domain. A plane wave hitting a plate allows reflected waves going out in many directions, hitting the top and bottom walls of the channel. Then these reflected waves interact and make a complex interference pattern which leads to build up a very noisy pressure field. Three acoustic resonance frequencies corresponding to the first three eigenfrequencies of the duct are not as sharp and are more damped compared to those of the previous simulation (cf. Fig. 18) and relatively shifted, particularly high frequencies cf. $f = 600$ Hz (non–dimensional frequencies $f^*_{c_0} = f\frac{L}{c_0} = 0.15$ and $f^*_U = f\frac{L}{U} = 15$) and 1000 Hz ($f^*_{c_0} = 0.25$ and $f^*_U = 25$). The quarter wave mode $f = 200$ Hz ($f^*_{c_0} = 0.05$ and $f^*_U = 5$) is no longer dominant. The fundamental frequency of the soft palate model oscillation $f = 91.5$ Hz ($f^*_{c_0} = 0.022875$ and $f^*_U = 2.2875$) and some harmonics can be observed. The plane waves travelling through the channel change to the circular wave nears the trailing edge (as can be seen in Fig. 19 at $tc_0/L = 0$ and in Fig. 22 at $tc_0/L = 2000$) when the plate starts to oscillate. The resonance frequency $f = 490$ Hz can be identified as a consequence of this phenomenon in both figures 18(b) and 21(b). This acoustic resonance frequency corresponds to the eigenfrequency of each of the two ducts from the inlet to the trailing edge of the flexible plate, i.e., $f = c/(4(L_{\text{rigid plate}} + L_{\text{flexible plate}})) = 500$ Hz ($f^*_{c_0} = 0.125$ and $f^*_U = 12.5$).

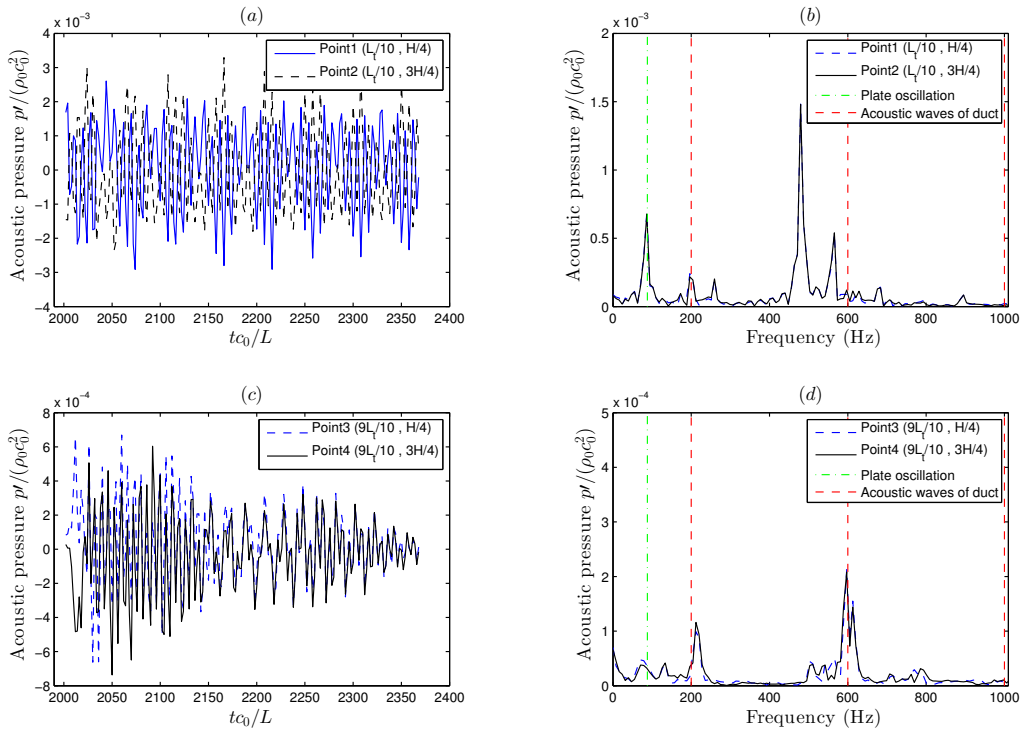

Figure 21: (a) and (c) Time history of acoustic pressure $p'/(\rho_0 c_0^2)$ at inlet and outlet, respectively; (b) and (d) Spectrum of pressure signal. The fluid flow is at Re = 378 and Ma = 0.01, the structure data are as in section 3.4, except for the initial tip displacement $\phi(L,0)/H = 0.1$. The flexible plate was released at $tc_0/L = 2000$.

4. Conclusions

A numerical approach for a simplified model of fluid–structure interaction for the soft palate in the upper airways is developed. This FSI model for the interaction between the inspiratory airflow through nose and mouth with the soft palate has been modeled as compressible viscous flow over a cantilevered flexible plate in a duct. The coupling between the fluid and the structure is handled in an arbitrary Lagrangian–Eulerian (ALE) formulation with an explicit, two–way coupling strategy where forces and deformations are exchanged between the flow and plate at the end of every time step. Strict stability and high order accuracy are obtained by employing summation by parts (SBP) difference operators, which are 6^{th} order accurate in the interior and 3^{rd} order accurate near the boundaries (Svärd and Nordström, 2014). To achieve high accuracy and easy parallelization, the 4^{th} order explicit Runge–Kutta method is applied for time integration. The motion of the cantilevered flexible plate is obtained by solving the linearized Euler–Bernoulli thin beam equation. The numerical method for computing the structure equation is based on the 2^{nd} order central finite difference method and the most accurate and unconditionally stable scheme of

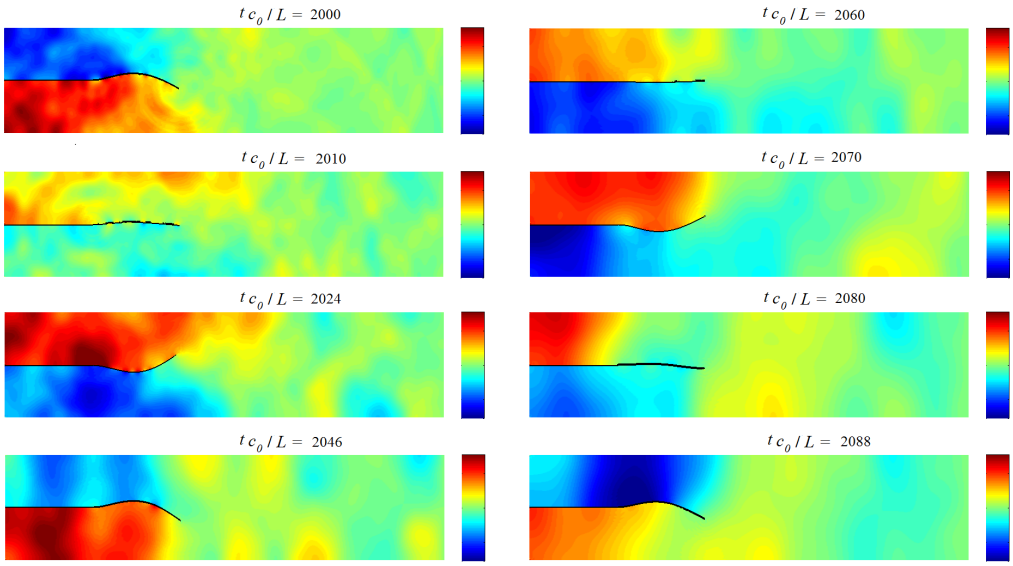

Figure 22: Time sequence showing acoustic pressure contour plots for the first two cycles of oscillation, Re = 378 and Ma = 0.01, the structure data are as in section 3.4, except for the initial tip displacement $\phi(L,0)/H = 0.1$. The outflow pressure is at $p = p_\infty$ and the contour levels are from -3 Pa to 3 Pa corresponding to $-2.48 \times 10^{-3} \leqslant p'/(\rho_0 c_0^2) \leqslant 2.48 \times 10^{-3}$.

the Newmark family.

The dependence of oscillation frequencies of the plate on the grid is studied by varying the number of grid points. The frequencies of plate are compared with the corresponding second mode eigenfrequencies of the structure to assess the required number of grid points. The dynamics of the vortices produced by the interaction of the fluid flow and the structure is investigated when both the upper and lower inlets are open and when only the upper inlet is open the lower one closed. The numerical simulations of FSI show that when both inlets are open the vortices are more stable than when one inlet is closed. Having one inlet closed creates a very complex vortical structure. Several cases are presented to investigate the oscillation behaviour of the flexible plate under different material parameters. For all cases considered, the oscillation of the plate remains stable. The highest rigidity evokes a warning. Close inspection showed that the displacement of the structure developed high wavenumber oscillations. Choosing the time step size for the structure computation twice as large as the time step size for the flow computation, has a stabilizing effect and suppresses the numerical instability. Finally, in order to identify the effect of plate oscillation as a source of sound generation in the evaluation of snoring, the acoustic pressure is analyzed. Although at the given boundary conditions the quarter wave mode is identified as dominant frequency, the frequency of the sound produced by oscillation is in good agreement with the frequency of the plate oscillation. However, the quarter wave frequency and its harmonics dominate the oscillation frequency, as long as the acoustic waves have not yet decayed sufficiently.

5. Acknowledgements

The current research is a part of a larger research project entitled "Modeling of obstructive Sleep apnea by fluid-structure interaction in the upper airways" funded by the Research Council of Norway (Larsson, 2015).

Appendix A. Summation by parts operators

To demonstrate the SBP operators, we apply the procedure to a simplified PDE, that is, rather than analysing the full Navier–Stokes equations in this section, we only focus on the 1D convection–diffusion equation as a model equation.

$$\begin{aligned} &u_t + au_x = bu_{xx}, \quad 0 \leq x \leq 1 \quad t \geq 0 \\ &u(x,0) = f(x) \\ &u(0,t) = u(1,t) = g(t) = 0 \end{aligned} \tag{A.1}$$

where a and b are assumed to be constant and positive, and u is the dependent variable.

The basis of getting such an energy estimate is to satisfy integration by parts in the discrete sense called Summation–By–Parts (SBP) property (Gustafsson, 2008; Svärd and Nordström, 2014). To outline this technique for model problem (A.1), we consider $u_j = u_j(t)$ the numerical solution of the convection–diffusion equation at grid point $x_j = jh, j = 0, ..., N$, with grid spacing $h = \frac{1}{N}$. The solution vector containing the solution at the discrete grid points is $\mathbf{u} = [u_0(t), u_1(t), ..., u_N(t)]^T$. Using a difference operator Q approximating the first derivative in space, the semi-discrete form of the model equation can be expressed as

$$\tfrac{d\mathbf{u}}{dt} = -aQ\mathbf{u} + bQQ\mathbf{u}, \quad u_j(0) = f(x_j) \tag{A.2}$$

The discrete scalar product and corresponding norm and energy can be defined by

$$\begin{aligned} &(\mathbf{u}, \mathbf{v})_h = h\mathbf{u}^T H \mathbf{v}, \\ &E_h(t) = \|\mathbf{u}\|_h^2 = (\mathbf{u}, \mathbf{u})_h \end{aligned} \tag{A.3}$$

where H is a diagonal and positive definite matrix defined by $H = \text{diag}(H_L, I, H_R)$. The SBP property is satisfied by the difference operator Q, if

$$(\mathbf{u}, Q\mathbf{v})_h = u_N v_N - u_0 v_0 - (Q\mathbf{u}, \mathbf{v})_h \tag{A.4}$$

or if Q can be written on the form $hQ = H^{-1}P$ for P satisfying

$$P + P^T = E_N - E_0 = \text{diag}(-1, 0, ..., 0, 1) \tag{A.5}$$

where $E_0 = \text{diag}(1, 0, ..., 0)$ and $E_N = \text{diag}(0, 0, ..., 1)$. Using the semi–discrete equation A.2, the energy estimate for the semi–discrete problem can be obtained as

$$\begin{aligned} \tfrac{dE}{dt} = \tfrac{d}{dt}\|u(\cdot,t)\|^2 &= (u_t, u)_h + (u, u_t)_h \\ &= (-aQu + bQQu, u)_h + (u, -aQu + bQQu)_h \\ &= -a[u_N^2 - u_0^2] + 2b[u_N(Qu)_N - u_0(Qu)_0] \\ &\quad -2b(Qu, Qu)h \leq au_0^2 + 2b[u_N(Qu)_N - u_0(Qu)_0]. \end{aligned} \tag{A.6}$$

We would get non-growing energy in time if the homogeneous boundary conditions could directly be imposed in (A.6). However, this will change the difference operator Q such that its SBP property might be lost. To avoid this problem, boundary conditions are weakly imposed by the simultaneous approximation term (SAT) technique (Gustafsson, 2008). A first derivative SBP operator with diagonal quadrature matrix H in A.3 is a $\mathcal{O}(h^{2s})$ accurate central difference operator which is $\mathcal{O}(h^s)$ accurate at and near boundaries $s = 1, 2, 3$. Such an SBP operator is globally $\mathcal{O}(h^{s+1})$ accurate.

Appendix B. Time step selection

We solve the compressible Navier–Stokes equations explicitly in time. Hence, the time step is restricted by the stability region of the Runge–Kutta method. To analyse the approach for the model (A.1), we consider that the x–derivative is approximated by a standard central p^{th} order finite difference operator $Q_x^{(p)}$ and the time–derivative by an explicit Runge–Kutta method. Therefore, the von Neumann stability analysis leads to the stability condition $\triangle t(-a\hat{Q}^{(p)} + b(\hat{Q}^{(p)})^2) \in S$, where $\hat{Q}^{(p)}$ and S are the Fourier transform of $Q_x^{(p)}$ and the stability domain of the Runge–Kutta method, respectively. The stability condition for SBP operators is more restrictive, due to the requirement $\triangle t \| - aQ_x^{(p)} + bQ_x^{(p)})^2 \|_h \leq R_1 < R$, where the open semicircle $\{z \in \mathbb{C} \mid |z| < R \text{ and } \text{Real}(z) < 0\}$ is contained in the stability domain S (Kreiss and Wu, 1993). For the standard sixth order difference operator, i.e., $(Q_x^{(6)}\mathbf{u})_j = \frac{1}{60\triangle x}(u_{j+3} - 9u_{j+2} + 45u_{j+1} - 45u_{j-1} + 9u_{j-2} - u_{j-3})$, the Fourier transform is $\hat{Q}^{(6)} = \frac{i}{\triangle x}[\frac{3}{2}\sin(k\triangle x) - \frac{3}{10}\sin(2k\triangle x) + \frac{1}{30}\sin(3k\triangle x)]$, where k is the wave number. Thus, the von Neumann stability condition for $Q_x^{(6)}$ and the classical fourth order Runge–Kutta reads $CFL = \frac{|a|\triangle t}{\triangle x} \leq 1.783$ for $b = 0$ and $VNN = \frac{|b|\triangle t}{\triangle x^2} \leq 1.124$ for $a = 0$ (Larsson and Müller, 2009).

References

Auregan, Y., Depollier, C., 1995. Snoring: Linear stability analysis and in-vitro experiments. Journal of Sound and Vibration 188, 39–53.

Balint, T., Lucey, A., 2005. Instability of a cantilevered flexible plate in viscous channel flow. Journal of Fluids and Structures 20, 893–912.

Bertram, C.D., 2008. Flow-induced oscillation of collapsed tubes and airway structures. Respiratory Physiology & Neurobiology 163, 256–265.

Brietzke, S.E., Mair, E.A., 2006. Acoustical analysis of snoring: Can the probability of success be predicted? Otolaryngology-Head and Neck Surgery 135, 417–420.

Guo, C., Païdoussis, M., 2000. Stability of rectangular plates with free side-edges in two-dimensional inviscid channel flow. Journal of Applied Mechanics 67, 171–176.

Gustafsson, B., 2008. High order difference methods for time dependent PDE. Springer, Berlin.

Gustafsson, B., Kreiss, H.O., Oliger, J., 1995. Time dependent problems and difference methods. John Wiley & Sons, New York.

Howell, R., Lucey, A., Carpenter, P., Pitman, M., 2009. Interaction between a cantilevered-free flexible plate and ideal flow. Journal of Fluids and Structures 25, 544–566.

Huang, L., 1995. Flutter of cantilevered plates in axial flow. Journal of Fluids and Structures 9, 127–147.

Huang, L., Zhang, C., 2013. Modal analysis of cantilever plate flutter. Journal of Fluids and Structures 38, 273–289.

Hughes, T.J., 2012. The finite element method: linear static and dynamic finite element analysis. Courier Corporation, New York.

Kreiss, H.O., Wu, L., 1993. On the stability definition of difference approximations for the initial boundary value problem. Applied Numerical Mathematics 12, 213–227.

Kuhl, J.M., DesJardin, P., 2012. Power production locality of bluff body flutter mills using fully coupled 2D direct numerical simulation. Journal of Fluids and Structures 28, 456–472.

Larsson, M., 2015. Welcome to the OSAS page. Http://osas.no/.

Larsson, M., Müller, B., 2009. Numerical simulation of confined pulsating jets in human phonation. Computers & Fluids 38, 1375–1383.

Larsson, M., Müller, B., 2012. High–order numerical simulation of fluid–structure interaction in the human larynx. Progress in Computational Fluid Dynamics, an International Journal 12, 164–175.

Malhotra, A., White, D.P., 2002. Obstructive sleep apnoea. The Lancet 360, 237–245.

Müller, B., 2008. High order numerical simulation of aeolian tones. Computers & Fluids 37, 450–462.

Newmark, N.M., 1959. A method of computation for structural dynamics. Journal of the Engineering Mechanics Division 85, 67–94.

Peyret, R., Viviand, H., Smolderen, J., 1975. Computation of viscous compressible flows based on the Navier-Stokes equations. NASA STI/Recon Technical Report N 76, 11380.

Poinsot, T.J., Lele, S., 1992. Boundary conditions for direct simulations of compressible viscous flows. Journal of Computational Physics 101, 104–129.

Polifke, W., Wall, C., Moin, P., 2006. Partially reflecting and non-reflecting boundary conditions for simulation of compressible viscous flow. Journal of Computational Physics 213, 437–449.

Pulliam, T.H., Steger, J.L., 1980. Implicit finite-difference simulations of three-dimensional compressible flow. AIAA Journal 18, 159–167.

Rudy, D.H., Strikwerda, J.C., 1980. A nonreflecting outflow boundary condition for subsonic Navier-Stokes calculations. Journal of Computational Physics 36, 55–70.

Selle, L., Nicoud, F., Poinsot, T., 2004. Actual impedance of nonreflecting boundary conditions: Implications for computation of resonators. AIAA Journal 42, 958–964.

Sesterhenn, J., Müller, B., Thomann, H., 1999. On the cancellation problem in calculating compressible low Mach number flows. Journal of Computational Physics 151, 597–615.

Shoele, K., Mittal, R., 2016. Flutter instability of a thin flexible plate in a channel. Journal of Fluid Mechanics 786, 29–46.

Strand, B., 1994. Summation by parts for finite difference approximations for d/dx. Journal of Computational Physics 110, 47–67.

Svärd, M., Nordström, J., 2014. Review of summation-by-parts schemes for initial–boundary-value problems. Journal of Computational Physics 268, 17–38.

Tang, L., Païdoussis, M.P., 2007. On the instability and the post-critical behaviour of two-dimensional cantilevered flexible plates in axial flow. Journal of Sound and Vibration 305, 97–115.

Tang, L., Païdoussis, M.P., 2008. The influence of the wake on the stability of cantilevered flexible plates in axial flow. Journal of Sound and Vibration 310, 512–526.

Tetlow, G., Lucey, A.D., 2009. Motions of a cantilevered flexible plate in viscous channel flow driven by a constant pressure drop. Communications in Numerical Methods in Engineering 25, 463–482.

Tian, F.B., Dai, H., Luo, H., Doyle, J.F., Rousseau, B., 2014. Fluid–structure interaction involving large deformations: 3D simulations and applications to biological systems. Journal of Computational Physics 258, 451–469.

Visbal, M.R., Gaitonde, D.V., 2002. On the use of higher-order finite-difference schemes on curvilinear and deforming meshes. Journal of Computational Physics 181, 155–185.

Wu, Y., Cai, X.C., 2014. A fully implicit domain decomposition based ALE framework for three-dimensional fluid–structure interaction with application in blood flow computation. Journal of Computational Physics 258, 524–537.

Young, T., Palta, M., Dempsey, J., Skatrud, J., Weber, S., Badr, S., 1993. The occurrence of sleep-disordered breathing among middle-aged adults. New England Journal of Medicine 328, 1230–1235.

Paper II [54]

Computational study of flow-induced oscillation of a simplified soft palate

M. E. Khalili, M. Larsson, B. Müller

Coupled Problems in Science and Engineering VII
CIMNE (2017), 582–593.

VII International Conference on Computational Methods for Coupled Problems in Science and Engineering
COUPLED PROBLEMS 2017
M. Papadrakakis, E. Oñate and B. Schrefler (Eds)

COMPUTATIONAL STUDY OF FLOW–INDUCED OSCILLATION OF A SIMPLIFIED SOFT PALATE

M. Ehsan Khalili*, Martin Larsson † and Bernhard Müller *

* Department of Energy and Process Engineering
Norwegian University of Science and Technology (NTNU)
Kolbjørn Hejes vei 2, NO-7491 Trondheim, Norway
e-mail: {mohammadtaghi.khalili, bernhard.muller}@ntnu.no

† Sportradar AS
Ferjemannsveien 10, NO-7014 Trondheim, Norway
e-mail: m.larsson@sportradar.com

Key words: Fluid structure interaction; High order finite difference method; Arbitrary Lagrangian–Eulerian formulation

Abstract. Two-dimensional numerical simulations are employed to study fluid structure interaction of a simplified model of the soft palate in the pharynx for uniform inhalation. We take a next step towards a better biomechanical system by modeling the motion of an inextensible flexible plate. The improved structural model discretized by a low order difference method permits us to simulate the two-dimensional motion of the flexible plate. The inspiratory airflow is described by the Navier–Stokes equations for compressible flow solved by a high order difference method. The explicitly coupled fluid structure interaction model is based on the Arbitrary Lagrangian–Eulerian formulation.

1 Introduction

Fluid structure interaction (FSI) refers to the interaction of a flexible structure with fluid flow where the fluid and structure interact over a shared interface. FSI gives rise to a rich variety of physical phenomena with applications in many fields of engineering and biomechanics. One of the prime examples of FSI in biomechanical systems is the dynamics of the upper airways where the interaction between inspiratory and expiratory airflow with soft tissues may lead to flow-induced oscillations and instabilities. Failure to maintain the patency of the upper airway during sleep characterizes obstructive sleep apnea (OSA), a common and disabling disorder wherein the soft palate obstructs the upper airways for prolonged periods of time during sleep. OSA and snoring are closely related to the flow conditions in the upper airways. Snoring is often considered a minor affliction. But when snoring is heavy, it is often associated with the more crippling condition known as OSA.

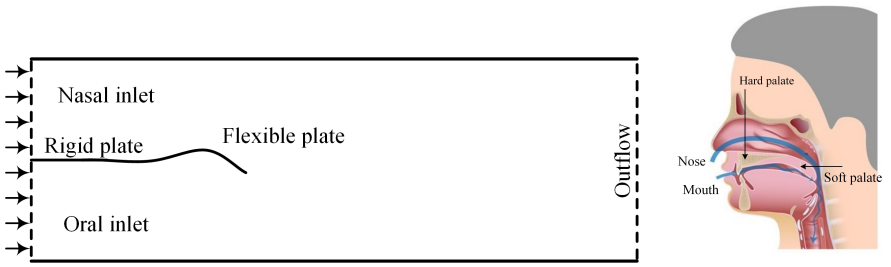

(a) Schematic of the computational model

(b) The anatomy of upper airways.

Figure 1: Computational model and real geometry.

Estimates show that the obstructive sleep apnea syndrome (OSAS) affects 2–4% of the adult population [1] and 10% of snorers are at risk of OSAS [2].

A cantilevered flexible plate immersed in two-dimensional channel flow has previously been shown to capture FSI representative of respiratory airflow and soft-palate dynamics in the upper airway [3, 4, 5, 6]. This is a well-established model wherein a flexible plate representing the soft palate is mounted downstream of a rigid plate representing the hard palate. The rigid plate separates the upper and lower channel flows modeling the flow in the oral and nasal tracts, which interact with the flexible plate motion and then combine into a single channel flow representing the flow in the pharynx, as illustrated in Fig. 1. In these studies, an inviscid flow model was used and viscous effects were implicitly modeled either through the imposition of the Kutta–Joukowski condition [3, 5, 6] or an applied channel resistance [4].

Latterly, researchers have modeled the effects of fluid viscosity explicitly for the laminar regime of Reynolds numbers [7] and investigated constant pressure-drop boundary conditions [8]. In these studies across the low-to-high range of Reynolds numbers, thin plates have been observed to lose their stability at a critical value of flow speed or Reynolds number based on channel height. The destabilization mechanism has been attributed to an irreversible energy transfer from the fluid flow to the plate arising from a phase difference between fluid pressure and plate motion owing to the finite length of the flexible plate [6, 7, 9]. Recently, compressible viscous flow has been employed for this model to characterize the acoustic wave propagation induced by the plate oscillation [10].

In all the studies mentioned above, linear structural mechanics was taken into account by using the one-dimensional Euler–Bernoulli beam equation. Another structural model has been developed by including an inextensibility condition, however, in the interaction with potential flow [11]. Apparently, the soft palate undergoes displacements beyond the linear range, particularly during episodes of obstructed breathing. The soft tissue in the palate is also nearly incompressible and is subjected to fluid friction in a viscous flow field.

Accordingly, the present work accounts for those effects and thereby yields a more faithful biomechanical FSI model. To achieve this, we extend our previous cantilevered plate model [10] to a two-dimensional elastic plate model having an inextensibility condition immersed in compressible viscous flow. This paper presents the development of the improved FSI model and then demonstrates its applicability in simulating flow-induced oscillation of a flexible plate and the characterization of its behaviour in the upper airway.

After outlining the flow and structure models as well as their coupling for FSI, the in-vacuum oscillation of the plate is presented through a verification study of the structural mechanism. Thereafter, the FSI model is used to simulate the flow-induced oscillation of a flexible plate.

2 Model

2.1 Fluid flow

The fluid motion is described by the 2D compressible Navier–Stokes equations in perturbation form. The perturbation formulation is employed to minimize cancellation errors when discretizing the Navier–Stokes equations for compressible low Mach number flow [12, 13, 14]. The conservative form of the 2D compressible Navier–Stokes equations in perturbation formulation can be written as

$$\mathbf{U}'_t + \mathbf{F}^{c\prime}{}_x + \mathbf{G}^{c\prime}{}_y = \mathbf{F}^{v\prime}{}_x + \mathbf{G}^{v\prime}{}_y \ , \tag{1}$$

where $\mathbf{U}' = \mathbf{U} - \mathbf{U_0}$ is the vector of conservative perturbation variables with $\mathbf{U} = (\rho, \rho u, \rho v, \rho E)^T$ the vector of the conservative variables and $\mathbf{U}_0 = (\rho_0, 0, 0, (\rho E)_0)^T$ the stagnation values. For a complete description of the compressible flow equations, see [10].

2.1.1 Discretization of the compressible Navier–Stokes equations

The high order finite difference method based on summation by parts (SBP) operators [15, 16, 17] is employed for space discretization of the compressible Navier–Stokes equations. We use a globally fourth order SBP operator to discretize the first derivatives and apply them twice to approximate the second derivatives in the viscous terms. The SBP operators correspond to the sixth order central difference operator in the interior, but degrade to third order accuracy near the boundary resulting in fourth order global accuracy [16]. This approach is based on the energy method, which permits us to derive well-posedness for the continuous problem and to guarantee stability for the discrete problem. For the time integration process, the classical fourth order explicit Runge–Kutta method is used. The multi-block structured grid approach is employed to represent the simplified geometry in the upper airways.

Adiabatic no-slip boundary conditions are applied at the walls and the fluid-structure interface. At the inflow, the velocities in the x- and y-directions are imposed using a uniform inlet profile normal to the boundary, $u(x = 0, t) = U_0$ and $v = 0$. In addition,

the inlet temperature is set to $T = T_0 = 310$ K. The outlet pressure is set to atmospheric pressure, i.e., $p' = p - p_0 = p - p_{\text{atm}} = 0$ Pa. The Navier–Stokes characteristic boundary conditions (NSCBC) developed by [18] are employed at the inflow and outflow boundaries to minimize wave reflections. The details of this numerical algorithm and boundary conditions can be found in our previous publication [10].

2.2 The structure model

The plate model is central in order to obtain physical results for simulating the soft palate motion. In the present study, the soft palate is modeled as a two–dimensional, massive, flexible and inextensible plate. This model provides the correlation between the elastic deflection of the plate and the applied force. The flexible plate has its own material density ρ_s, different from the surrounding fluid density ρ_f. The flexibility allows the plate to bend and to react to the force applied by the fluid flow and the flexural force generating a restoring force. Taking into account the inextensibility constraint, the length of the plate remains constant even if an external force is acting on it.

The dynamics of the plate in Lagrangian coordinate s along its undeformed reference configuration can be described by the following equation [19]

$$\rho_s \frac{\partial^2 \mathbf{X}}{\partial t^2} = \frac{\partial}{\partial s}\Big(T\frac{\partial \mathbf{X}}{\partial s}\Big) - \frac{\partial^2}{\partial s^2}\Big(K_B \frac{\partial^2 \mathbf{X}}{\partial s^2}\Big) + \rho_s \mathbf{g} + \mathbf{F}, \tag{2}$$

where s is the arclength, $\mathbf{X} = (x(s,t), y(s,t))^T$ denotes the material position of the plate, T is the tension along the Lagrangian coordinate s, K_B is the flexural rigidity, $\mathbf{g}$ the gravitational acceleration, and $\mathbf{F}$ is the force applied on the plate by the surrounding fluid. Furthermore, ρ_s is the actual line density of the plate defined as the line density difference between the thin plate and the surrounding fluid $\rho_s = \rho - \rho_f A$, where ρ is density of the plate, ρ_f the density of the fluid and A is the cross sectional area of the plate.

The inextensibility constraint of the plate [20, 19], i.e. the local stretching of the plate satisfies $\frac{d}{dt}|\frac{\partial \mathbf{X}}{\partial s}| = 0$, can be expressed as

$$\frac{\partial \mathbf{X}}{\partial s} \cdot \frac{\partial \mathbf{X}}{\partial s} = 1. \tag{3}$$

Following the previous studies [20, 19], the tension T in this model is determined by a Poisson equation derived by inserting the constraint of inextensibility Eq. (3) into the dot product of $\frac{\partial \mathbf{X}}{\partial s}$ and the $s-$derivative of the plate dynamical equation Eq. (2)

$$\frac{\partial \mathbf{X}}{\partial s} \cdot \frac{\partial^2}{\partial s^2}\Big(T\frac{\partial \mathbf{X}}{\partial s}\Big) = \frac{\rho_s}{2}\frac{\partial^2}{\partial t^2}\Big(\frac{\partial \mathbf{X}}{\partial s} \cdot \frac{\partial \mathbf{X}}{\partial s}\Big) - \rho_s \frac{\partial^2 \mathbf{X}}{\partial t \partial s} \cdot \frac{\partial^2 \mathbf{X}}{\partial t \partial s} - \frac{\partial \mathbf{X}}{\partial s} \cdot \frac{\partial}{\partial s}\Big(\mathbf{F}_B + \mathbf{F}\Big) \tag{4}$$

where $\mathbf{F}_B$ is the bending force which by using the Euler–Bernoulli assumption for a thin flexible plate is expressed as

$$\mathbf{F}_B = -\frac{\partial^2}{\partial s^2}\left(K_B \frac{\partial^2 \mathbf{X}}{\partial s^2}\right) \tag{5}$$

The non-dimensional parameters are chosen with respect to the stagnation density ρ_0, stagnation speed of sound c_0 and the length of the flexible plate L, in the same way as for the fluid solver.

The boundary conditions are specified at the free end ($s = L$) and at the fixed end at ($s = 0$) of the plate. The free end boundary condition at the trailing edge is imposed by assuming that the tension, bending moment and shear force are zero

$$T(L,t) = 0, \quad \left.\frac{\partial^2 \mathbf{X}}{\partial s^2}\right|_{s=L} = 0, \quad \left.\frac{\partial^3 \mathbf{X}}{\partial s^3}\right|_{s=L} = 0 \tag{6}$$

The support mechanism at the leading edge is taken into account as

$$\mathbf{X}|_{s=0} = \mathbf{X}_0, \quad \left.\frac{\partial^2 \mathbf{X}}{\partial s^2}\right|_{s=0} = 0 \tag{7}$$

2.2.1 Discretization of the structure model

The discretisation of the governing equation of the plate motion (2) along s is performed on a staggered grid following [19]. The plate is discretized with a finite number of Lagrangian points $\mathbf{X}_i$. The plate tension is defined at the interfaces of the grid cells, and other variables are defined at the primary grid points in the centers of the grid cells, as shown in Fig. 2

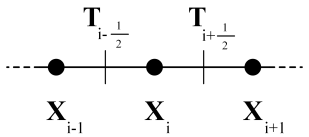

Figure 2: Schematic diagram of staggered grid discretisation on the plate along its Lagrangian coordinate.

Then, the numerical procedure for the non-dimensionalised form of Eqs. (2) and (3) is as follows

$$\mathbf{X}^* = 2\mathbf{X}_i^n - \mathbf{X}_i^{n-1} \tag{8}$$

$$\mathbf{F}_B^* = -D_{ss}(K_B\ D_{ss}\mathbf{X}^*)_i^n \tag{9}$$

$$(D_s\mathbf{X}^*)_{i+\frac{1}{2}} \cdot \left(D_s(D_s(T^{n+\frac{1}{2}}_{i+\frac{1}{2}} D_s\mathbf{X}^*))\right) = \rho_s \frac{1 - 2(D_s\mathbf{X} \cdot D_s\mathbf{X})^n_{i+\frac{1}{2}} + (D_s\mathbf{X} \cdot D_s\mathbf{X})^{n-1}_{i+\frac{1}{2}}}{2\Delta t^2} - \rho_s(D_s\mathbf{V} \cdot D_s\mathbf{V})^n_{i+\frac{1}{2}} - (D_s\mathbf{X}^*)^n_{i+\frac{1}{2}} \cdot \left(D_s(\mathbf{F}^*_B + \mathbf{F}^n)\right)_{i+\frac{1}{2}} \tag{10}$$

$$\rho_s \frac{\mathbf{X}^{n+1}_i - \mathbf{X}^*_i}{\Delta t^2} = \left(D_s(T^{n+\frac{1}{2}} D_s\mathbf{X}^{n+1})\right)_i + (\mathbf{F}_B)^{n+1} + \mathcal{G}\frac{\mathbf{g}}{|g|} + \mathbf{F}^n_i \tag{11}$$

where D_s and D_{ss} are the second order accurate difference operators for the first and second derivatives along s, respectively, and $\mathbf{X}^*$ is the predicted position of the plate. Employing $\mathbf{X}^*$ to calculate the tension helps to reduce the error. The tension is computed at the intermediate step, i.e. $t^{n+\frac{1}{2}}$ and is employed to update the position of the plate, i.e. $\mathbf{X}^{n+1}$. The velocity of the plate is defined as $\mathbf{V}^n_i = (\mathbf{X}^n_i - \mathbf{X}^{n-1}_i)/\Delta t$. $\mathbf{F}^n$ denotes the force exerted by the fluid flow on the structure and is obtained explicitly using the fluid solver at time level n. $\mathcal{G}$ is defined as the non-dimensional gravity $\mathcal{G} = gL/c_0^2$. Equations (10) and (11) constitute diagonally dominant tri- and pentadiagonal linear systems, which are solved by LU decomposition without pivoting, i.e. by the Thomas algorithm and a similar algorithm, respectively. The condition for diagonal dominance of the matrix in Eq. (11) is $K_B\frac{\Delta t^2}{\Delta s^4} \leqslant \frac{1}{4}$.

2.3 Fluid structure interaction

To handle the fluid flow in Eulerian description using moving fluid grids and the plate structure in a Lagrangian formulation using stationary structure grids, the Arbitrary Lagrangian–Eulerian (ALE) formulation is appropriately employed. Considering the velocity of the fluid grids $\dot{x}$ and $\dot{y}$ in the time-dependent coordinate transformation of the fluid flow domain, the grid point velocities are subtracted from the fluid velocity to define the contravariant velocity components $U = \xi_x(u-\dot{x})+\xi_y(v-\dot{y})$ and $V = \eta_x(u-\dot{x})+\eta_y(v-\dot{y})$ which yield simple expressions for the transformed inviscid flux vectors $\hat{\mathbf{F}}^c$ and $\hat{\mathbf{G}}^c$ [21]. The mesh update is implemented by remeshing the whole fluid domain in each time step using the positions and velocities of the flexible structure at the boundary and a linear interpolation for interior points in the fluid domain.

Solving fluid flow on a moving mesh, the numerical scheme should satisfy the Geometric Conservation Law (GCL) for mathematical consistency [22], which leads to the 2D Navier-Stokes equations in ALE formulation [23] being expressed as

$$\mathbf{U}'_\tau = \tfrac{1}{J^{-1}}(-\hat{\mathbf{F}}'_\xi - \hat{\mathbf{G}}'_\eta - (J^{-1})_\tau \mathbf{U}'). \tag{12}$$

An explicit, two-way method where forces and deformations are exchanged between the flow and the deformable structure in each time-step is employed to handle the coupling between the fluid and the structure. The fluid and structure interact with each other by applying equal displacement and velocity at the interface, satisfying the no-slip and adiabatic wall boundary conditions. The force exerted by the fluid flow on the plate at

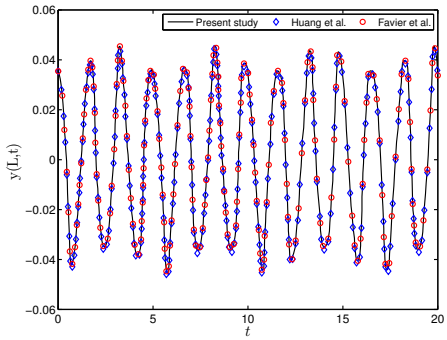

Figure 3: Time history of the y-coordinate position of the trailing edge of the plate subjected to only gravity, without bending force $K_B = 0$. The solid line shows the present model, circles present the results of the study performed by Huang et al. [19] and diamonds represent the results of the study done by Favier et al. [24].

time level n in equations (10) and (11) is given by $\mathbf{F}^n = -(p_U^n - p_L^n)\mathbf{n}$, where p_U and p_L are the pressures on the upper side and lower side of the plate, respectively, and $\mathbf{n}$ is the outer unit vector normal to the plate.

3 Results and discussion

3.1 Verification of structure solver in vacuum

The accuracy of the numerical model of the plate has been first tested and verified by simulating the oscillation and bending of the plate subjected to the gravity force in the absence of surrounding fluid, i.e. a pendulum with gravity acting in the $x-$direction. The plate was initially deformed by using the following initial configuration

$$\mathbf{X}(s,0) = \mathbf{X}_0 + s(\cos\theta, \sin\theta), \quad s \in [0, L], \tag{13}$$

where L is the length of the plate, θ is an angle and $\mathbf{X}_0 = (0,0)$. This particular configuration within the small angle approximation is considered in previous studies [19, 24]. Following them, the test is first performed by setting the initial angle of the plate to $\theta = 0.01\pi$ with a flexural stiffness $K_B = 0$ and non-dimensional gravity equivalent to $\gamma = 10$. The length of the plate is $L = 1$, and it is discretized by $N = 101$ grid points along the Lagrangian coordinate s. The time variation of the y coordinate of the trailing edge is monitored and shown in Fig. 3.

A second verification test is performed for a larger initial deflection angle $\theta = 0.1\pi$ and by including the non-dimensional bending force with $K_B = 0.01$. Fig. 4 illustrates the y-displacement of the trailing edge and the time variation of the plate deformation.

The results obtained in Figures 3 and 4(a) are in good agreement in comparison with

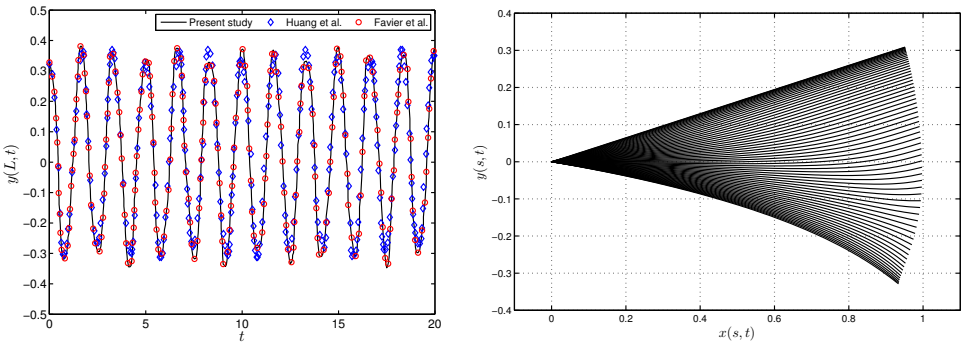

(a) (b)

Figure 4: (a) Time history of the y-coordinate position of the trailing edge of the plate subjected to only gravity $\gamma = 10$, with bending force $K_B = 0.01$. The solid line shows the present model, circles present the results of the study performed by Huang et al. [19] and diamonds represent the results of the study done by Favier et al. [24], (b) The sequence of superposition of the plate from up to down between time $0 - 0.8$.

the available numerical results [19, 24].

3.2 Numercal results of FSI

Having established the credibility of the structural model, we now couple the structure and fluid models to investigate their interaction. The computational domain is a rectangular channel with $0 \leq x \leq 9L$ and $0 \leq y \leq 4L$ where L is the length of the flexible plate. The flexible plate modeling the soft palate is attached to a rigid plate with length L representing the hard palate. The origin of the rigid plate is located in the middle of the height of the channel. Therefore, the leading edge of the flexible plate is placed at $(L, 2L)$. Overall, the computational domain is discretized by 581×281 grid points in longitudinal and transversal directions, respectively. The Reynolds number $\mathrm{Re} = \frac{\rho UL}{\mu} = 378$ and the Mach number $\mathrm{Ma} = \frac{U}{c_0} = 0.1$ are used based on the inlet velocity, density, viscosity, speed of sound and the plate length. The nondimensional line density $\frac{\rho_s}{\rho_0 L}$ is 1, and the nondimensional flexural rigidity $\frac{K_B}{\rho_0 c_0^2 L^3} = 0.0001$ is used. The plate is discretized by $N = 81$ grid points and $\frac{\Delta t c_0}{L} = 0.001$ is chosen. The initial configuration of the flexible plate is a straight line like in the previous section with $\theta = -0.04\pi$. The flexible plate has been fixed to its initial displacement until an approximately steady state flow solution is reached at $\frac{tc_0}{L} = 60$. Then, the flexible plate is released from its initial position and allowed to interact with the flow.

Fig. 5 represents the y-displacement of the trailing edge and the time variation of the plate deformation. The amplitude of the oscillation is decreasing, and the frequency is

about $\frac{fL}{c_0} = 0.6$.

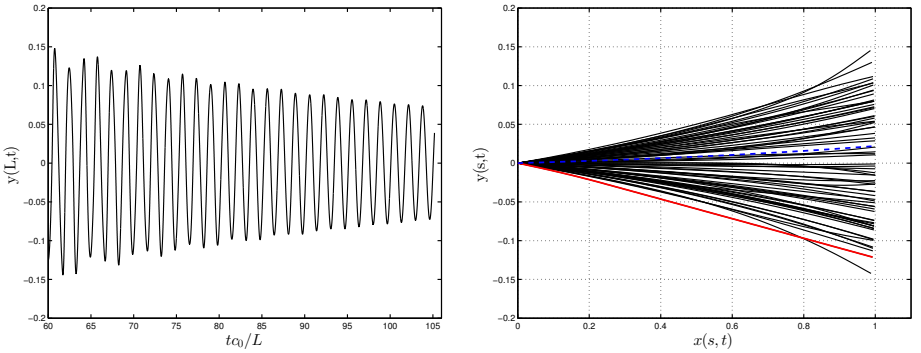

(a) (b)

Figure 5: (a) Time history of the y-coordinate position of the trailing edge of the plate in FSI. (b) Sequence of flexible plate deformation from $tc_0/L = 60$ to $tc_0/L = 105$, the initial and final deformation are marked by the red solid line and the blue dashed line, respectively.

Fig. 6 shows the instantaneous spanwise vorticity contours in the left column and the corresponding pressure field on the right at five time instants. The plate is released to oscillate at nondimensional time $tc_0/L = 60$. The plate oscillation produces a strong acoustic wave near the trailing edge of the plate. The wave hits the top and bottom wall of the channel and the reflected waves propagate into the domain, hitting waves newly produced by oscillating plate and waves reflected at the inlet. These reflected waves interact and produce a complex interference pattern which leads a very noisy pressure field. The complexity of the reflections and vicinity of the inlet boundary imposing uniform flow to the trailing edge lead to a build-up of vortices near the inlet. Behind the trailing edge of the oscillating plate, a complex vorticity pattern is observed.

4 Conclusions

In the present study, we have implemented a two-dimensional structure model to interact with compressible viscous flow in order to simulate the fluid structure interaction for a simplified model of the soft palate in the pharynx. The soft palate is modeled as a deformable inextensible plate. The FSI algorithm is based on the Arbitrary Lagrangian–Eulerian formulation with an explicit, two-way coupling strategy. The 2D compressible Navier–Stokes equations are computed by highly stable high order summation by parts (SBP) difference operators. The explicit Runge–Kutta method is applied for time integration. The structure model is solved by an implicit second order difference method to determine the flexible plate motion. The accuracy of the structural solver has been as-

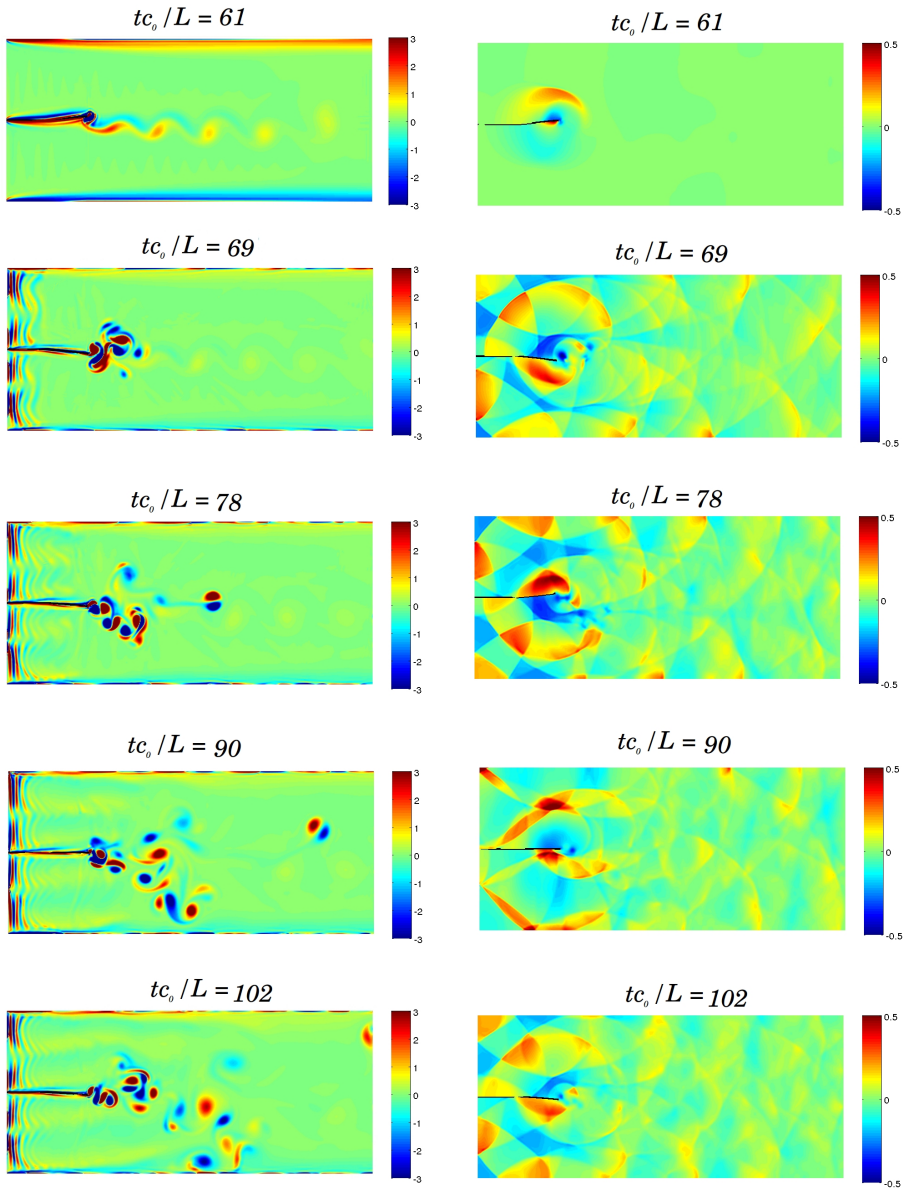

Figure 6: The left column shows the time sequence of vorticity contour plots, $\frac{\omega_z L}{c_0}$, and the right column presents the corresponding acoustic pressure contour plots, $\frac{p'}{\rho_0 c_0}$, at Re = 378 and Ma = 0.1.

sessed through comparisons with previous numerical results. The flow-induced oscillation of the plate is simulated for low Reynolds and Mach numbers. Strong acoustic waves are produced by the oscillating plate. Complex pressure and vorticity patterns are observed.

REFERENCES

[1] T. Young, M. Palta, J. Dempsey, J. Skatrud, S. Weber, and S. Badr, "The occurrence of sleep-disordered breathing among middle-aged adults," *New England Journal of Medicine*, vol. 328, no. 17, pp. 1230–1235, 1993.

[2] C. D. Bertram, "Flow-induced oscillation of collapsed tubes and airway structures," *Respiratory Physiology & Neurobiology*, vol. 163, no. 1, pp. 256–265, 2008.

[3] L. Huang, "Flutter of cantilevered plates in axial flow," *Journal of Fluids and Structures*, vol. 9, no. 2, pp. 127–147, 1995.

[4] Y. Auregan and C. Depollier, "Snoring: Linear stability analysis and in-vitro experiments," *Journal of Sound and Vibration*, vol. 188, no. 1, pp. 39–53, 1995.

[5] C. Guo and M. Païdoussis, "Stability of rectangular plates with free side-edges in two-dimensional inviscid channel flow," *Journal of Applied Mechanics*, vol. 67, no. 1, pp. 171–176, 2000.

[6] R. Howell, A. Lucey, P. Carpenter, and M. Pitman, "Interaction between a cantilevered-free flexible plate and ideal flow," *Journal of Fluids and Structures*, vol. 25, no. 3, pp. 544–566, 2009.

[7] T. Balint and A. Lucey, "Instability of a cantilevered flexible plate in viscous channel flow," *Journal of Fluids and Structures*, vol. 20, no. 7, pp. 893–912, 2005.

[8] G. Tetlow and A. D. Lucey, "Motions of a cantilevered flexible plate in viscous channel flow driven by a constant pressure drop," *Communications in Numerical Methods in Engineering*, vol. 25, no. 5, pp. 463–482, 2009.

[9] L. Tang, M. P. Païdoussis, and J. Jiang, "Cantilevered flexible plates in axial flow: energy transfer and the concept of flutter-mill," *Journal of Sound and Vibration*, vol. 326, no. 1, pp. 263–276, 2009.

[10] M. Khalili, M. Larsson, and B. Müller, "Interaction between a simplified soft palate and compressible viscous flow," *Journal of Fluids and Structures*, vol. 67, pp. 85–105, 2016.

[11] L. Tang and M. P. Païdoussis, "On the instability and the post-critical behaviour of two-dimensional cantilevered flexible plates in axial flow," *Journal of Sound and Vibration*, vol. 305, no. 1, pp. 97–115, 2007.

[12] J. Sesterhenn, B. Müller, and H. Thomann, "On the cancellation problem in calculating compressible low Mach number flows," *Journal of Computational Physics*, vol. 151, no. 2, pp. 597–615, 1999.

[13] B. Müller, "High order numerical simulation of aeolian tones," *Computers & Fluids*, vol. 37, no. 4, pp. 450–462, 2008.

[14] M. Larsson and B. Müller, "Numerical simulation of confined pulsating jets in human phonation," *Computers & Fluids*, vol. 38, no. 7, pp. 1375–1383, 2009.

[15] B. Strand, "Summation by parts for finite difference approximations for d/dx," *Journal of Computational Physics*, vol. 110, no. 1, pp. 47–67, 1994.

[16] B. Gustafsson, *High order difference methods for time dependent PDE*. Berlin: Springer, 2008.

[17] B. Gustafsson, H.-O. Kreiss, and J. Oliger, *Time dependent problems and difference methods*. New York: John Wiley & Sons, 1995.

[18] T. J. Poinsot and S. Lele, "Boundary conditions for direct simulations of compressible viscous flows," *Journal of Computational Physics*, vol. 101, no. 1, pp. 104–129, 1992.

[19] W.-X. Huang, S. J. Shin, and H. J. Sung, "Simulation of flexible filaments in a uniform flow by the immersed boundary method," *Journal of Computational Physics*, vol. 226, no. 2, pp. 2206–2228, 2007.

[20] A.-K. Tornberg and M. J. Shelley, "Simulating the dynamics and interactions of flexible fibers in Stokes flows," *Journal of Computational Physics*, vol. 196, no. 1, pp. 8–40, 2004.

[21] T. H. Pulliam and J. L. Steger, "Implicit finite-difference simulations of three-dimensional compressible flow," *AIAA Journal*, vol. 18, no. 2, pp. 159–167, 1980.

[22] M. R. Visbal and D. V. Gaitonde, "On the use of higher-order finite-difference schemes on curvilinear and deforming meshes," *Journal of Computational Physics*, vol. 181, no. 1, pp. 155–185, 2002.

[23] R. Peyret, H. Viviand, and J. Smolderen, "Computation of viscous compressible flows based on the Navier-Stokes equations," *NASA STI/Recon Technical Report N*, vol. 76, p. 11380, 1975.

[24] J. Favier, A. Revell, and A. Pinelli, "A lattice Boltzmann–immersed boundary method to simulate the fluid interaction with moving and slender flexible objects," *Journal of Computational Physics*, vol. 261, pp. 145–161, 2014.

Paper III [56]

Immersed boundary method for the compressible Navier-Stokes equations using high order summation-by-parts difference operators

M. E. Khalili, M. Larsson, B. Müller

12th International Conference on Computational Fluid Dynamics In the Oil & Gas, Metallurgical and Process Industries
SINTEF (2017), 233–242.

IMMERSED BOUNDARY METHOD FOR THE COMPRESSIBLE NAVIER–STOKES EQUATIONS USING HIGH ORDER SUMMATION-BY-PARTS DIFFERENCE OPERATORS

M. EHSAN KHALILI[1*], **MARTIN LARSSON**[2†], **BERNHARD MÜLLER**[1‡]

[1]Department of Energy and Process Engineering, Norwegian University of Science and Technology (NTNU), Kolbjørn Hejes vei 2, NO-7491 Trondheim, Norway

[2]Sportradar AS, Ferjemannsveien 10, NO-7014 Trondheim, Norway

[*] E-mail: mohammadtaghi.khalili@ntnu.no
[†] E-mail: m.larsson@sportradar.com
[‡] E-mail: bernhard.muller@ntnu.no

ABSTRACT

A ghost-point immersed boundary method is devised for the compressible Navier–Stokes equations by employing high order summation-by-parts (SBP) difference operators. The immersed boundaries are treated as sharp interfaces by enforcing the solid wall boundary conditions via flow variables at ghost points using bilinearly interpolated flow variables at mirror points. The approach is verified and validated for compressible flow past a circular cylinder at moderate Reynolds numbers.

Keywords: High order finite difference method, Immersed boundary method, Compressible viscous flow .

NOMENCLATURE

Greek Symbols

ρ	Mass density
μ	Dynamic viscosity
τ	Viscous stress tensor
γ	Ratio of specific heats
κ	Heat conduction coefficient
ϕ	Generic variable
$\mathcal{G}$	Set of body intercept points that are part of the interpolation stencil
Λ	Parameter
σ	Source term in steady state heat equation
ξ, η	Transformed coordinates in computational domain

Latin Symbols

t	Physical time
E	Specific total energy
H	Total entalpy
p	Pressure
S_c	Sutherland constant
T	Temperature
$\mathbf{U}$	Vector of conservative variables
$\mathbf{V}$	Vandermonde matrix
x, y	Cartesian coordinates in physical domain
J^{-1}	Jacobian determinant

Sub/superscripts

GP	Ghost point
IP	Image point
BI	Body intercept
c'	Conservative perturbation
ν'	Viscous perturbation

INTRODUCTION

Many applications in engineering, biology and medicine involve low and moderate Reynolds number flow problems with complex boundaries between fluid and structure. Simulating these problems with conventional methods requires the process of generating high quality and body-conforming grids which is challenging and time-consuming. Recently, there has been a growing interest in the development of non-boundary conforming methodologies for the solution of the Navier–Stokes equations (Mittal and Iaccarino, 2005). In such methods, the requirement that the grid should conform to a solid boundary is dropped, and the effect of the immersed boundary of the solid body on the flow is introduced through the proper treatment of the solution variables near the boundary. The basic advantage of these formulations is the simplicity compared with conventional body-conforming grid generation, especially in cases of complex stationary or moving boundaries where the demand for regeneration or deformation of the grid is eliminated. Therefore, efficient non boundary conforming strategies with robust Cartesian coordinate solvers can directly be applied to a wide range of flow problems.

Over the past decades a variety of non-body conforming approaches with various degrees of accuracy and complexity have been proposed. The so-called immersed-boundary method (IBM) was introduced by (Peskin, 1972). IB methods are categorized into continuous forcing and discrete (direct) forcing approaches. In the first category, a continuous forcing term is added to the governing equations to represent the interaction between the immersed boundary and the fluid, and a discrete Dirac–delta function is used to smooth this singular force on the Euler grid (Peskin, 1972; Goldstein *et al.*, 1993; Saiki and Biringen, 1996). Numerous modifications and improvements have been implemented in this category (Haeri and Shrimpton, 2012; Sotiropoulos and Yang, 2014). The second category, including the sharp interface method, mimics the presence of a surface force exerted by the boundary on the fluid by adjusting the discretization in the vicinity of the immersed boundary in order to directly take into account the boundary conditions at the IB (Ye *et al.*, 1999; Fadlun *et al.*, 2000; Mohd-Yusof, 1997; Balaras, 2004). The ghost cell immersed boundary (GCIB) method as sharp interface method is proposed in the studies by (Tseng and Ferziger, 2003; Ghias *et al.*, 2007; Mittal *et al.*, 2008). Ghost cells are defined as a layer of cells within the solid body having at least one nearby point in the fluid domain

i.e., adjoining to the immersed boundary. The flow variables at the ghost points are calculated with the boundary conditions at the immersed boundary and the flow variables at grid points near the IB in the fluid domain. The presence of the immersed boundary is introduced by the flow variables at the ghost points. The idea of image points inside the fluid domain is adopted to ensure suitable weighting coefficients in the reconstruction formula in order to avoid numerical instability caused by the large, negative weighting coefficients in the extrapolation formulation (Tseng and Ferziger, 2003). The ghost point method has shown large potential to deal with different fluid-solid interaction problems, including those involving highly complex geometries and moving or deforming bodies (Mittal *et al.*, 2008).

In the IBM, all the equations can be solved on a body nonconformal, Cartesian grid which does not require to be updated for moving or deforming bodies. Due to the flexibility of the method, many different types of IBM have been developed in incompressible and compressible flow solvers. However, most of the attention on IBM is devoted to incompressible flows (Mittal and Iaccarino, 2005). Works on viscous compressible flows are still scarce and a few IBM for viscous compressible flows has been developed (De Palma *et al.*, 2006; Ghias *et al.*, 2007; de Tullio *et al.*, 2007; Brehm *et al.*, 2015). Due to the different nature of the Navier–Stokes equations for compressible and incompressible flows, i.e. the requirement of equation of state for compressible flows, there are differences in implementation of the boundary conditions between these two types of equations as well as in the spatial discretisation schemes employed.

In this study, the ghost point IB approach has been adopted for a high order finite difference method based on summation-by-parts operators (SBP) to provide an accurate and efficient approach for studying low Mach number compressible viscous flows. The major ambition of the present work is to extend this approach for fluid structure interaction (FSI) in the upper airways to study the obstructive sleep apnea syndrome. The main focus in our study is subsonic flow which permits us to characterize the acoustic wave propagation induced by the structure oscillation in FSI to obtain a better understanding of snoring. The proposed approach is verified and validated for two dimensional flows over a circular cylinder. In the following sections, a brief review of the governing equations and their numerical solution is given. Then, the IB approach is described in detail. Finally, results are provided and compared with numerical and experimental ones available in the literature.

MODEL DESCRIPTION

Governing equations

The 2D compressible Navier–Stokes equations in perturbation form are solved. To minimize cancellation errors when discretizing the Navier–Stokes equations for compressible low Mach number flow, the perturbation formulation is employed (Sesterhenn *et al.*, 1999; Müller, 2008). The conservative form of the 2D compressible Navier–Stokes equations in perturbation formulation can be written as

$$\mathbf{U}'_t + \mathbf{F}^{c\prime}{}_x + \mathbf{G}^{c\prime}{}_y = \mathbf{F}^{v\prime}{}_x + \mathbf{G}^{v\prime}{}_y \tag{1}$$

where $\mathbf{U}' = \mathbf{U} - \mathbf{U_0}$ is the vector of conservative perturbation variables with $\mathbf{U} = (\rho, \rho u, \rho v, \rho E)^T$ the vector of the conservative variables and $\mathbf{U}_0 = (\rho_0, 0, 0, (\rho E)_0)^T$ the stagnation values.

The conservative perturbation variables $\mathbf{U}'$ and the inviscid ($\mathbf{F}^{c\prime}$, $\mathbf{G}^{c\prime}$) and viscous perturbation flux vectors ($\mathbf{F}^{v\prime}$, $\mathbf{G}^{v\prime}$) are defined by $\mathbf{F}^{c\prime} = \mathbf{F}^c(\mathbf{U}) - \mathbf{F}^c(\mathbf{U_0})$, etc.

$$\mathbf{U}' = \begin{pmatrix} \rho' \\ (\rho u)' \\ (\rho v)' \\ (\rho E)' \end{pmatrix},$$

$$\mathbf{F}^{c\prime} = \begin{pmatrix} (\rho u)' \\ (\rho u)'u' + p' \\ (\rho v)'u' \\ ((\rho H)_0 + (\rho H)')u' \end{pmatrix}, \mathbf{G}^{c\prime} = \begin{pmatrix} (\rho v)' \\ (\rho u)'v' \\ (\rho v)'v' + p' \\ ((\rho H)_0 + (\rho H)')v' \end{pmatrix},$$

$$\mathbf{F}^{v\prime} = \begin{pmatrix} 0 \\ \tau'_{xx} \\ \tau'_{xy} \\ u'\tau'_{xx} + v'\tau'_{xy} + \kappa T'_x \end{pmatrix}, \mathbf{G}^{v\prime} = \begin{pmatrix} 0 \\ \tau'_{yx} \\ \tau'_{yy} \\ u'\tau'_{yx} + v'\tau'_{yy} + \kappa T'_y \end{pmatrix},$$

where t is physical time and x and y are the Cartesian coordinates. ρ denotes density, u and v the x- and y-direction velocity components, E the specific total energy, T the temperature and κ the heat conduction coefficient calculated from the constant Prandtl number $\mathrm{Pr} = 0.72$. ρ_0, $(\rho E)_0$ and $(\rho H)_0$ denote the stagnation values of density, total energy density and total enthalpy density. The perturbation variables are defined as:

$$\rho' = \rho - \rho_0, \quad (\rho\mathbf{u})' = (\rho\mathbf{u}),$$

$$(\rho E)' = \rho E - (\rho E)_0, \quad (\rho H)' = (\rho E)' + p', \quad \mathbf{u}' = \frac{(\rho\mathbf{u})'}{\rho_0 + \rho'},$$

$$\tau' = \mu(\nabla\mathbf{u}' + (\nabla\mathbf{u}')^T) - \frac{2}{3}\mu(\nabla\cdot\mathbf{u}')\mathbf{I}, \quad T' = \frac{p'/R - \rho' T_0}{\rho_0 + \rho'}$$

Here, R is the specific gas constant and μ is the viscosity which is determined from the Sutherland law $\frac{\mu}{\mu_0} = (\frac{T}{T_0})^{1.5}[(1+S_c)/(\frac{T}{T_0}+S_c)]$ with the non-dimensional Sutherland constant $S_c = \frac{110}{301.75}$.

Since perfect gas is considered, the pressure perturbation can be related to the conservative perturbation variables by $p' = (\gamma-1)[(\rho E)' - \frac{1}{2}((\rho\mathbf{u}'\cdot\mathbf{u}'))]$, where the ratio of specific heats $\gamma = c_p/c_v = 1.4$ for air.

The viscous flux vectors $\mathbf{F}^{v\prime}$ and $\mathbf{G}^{v\prime}$ are the same as for the standard conservative form, except for using the temperature perturbation T' instead of temperature T for the heat flux terms. The momentum density and velocity perturbations are taken as the same as their unperturbed counterparts, i.e. $(\rho\mathbf{u})' = \rho\mathbf{u}$ (Larsson and Müller, 2009). For convenience the variables are non-dimensionalized with ρ_0, stagnation speed of sound c_0 and $\rho_0 c_0^2$ as reference values. In order to generalize the geometry for non-uniform Cartesian grids, the equations of motions are transformed from the physical domain (x,y) to the computational domain (ξ,η) by the following relations,

$$\begin{aligned} x &= x(\xi,\eta) \\ y &= y(\xi,\eta) \end{aligned} \tag{2}$$

Thus, the transformed 2D compressible Navier–Stokes equations in perturbation form are expressed as:

$$\hat{\mathbf{U}}'_t + \hat{\mathbf{F}}'_\xi + \hat{\mathbf{G}}'_\eta = 0 \tag{3}$$

where $\hat{\mathbf{U}}' = J^{-1}\mathbf{U}'$, $\hat{\mathbf{F}}' = J^{-1}(\xi_x(\mathbf{F}^{c\prime} - \mathbf{F}^{v\prime}) + \xi_y(\mathbf{G}^{c\prime} - \mathbf{G}^{v\prime}))$ and $\hat{\mathbf{G}}' = J^{-1}(\eta_x(\mathbf{F}^{c\prime} - \mathbf{F}^{v\prime}) + \eta_y(\mathbf{G}^{c\prime} - \mathbf{G}^{v\prime}))$. The chain rule for partial differentiation provides the expressions for Cartesian derivatives in the viscous flux vectors $\mathbf{F}^{v\prime}$ and $\mathbf{G}^{v\prime}$, e.g.

$u'_x = u'_\xi \xi_x + u'_\eta \eta_x$ and $u'_y = u'_\xi \xi_y + u'_\eta \eta_y$. The Jacobian determinant of the transformation is $J^{-1} = x_\xi y_\eta - x_\eta y_\xi$ and metric terms are

$$\begin{aligned} J^{-1}\xi_x &= y_\eta, \quad J^{-1}\xi_y = -x_\eta, \\ J^{-1}\eta_x &= -y_\xi, \quad J^{-1}\eta_y = x_\xi. \end{aligned} \tag{4}$$

Numerical methodology

The summation-by-parts (SBP) operator Q is an approximation to the first ξ- and η- derivatives in (4) and (3). In the interior, it corresponds to the standard sixth order central operator, while being third order accurate near the boundaries. Through a special boundary treatment, SBP operators permit energy estimates for discrete problems similar to those for the continuous ones that are approximated. Therefore, SBP operators can yield strictly stable schemes for general boundary conditions (Strand, 1994; Gustafsson *et al.*, 1995; Gustafsson, 2008). The global order of accuracy of the present SBP operator Q is fourth order (Müller, 2008). The energy method and the summation-by-parts operators are discussed in the Appendix A and B, respectively.

Second derivatives of viscous parts of $\hat{\mathbf{F}}_\xi{}'$ and $\hat{\mathbf{G}}_\eta{}'$ are approximated by applying the SBP operator for first derivatives twice. However, successively applying the first derivative operator makes the scheme wider, which requires special treatment for the immersed boundary method, and will be discussed in section boundary conditions below. Spurious high wave number oscillations are suppressed by a sixth order explicit filter (Visbal and Gaitonde, 2002; Müller, 2008). The classical fourth order explicit Runge–Kutta method is employed for time integration.

Immersed boundary formulation

The sharp interface method is well suited for compressible viscous flow, due to imposing the boundary conditions at immersed boundaries, without computing any forcing term and introducing any force distribution function. The ghost point immersed boundary method employed in this study is based on the ghost cell immersed boundary approach for second order methods (Ghias *et al.*, 2007; Mittal *et al.*, 2008).

The basic idea in this method is to compute the value of the flow variables at each of the ghost points (referring to the layer of points inside the solid body adjoining the immersed boundary) such that the boundary conditions at the immersed boundary are satisfied. As illustrated in Fig. 1, the procedure begins by determining the immersed boundary and then distinguishing the solid points, i.e. the nodes lying inside the solid body, and the fluid points, i.e. the nodes lying outside the body in the fluid domain. The ghost points (denoted by GP) are identified by those nodes that lie inside the body and adjacent to the immersed boundary which have at least one neighbour node in the fluid domain with the difference stencil centered at the ghost point. The image point (denoted by IP) can be found by extending a normal probe, i.e. a line normal to the immersed boundary, from the ghost point to intersect with the immersed boundary at the body intercept point (denoted by BI) such that the body intercept point lies at the midpoint of the line connecting the ghost point and the image point. Once the flow variables at the image point are computed, the ghost point variables can be determined by imposing the boundary conditions. In other words, the general strategy is to compute the flow variables at the image point by taking into account the nodal values at the surrounding fluid points and then use the boundary conditions to obtain the values at the ghost point.

Among the available options for determining the flow variables at the image points, the computationally most efficient scheme will be the bilinear interpolation scheme in 2D (Ghias *et al.*, 2007; Mittal *et al.*, 2008) where the flow variables are linearly interpolated from four nodal points surrounding the image points. This interpolation scheme leads to a nominally second order accuracy of the immersed boundary condition. The high order SBP operator used in this study for spatial discretization, corresponding to the sixth order central finite difference method at interior grids, requires three layers of ghost points inside the immersed boundary in order to maintain the overall high order of accuracy, as shown in Fig. 2.

In the case of bilinear interpolation, the interpolating polynomial involves four nodes and hence four nodal values need to be specified. The bilinear interpolation for a generic variable ϕ can be expressed as

$$\phi(x,y) = C_1 + C_2 x + C_3 y + C_4 xy. \tag{5}$$

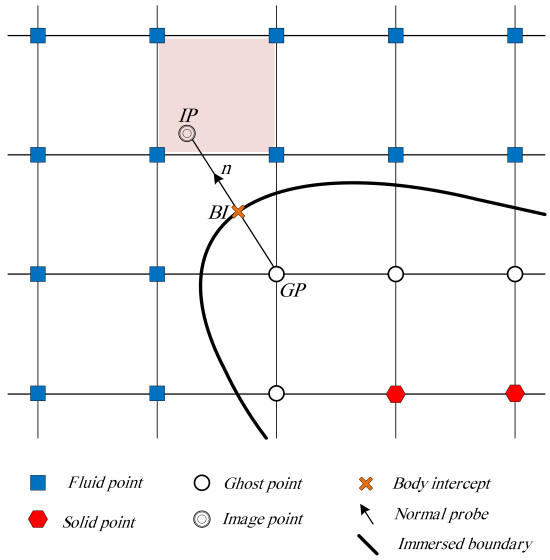

Figure 1: Schematic of points used to interpolate the variable located at a ghost point.

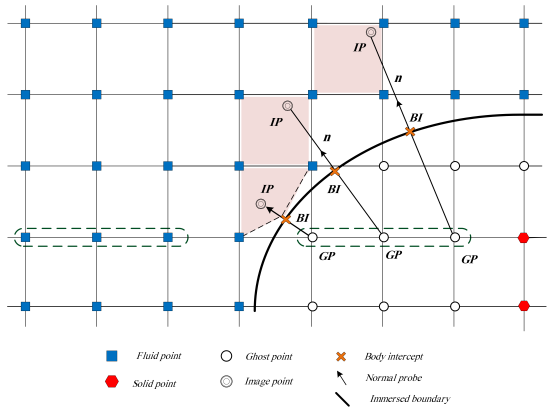

Figure 2: Schematic of 3 layers of ghost points inside immersed body on a Cartesian mesh.

The four unknown coefficients $C_i, i = 1,..,4$, can be determined using values at the four nodes surrounding the image point. Thus, the variable at the image point is reconstructed through bilinear interpolation using unknown coefficients and known flow variables at surrounding fluid nodes. The four weighting coefficients are evaluated as the solution of the linear system

$$\mathbf{VC} = \phi, \tag{6}$$

where

$$\mathbf{C} = \{C_1, C_2, C_3, C_4\}^T \tag{7}$$

is the vector of the unknown coefficients and

$$\phi = \{\phi_1, \phi_2, \phi_3, \phi_4\}^T \tag{8}$$

is the vector of the four surrounding node values. The matrix $\mathbf{V}$ is the Vandermonde matrix which is expressed as

$$\mathbf{V} = \begin{bmatrix} 1 & x_1 & y_1 & x_1 y_1 \\ 1 & x_2 & y_2 & x_2 y_2 \\ 1 & x_3 & y_3 & x_3 y_3 \\ 1 & x_4 & y_4 & x_4 y_4 \end{bmatrix} \tag{9}$$

In this classical formulation, the unknown coefficient values $C_i, i = 1,...,4$, would depend on the solution at each time step. However, the approach can be reformulated such that new coefficients are only dependent on the coordinates of the image point and the geometry of the grids. The reformulation is discussed in detail in Appendix C. Thus, the image point value can be expressed as

$$\phi_{IP} = \sum_{i=1}^{4} \alpha_i \phi_i \tag{10}$$

where $\alpha_i, i = 1,...,4$, are coefficients depending on the coordinates only. They can be established once the grid, immersed boundary and image point coordinates are specified.
When a ghost point is close to the immersed boundary, its corresponding image point might not have four surrounding fluid points. One case would be that the ghost point itself is part of the interpolation scheme. Since the ghost point value in an interpolation scheme would be unknown, the ghost point is then replaced by the body intercept point where the values are determined by the boundary conditions, cf. Fig. 3.
For Dirichlet boundary condition in this case, the corresponding row in Eq. (9) is replaced by

$$\phi_{BI}(x,y) = C_1 + C_2\, x_{BI} + C_3\, y_{BI} + C_4\, x_{BI} y_{BI} \tag{11}$$

where x_{BI} and y_{BI} are the coordinates of the body intercept point. Thereby, for a Dirichlet boundary condition the linear system corresponding to Eq.(6) for this case becomes

$$\begin{bmatrix} 1 & x_1 & y_1 & x_1 y_1 \\ 1 & x_2 & y_2 & x_2 y_2 \\ 1 & x_3 & y_3 & x_3 y_3 \\ 1 & x_B & y_B & x_B y_B \end{bmatrix} \begin{bmatrix} C_1 \\ C_2 \\ C_3 \\ C_4 \end{bmatrix} = \begin{bmatrix} \phi_1 \\ \phi_2 \\ \phi_3 \\ \phi_{BI} \end{bmatrix} \tag{12}$$

For a Neumann boundary condition, the variable gradient at the body intercept is known instead of the actual value. The most obvious choice in such a case is to use the specified gradient value $\frac{\partial \phi_{\mathrm{BI}}}{\partial n}$ to compute the value at the image point. The gradient of ϕ_{BI} at the boundary can be determined by taking the normal derivative of Eq.(11),

$$\frac{\partial \phi_{\mathrm{BI}}}{\partial n} = C_2 n_x + C_3 n_y + C_4 (y_{\mathrm{BI}} n_x + x_{\mathrm{BI}} n_y) = \zeta \tag{13}$$

where n_x and n_y are the components of the unit vector normal to the boundary.
Thus, the linear system corresponding to Eq.(6) for this case becomes

$$\begin{bmatrix} 1 & x_1 & y_1 & x_1 y_1 \\ 1 & x_2 & y_2 & x_2 y_2 \\ 1 & x_3 & y_3 & x_3 y_3 \\ 0 & n_x & n_y & y_{BI} n_x + x_{BI} n_y \end{bmatrix} \begin{bmatrix} C_1 \\ C_2 \\ C_3 \\ C_4 \end{bmatrix} = \begin{bmatrix} \phi_1 \\ \phi_2 \\ \phi_3 \\ \zeta \end{bmatrix} \tag{14}$$

As shown in Fig. 4, it might also be the case that two interpolation points would lie inside the immersed body, one at the corresponding ghost point itself and one at another ghost point. The procedure we used to handle this case is to repeat the above steps for the other ghost point as well, resulting in a Vandermonde matrix where another row is also replaced by Eqs. (11) or (13) in the same way as the fourth row, in contrast to (Ghias *et al.*, 2007; Mittal *et al.*, 2008). Applying our procedure for this case, it is no longer necessary to solve a coupled linear system by using iterative processes like (Ghias *et al.*, 2007; Mittal *et al.*, 2008). This situation does not pose any consistency issues and ensures that the interpolation procedure for the image point is well-posed without affecting the accuracy of the interpolation.
The value of the variable at the ghost point is computed by employing a linear approximation along the normal probe which takes into account the boundary condition at the boundary intercept. For a Dirichlet boundary condition this can generally be expressed as

$$\phi_{\mathrm{BI}} = \tfrac{1}{2}(\phi_{\mathrm{IP}} + \phi_{\mathrm{GP}}) + O(\triangle l^2) \tag{15}$$

where $\triangle l$ is the length of the normal probe from GP to IP. Solving for ϕ_{GP} using Eq. (15) and neglecting the truncation gives

$$\phi_{\mathrm{GP}} = \left(2 - \sum_{j \in \mathcal{G}} \alpha_j\right) \phi_{\mathrm{BI}} - \sum_{i \notin \mathcal{G}} \alpha_i \phi_i \tag{16}$$

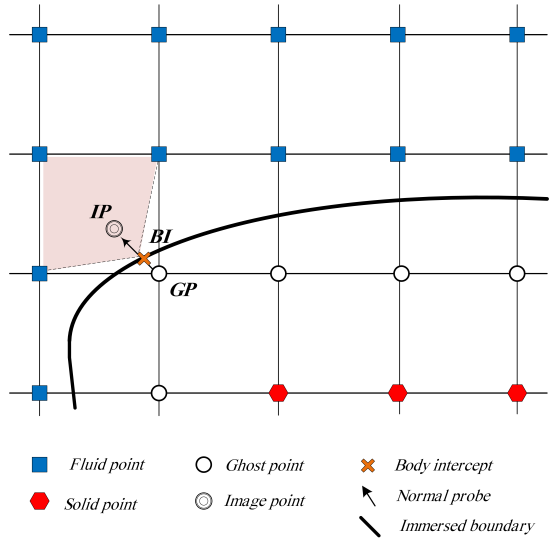

Figure 3: Schematic of the situation when one surrounding interpolation point is the boundary intercept.

where $\mathcal{G}$ is the set of body intercepts that are part of the interpolation stencil. For a Neumann boundary condition on the immersed boundary, the following second-order central-difference is written along the normal probe

$$(\frac{\partial \phi}{\partial n})_{\mathrm{BI}} = \frac{\phi_{\mathrm{IP}} - \phi_{\mathrm{GP}}}{\triangle l} + O(\triangle l^2) \tag{17}$$

Thereby, the general formulation for a non-homogeneous Neumann boundary condition is expressed as

$$\phi_{\mathrm{GP}} = \left(\sum_{j \in \mathcal{G}} \alpha_j - \triangle l \right) (\frac{\partial \phi}{\partial n})_{\mathrm{BI}} + \sum_{i \notin \mathcal{G}} \alpha_i \phi_i \tag{18}$$

Boundary conditions

The no-slip boundary condition at the immersed boundary for a stationary body is considered. Thereby, Dirichlet boundary conditions are employed for the velocity components at the IB. For each velocity components, the corresponding value at the body intercept $\phi_{BI} = 0$ is set in Eq. (11). Applying the no-slip condition at the body surface, the convective flux contribution should be zero. The pressure gradient normal to the immersed interface is set zero as a boundary layer approximation, $\frac{\partial p}{\partial n} = \frac{\partial \phi_{\mathrm{BI}}}{\partial n} = 0$ in Eq. (13). The boundary condition for the temperature depends on the whether the immersed surface of the body is adiabatic or isothermal. Assuming an adiabatic boundary condition at the immersed body, the temperature gradient normal to the surface $\frac{\partial T}{\partial n} = 0$ is set to zero by enforcing a zero density gradient $\frac{\partial \rho}{\partial n} = 0$. Thus, for the variables ρ and p Neumann boundary conditions are employed. According to the boundary conditions considered for the immersed body, the values of the conservative perturbation variables at the ghost points are determined once the flow variables at the image points

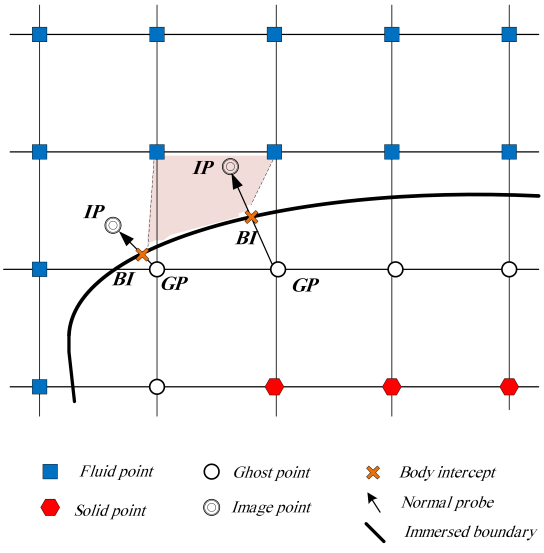

Figure 4: Schematic of the situation when two of the surrounding interpolation points lie inside the immersed body.

are interpolated using:

$$\begin{aligned} \rho'_{GP} &= \rho'_{IP} \\ (\rho u)'_{GP} &= -(\rho u)'_{IP} \\ (\rho v)'_{GP} &= -(\rho v)'_{IP} \\ (\rho E)'_{GP} &= (\rho E)'_{IP} \end{aligned} \tag{19}$$

As mentioned above, applying the first derivative approximation twice for computing the second derivative will make the stencil wider. For the proper treatment of wide stencils in computing the second derivative, the first derivatives of the viscous terms are computed up to and including the ghost points, treating the solid points inside the ghost point layers as domain boundaries when employing the differencing stencil. Using this procedure, we ensure that the derivatives of the viscous fluxes at the fluid points closest to the immersed boundary are computed with high order.

Non-reflecting characteristic boundary conditions are employed at the inflow and outflow boundaries to minimize wave reflections. The Navier–Stokes characteristic boundary conditions (NSCBC) developed by (Poinsot and Lele, 1992) are employed to approximate incoming waves based on local one-dimensional inviscid (LODI) relations. The primitive variables can be related to the wave amplitude ($\mathscr{L}_i$) by LODI relations. The amplitudes of the characteristic waves are $\mathscr{L}_1 = \lambda_1(\frac{\partial p}{\partial x} - \rho c \frac{\partial u}{\partial x})$, $\mathscr{L}_2 = \lambda_2(c^2 \frac{\partial \rho}{\partial x} - \frac{\partial p}{\partial x})$, $\mathscr{L}_3 = \lambda_3(\frac{\partial v}{\partial x})$ and $\mathscr{L}_4 = \lambda_4(\frac{\partial p}{\partial x} + \rho c \frac{\partial u}{\partial x})$. Since fully non-reflecting conditions may lead to an ill-posed problem (Poinsot and Lele, 1992), this approach is partially reflecting. Imposing a constant pressure at the outlet requires $\mathscr{L}_1 = -\mathscr{L}_4$. To keep the reflections low and the pressure close to atmospheric pressure, the incoming wave amplitude is set to

$$\mathscr{L}_1 = K(p - p_{\mathrm{atm}}) \tag{20}$$

where K is a relaxation coefficient. Rudy and Strikwerda proposed the relaxation coefficient as $K = \Lambda(1 - \mathrm{Ma}^2)(c/L_t)$ where Ma is the Mach number, c the speed of sound, L_t the total length of the domain and Λ a parameter (Rudy and Strikwerda, 1980). The optimum value $\Lambda = 0.25$ derived by (Rudy and Strikwerda, 1980) is employed. For reverse flow (negative velocity in x-direction) at the outlet, $\mathscr{L}_1$, $\mathscr{L}_2$ and $\mathscr{L}_3$ are set to zero. A similar boundary treatment at inflow and outflow was used by (Khalili *et al.*, 2016).

RESULTS

In order to assess the accuracy of the immersed boundary methodology, a two-dimensional steady state heat problem is first solved. Then, the IBM is applied to a two-dimensional flow past a circular cylinder at a range Reynolds numbers to demonstrate the ability and performance of the method for simulating compressible viscous flow.

Steady state heat equation

To verify the order of spatial accuracy of the current immersed boundary scheme, a steady state heat transfer problem has been considered. Since the ghost point immersed boundary method is second-order accurate (Ghias *et al.*, 2007; Mittal *et al.*, 2008), care has been taken to maintain a second-order spatial accuracy in the imposition of boundary conditions on the immersed boundary. The steady state heat equation reads

$$\nabla^2 T = \sigma \tag{21}$$

where σ is a source term, i.e. $-\kappa\sigma$ is the rate of heat generation per unit volume. The exact solution for this case in polar coordinates can be expressed as

$$T(r) = \sigma \frac{r^2}{4} + A \ln(r) + B \tag{22}$$

where A and B depend on the boundary conditions type and their values.

The numerical solution by means of IBM is implemented to solve Eq.(21) in Cartesian coordinates. The second and fourth order central finite difference methods for second derivatives are employed for spatial discretization of the regular fluid points.

$$T_{xx}^{(2)} = (T_{i+1} - 2T_i + T_{i-1})/\Delta x^2 \tag{23}$$

$$T_{xx}^{(4)} = (-T_{i+2} + 16T_{i+1} - 30T_i + 16T_{i-1} - T_{i-2})/(12\Delta x^2) \tag{24}$$

The temperature distribution is solved between two concentrical cylinders with inner and outer diameters $D_{\text{inner}} = 3.5$ and $D_{\text{outer}} = 8.5$, respectively, embedded in a square domain of edge length $L = 10$. The $\sigma = -0.45$ is chosen and the temperatures of the inner and outer cylinders are $T_{\text{inner}} = 5$ and $T_{\text{outer}} = 10$, respectively. The immersed boundary approach is implemented at the cylinder interfaces. The results from different grids on a uniform Cartesian grid $(N \times N)$ from $N = 100$ to 1000 are compared with the exact solution to compute the L_2 and L_∞ norms. Fig. 5 shows the errors for different grids.

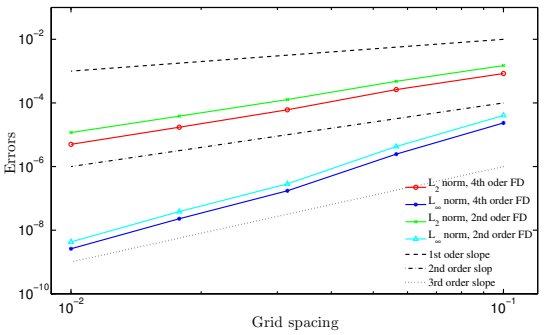

Figure 5: L_2 and L_∞ norms computed at various grid levels with IBM for 2D steady heat Eq. (21).

The first, second and third–order convergence rates are also included in Fig. 5 for reference. This figure indicates that a second-order rate of convergence has been achieved by the Poisson solver for Dirichlet boundary conditions at immersed boundaries. The error are slightly lower for the fourth order difference method than for the second order one.

Flow past circular cylinder

To verify and validate the present immersed boundary treatment for a compressible flow solver, the benchmark flow over a circular cylinder is firstly simulated at the Reynolds numbers of 20 and 40 based on the free-stream velocity and diameter of the cylinder. It is known that steady flow over a circular cylinder can persist up to Reynolds numbers of about 40. The free-stream Mach number for the simulation is set as a small number $\text{Ma} = 0.03$ in order to be comparable to the simulations performed using incompressible solvers. Then, the unsteady flow over a circular cylinder has been chosen to verify the proposed IB method at the Reynolds number of 100 and Mach number 0.25.

The computational domain size is $90D \times 40D$ where D is the diameter of the cylinder. The center of the cylinder is located at the point $(20D, 20D)$ of the coordinate system. The computational domain is sizeable to reduce the effects of domain boundaries and wave reflections form the inlet and outlet boundaries. It has been observed that those could lead to a momentous error when computing the lift and drag coefficients. In the present work, the block structured computational domain has been discretized with non-uniform Cartesian grids, where the block corresponding to the cylinder has a much finer grid spacing of $(\Delta x = \Delta y = D/25)$ at Re = 20 and 40, and grid spacing of $(\Delta x = \Delta y = D/50)$ at Re = 100. At these grid resolutions, the lift and drag coefficients are sufficiently converged. Sufficient grid resolution around the cylinder is crucial to obtain the drag and lift coefficients accurately. Additionally, to capture the von Kármán vortex shedding, the wake region needs to be resolved properly. The grid spacing Δx and Δy was smoothly stretched from $(\Delta x = \Delta y = D/25$ at Re = 20 and 40, and $\Delta x = \Delta y = D/50$ for Re=100 to $\Delta x = \Delta y = D/2$ near the inflow, outflow, top and bottom boundaries. Symmetry boundary conditions are applied on the top and bottom of the computational domain. At the inflow, the velocities in the x- and y-directions are imposed using a uniform inlet profile normal to the boundary, $u(x = 0, t) = U_\infty$ and $v = 0$. In addition, the inlet temperature is set to $T = T_0 = 310$ K. The outlet pressure is set to atmospheric pressure, i.e., $p' = p - p_0 = p - p_{\text{atm}} = 0$ Pa.

The drag and lift coefficients are defined as $C_D = \frac{F_D}{\frac{1}{2}\rho_\infty U_\infty^2 D}$ and $C_L = \frac{F_L}{\frac{1}{2}\rho_\infty U_\infty^2 D}$, respectively, where F_D and F_L are the drag and lift forces. The total force on the cylinder is given by the sum of the pressure and viscous force integrated over the cylinder surface $F = -\oint p_B \cdot \mathbf{n}\, ds + \oint \tau_B \cdot \mathbf{n}\, ds$ where $\mathbf{n}$ is the outer unit vector normal to the cylinder, and p_B and τ_B are pressure and the viscous stress tensor on the body surface, respectively. These quantities are based on the evaluation of surface pressure and viscous stress. The procedure used to compute these surface quantities needs some explanation. In the current solver, four nodes surrounding a body-intercept point corresponding to the first layer of ghost points are identified and then a bilinear interpolation is used to estimate the pressure and viscous stress tensor at the body intercept. The viscous stress at the involved ghost points and fluid points are computed in a straightforward manner by using our high order method.

Figs. 6 - 9 show streamlines and vorticity contours for $\text{Re} = 20$ and $\text{Re} = 40$, respectively. The geometrical properties of the vortices behind the cylinder are schematically illustrated in Fig. 10 (Canuto and Taira, 2015). The quantitative comparison of these parameters as well as the drag coefficient with available numerical and experimental results are given in Table 1.

Fig. 11 presents the instantaneous spanwise vorticity ω_z contours for Re = 100 indicating the presence of the von Kármán vortex street. The vortex shedding leads to time-varying lift and drag forces until they reach to a periodic oscillatory form. The Strouhal number $St = \frac{fD}{U_\infty}$, where f is the vortex sheding frequency, is computed from the temporal variation of the lift coefficient. Due to the unsteadiness of the flow, the comparison of the average values of the lift and drag coefficients as well as the amplitude of the sinusoidal variation in time of the lift and drag coefficients is central. The results for the time-averaged lift and drag coefficients, the amplitude of

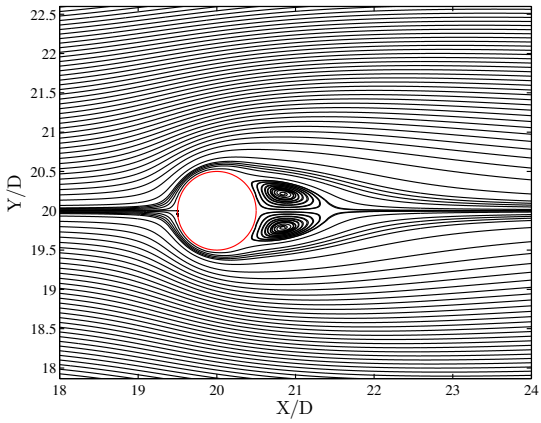

Figure 6: Streamlines for computed flow past a circular cylinder at Re = 20 and Ma = 0.03.

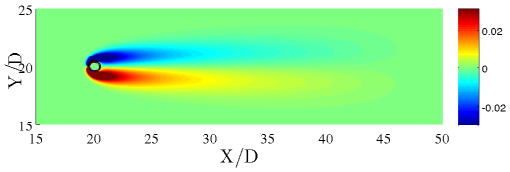

Figure 7: Vorticity contours for computed flow past a circular cylinder at Re = 20 and Ma = 0.03.

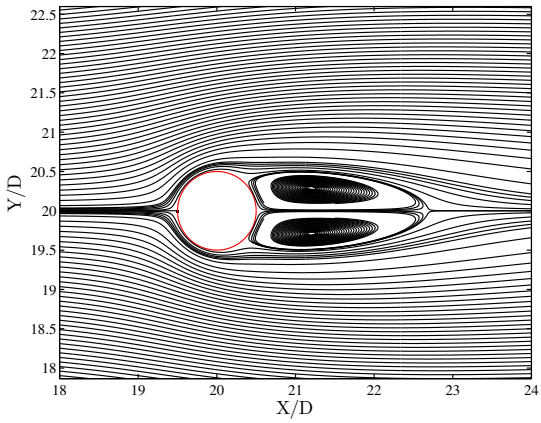

Figure 8: Streamlines for computed flow past a circular cylinder at Re = 40 and Ma = 0.03.

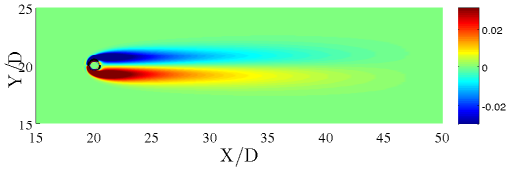

Figure 9: Vorticity contours for computed flow past a circular cylinder at Re = 40 and Ma = 0.03.

Table 1: Comparison of computed data with available numerical and experimental data at Re = 20 and Re = 40. (Exp.) indicates the experimental results.

Re = 20						
	Ma	L	a	b	$\theta(deg)$	C_D
(Tritton, 1959)(Exp.)	-	-	-	-	-	2.09
(Dennis and Chang, 1970)	0	0.94	-	-	43.7	2.05
(Coutanceau and Bouard, 1977)(Exp.)	-	0.93	0.33	0.46	45.0	-
(Fornberg, 1980)	0	0.91	-	-	45.7	2.0
(Linnick and Fasel, 2003)	0	0.93	0.36	0.43	43.5	2.06
(De Palma *et al.*, 2006)	0.03	0.93	0.36	0.43	44.6	2.05
(Canuto and Taira, 2015)	0	0.92	0.36	0.42	43.7	2.07
Present study	**0.03**	**0.93**	**0.36**	**0.43**	**43.9**	**2.05**
Re = 40						
	Ma	L	a	b	$\theta(deg)$	C_D
(Tritton, 1959)(Exp.)	-	-	-	-	-	1.59
(Dennis and Chang, 1970)	0	2.35	-	-	53.8	1.52
(Coutanceau and Bouard, 1977)(Exp.)	-	2.13	0.76	0.59	53.8	-
(Fornberg, 1980)	0	2.24	-	-	55.6	1.50
(Linnick and Fasel, 2003)	0	2.28	0.72	0.60	53.6	1.52
(De Palma *et al.*, 2006)	0.03	2.28	0.72	0.60	53.8	1.55
(Canuto and Taira, 2015)	0	2.24	0.72	0.59	53.7	1.54
Present study	**0.03**	**2.22**	**0.72**	**0.59**	**53.1**	**1.52**

their changes as well as the Strouhal number of the present study are compared to published results in Table 2. Table 1 and 2 confirm that for the present study all results compare very well with results reported in the literature.

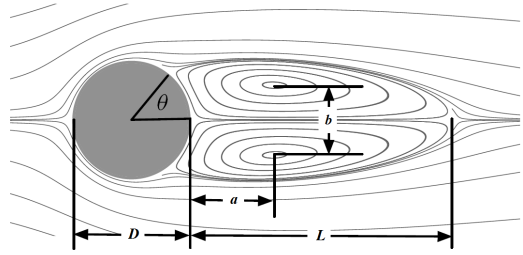

Figure 10: Definitions of the relevant geometrical parameters of the symmetric deperation region behind the cylinder (Canuto and Taira, 2015).

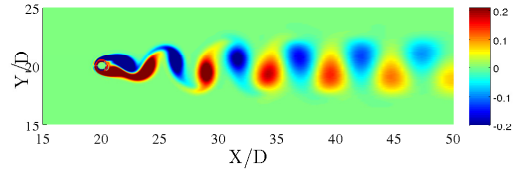

Figure 11: Vorticity contours for computed flow past a circular cylinder at Re = 100 and Ma = 0.25

Table 2: Comparison of computed data with available numerical and experimental data at Re = 100.

	Re = 100			
	Ma	*St*	C_D	C_L
(Berger and Wille, 1972)	0	0.16-0.17	-	-
(Liu *et al.*, 1998)	0	0.165	1.35 ± 0.012	± 0.339
(Linnick and Fasel, 2003)	0	0.166	1.34 ± 0.009	± 0.333
(Mittal *et al.*, 2008)	0	-	1.35	-
(Karagiozis *et al.*, 2010)	0.25	0.168	1.336	± 0.319
(Canuto and Taira, 2015)	0.25	0.163	1.378	± 0.325
Present study	**0.25**	**0.1667**	$\mathbf{1.33 \pm 0.013}$	$\mathbf{\pm 0.323}$

CONCLUSION

In this paper, we have combined highly stable high-order SBP operators with an immersed boundary method which permits us to use Cartesian grids for arbitrary geometries for solving the compressible Navier–Stokes equations accurately and efficiently. SBP operators which are 6^{th} order accurate in the interior and 3^{rd} order accurate near the boundaries is employed. To achieve high accuracy and easy parallelization, the 4^{th} order explicit Runge–Kutta method is applied. The methodology is applied to compute steady and unsteady flow problems to demonstrate its versatility as well as its accuracy. The flow past a circular cylinder for moderate values of Reynolds number and Mach number is assessed. A good agreement with available experimental and numerical results is achieved.

ACKNOWLEDGMENTS

The present research is a part of a research project entitled "Modeling of obstructive sleep apnea by fluid-structure interaction in the upper airways" funded by the Research Council of Norway. The simulations in our work are done on the Vilje cluster at NTNU which is gratefully acknowledged.

REFERENCES

BALARAS, E. (2004). "Modeling complex boundaries using an external force field on fixed Cartesian grids in large-eddy simulations". *Computers & Fluids*, **33(3)**, 375–404.

BERGER, E. and WILLE, R. (1972). "Periodic flow phenomena". *Annual Review of Fluid Mechanics*, **4(1)**, 313–340.

BREHM, C., HADER, C. and FASEL, H.F. (2015). "A locally stabilized immersed boundary method for the compressible navier–stokes equations". *Journal of Computational Physics*, **295**, 475–504.

CANUTO, D. and TAIRA, K. (2015). "Two-dimensional compressible viscous flow around a circular cylinder". *Journal of Fluid Mechanics*, **785**, 349–371.

COUTANCEAU, M. and BOUARD, R. (1977). "Experimental determination of the main features of the viscous flow in the wake of a circular cylinder in uniform translation. Part 1. Steady flow". *Journal of Fluid Mechanics*, **79(02)**, 231–256.

DE PALMA, P., DE TULLIO, M., PASCAZIO, G. and NAPOLITANO, M. (2006). "An immersed-boundary method for compressible viscous flows". *Computers & Fluids*, **35(7)**, 693–702.

DE TULLIO, M.D., DE PALMA, P., IACCARINO, G., PASCAZIO, G. and NAPOLITANO, M. (2007). "An immersed boundary method for compressible flows using local grid refinement". *Journal of Computational Physics*, **225(2)**, 2098–2117.

DENNIS, S. and CHANG, G.Z. (1970). "Numerical solutions for steady flow past a circular cylinder at Reynolds numbers up to 100". *Journal of Fluid Mechanics*, **42(03)**, 471–489.

FADLUN, E., VERZICCO, R., ORLANDI, P. and MOHD-YUSOF, J. (2000). "Combined immersed-boundary finite-difference methods for three-dimensional complex flow simulations". *Journal of Computational Physics*, **161(1)**, 35–60.

FORNBERG, B. (1980). "A numerical study of steady viscous flow past a circular cylinder". *Journal of Fluid Mechanics*, **98(04)**, 819–855.

GHIAS, R., MITTAL, R. and DONG, H. (2007). "A sharp interface immersed boundary method for compressible viscous flows". *Journal of Computational Physics*, **225(1)**, 528–553.

GOLDSTEIN, D., HANDLER, R. and SIROVICH, L. (1993). "Modeling a no-slip flow boundary with an external force field". *Journal of Computational Physics*, **105(2)**, 354–366.

GUSTAFSSON, B. (2008). *High order difference methods for time dependent PDE*. Springer, Berlin.

GUSTAFSSON, B., KREISS, H.O. and OLIGER, J. (1995). *Time dependent problems and difference methods*. John Wiley & Sons, New York.

HAERI, S. and SHRIMPTON, J. (2012). "On the application of immersed boundary, fictitious domain and body-conformal mesh methods to many particle multiphase flows". *International Journal of Multiphase Flow*, **40**, 38 – 55.

KARAGIOZIS, K., KAMAKOTI, R. and PANTANO, C. (2010). "A low numerical dissipation immersed interface method for the compressible navier–stokes equations". *Journal of Computational physics*, **229(3)**, 701–727.

KHALILI, M., LARSSON, M. and MÜLLER, B. (2016). "Interaction between a simplified soft palate and compressible viscous flow". *Journal of Fluids and Structures*, **67**, 85–105.

LARSSON, M. and MÜLLER, B. (2009). "Numerical simulation of confined pulsating jets in human phonation". *Computers & Fluids*, **38(7)**, 1375–1383.

LINNICK, M. and FASEL, H. (2003). "A high-order immersed boundary method for unsteady incompressible flow calculations". *41st Aerospace Sciences Meeting and Exhibit*, 1124.

LIU, C., ZHENG, X. and SUNG, C. (1998). "Preconditioned multigrid methods for unsteady incompressible flows". *Journal of Computational Physics*, **139(1)**, 35–57.

MITTAL, R. and IACCARINO, G. (2005). "Immersed boundary methods". *Annual Review of Fluid Mechanics*, **37**, 239–261.

MITTAL, R., DONG, H., BOZKURTTAS, M., NAJJAR, F., VARGAS, A. and VON LOEBBECKE, A. (2008). "A versatile sharp interface immersed boundary method for incompressible flows with complex boundaries". *Journal of Computational Physics*, **227(10)**, 4825–4852.

MOHD-YUSOF, J. (1997). "Combined immersed-boundary/B-spline methods for simulations of flow in complex geometries". *Center for Turbulence Research Annual Research Briefs*, 317–325.

MÜLLER, B. (2008). "High order numerical simulation of aeolian tones". *Computers & Fluids*, **37(4)**, 450–462.

PESKIN, C.S. (1972). "Flow patterns around heart valves: A numerical method". *Journal of Computational Physics*, **10(2)**, 252–271.

POINSOT, T.J. and LELE, S. (1992). "Boundary conditions for direct simulations of compressible viscous flows". *Journal of Computational Physics*, **101(1)**, 104–129.

RUDY, D.H. and STRIKWERDA, J.C. (1980). "A non-reflecting outflow boundary condition for subsonic Navier-Stokes calculations". *Journal of Computational Physics*, **36(1)**, 55–70.

SAIKI, E. and BIRINGEN, S. (1996). "Numerical simulation of a cylinder in uniform flow: Application of a virtual boundary method". *Journal of Computational Physics*, **123(2)**, 450–465.

SESTERHENN, J., MÜLLER, B. and THOMANN, H. (1999). "On the cancellation problem in calculating compressible low Mach number flows". *Journal of Computational Physics*, **151(2)**, 597–615.

SOTIROPOULOS, F. and YANG, X. (2014). "Immersed boundary methods for simulating fluid-structure interaction". *Progress in Aerospace Sciences*, **65**, 1 – 21.

STRAND, B. (1994). "Summation by parts for finite difference approximations for d/dx". *Journal of Computational Physics*, **110(1)**, 47–67.

SVÄRD, M. and NORDSTRÖM, J. (2014). "Review of summation-by-parts schemes for initial–boundary-value problems". *Journal of Computational Physics*, **268**, 17–38.

TRITTON, D. (1959). "Experiments on the flow past a circular cylinder at low Reynolds numbers". *Journal of Fluid Mechanics*, **6(04)**, 547–567.

TSENG, Y.H. and FERZIGER, J.H. (2003). "A ghost-cell immersed boundary method for flow in complex geometry". *Journal of Computational Physics*, **192(2)**, 593–623.

VISBAL, M.R. and GAITONDE, D.V. (2002). "On the use of higher-order finite-difference schemes on curvilinear and deforming meshes". *Journal of Computational Physics*, **181(1)**, 155–185.

YE, T., MITTAL, R., UDAYKUMAR, H. and SHYY, W. (1999). "An accurate Cartesian grid method for viscous incompressible flows with complex immersed boundaries". *Journal of Computational Physics*, **156(2)**, 209–240.

APPENDIX A. ENERGY METHOD

To demonstrate the energy method, we apply the procedure to a simplified PDE, that is, rather than analysing the full Navier–Stokes equations in this section, we only focus on the 1D convection–diffusion equation as a model equation.

$$\begin{aligned} &u_t + au_x = bu_{xx}, \quad 0 \le x \le 1 \quad t \ge 0 \\ &u(x,0) = f(x) \\ &u(0,t) = u(1,t) = g(t) = 0 \end{aligned} \tag{25}$$

where a and b are assumed to be constant and positive, and u is the dependent variable. The L_2 scalar product for two real functions v and w is defined by

$$(v,w) = \int_0^1 v(x)w(x)dx \tag{26}$$

which then defines the L_2 norm of the continuous solution at time t and energy $E(t) = \|u(\cdot,t)\|^2 = (u,u)$. Using integration by parts $(v,w_x) = v(1,t)w(1,t) - v(0,t)w(0,t) - (v_x,w)$, the energy method leads to

$$\begin{aligned} &\tfrac{dE}{dt} = \tfrac{d}{dt}\|u(\cdot,t)\|^2 = (u_t,u) + (u,u_t) \\ &= (-au_x + bu_{xx},u) + (u,-au_x + bu_{xx}) \\ &= -a[u^2(1,t) - u^2(0,t)] + 2b[u(1,t)u_x(1,t) - u(0,t)u_x(0,t)] \\ &-2b(u_x,u_x) \le au^2(0,t) + 2b[u(1,t)u_x(1,t) - u(0,t)u_x(0,t)] \\ &= 0 \end{aligned} \tag{27}$$

which yields a non growing solution, i.e. $E(t) \le E(0) = \|f(x)\|^2$. Thus, the energy is bounded by the initial condition.

APPENDIX B. SUMMATION BY PARTS OPERATORS

(Khalili *et al.*, 2016)

The SBP operators are constructed to guarantee a discrete energy estimate similar to the continuous energy estimate above.

$$\begin{aligned} &u_t + au_x = bu_{xx}, \quad 0 \le x \le 1 \quad t \ge 0 \\ &u(x,0) = f(x) \\ &u(0,t) = u(1,t) = g(t) = 0 \end{aligned} \tag{28}$$

where a and b are assumed to be constant and positive, and u is the dependent variable.

The basis of getting such an energy estimate is to satisfy integration by parts in the discrete sense called Summation–By–Parts (SBP) property (Gustafsson, 2008; Svärd and Nordström, 2014). To outline this technique for model problem (28), we consider $u_j = u_j(t)$ the numerical solution of the convection–diffusion equation at grid point $x_j = jh, j = 0,...,N$, with grid spacing $h = \frac{1}{N}$. The solution vector containing the solution at the discrete grid points is $\mathbf{u} = [u_0(t), u_1(t), ..., u_N(t)]^T$. Using a difference operator Q approximating the first derivative in space, the semi-discrete form of the model equation can be expressed as

$$\tfrac{d\mathbf{u}}{dt} = -aQ\mathbf{u} + bQQ\mathbf{u}, \quad u_j(0) = f(x_j) \tag{29}$$

The discrete scalar product and corresponding norm and energy can be defined by

$$\begin{aligned} &(\mathbf{u},\mathbf{v})_h = h\mathbf{u}^T H\mathbf{v}, \\ &E_h(t) = \|\mathbf{u}\|_h^2 = (\mathbf{u},\mathbf{u})_h \end{aligned} \tag{30}$$

where H is a diagonal and positive definite matrix defined by $H = \mathrm{diag}(H_L, I, H_R)$. The SBP property is satisfied by the difference operator Q, if

$$(\mathbf{u},Q\mathbf{v})_h = u_N v_N - u_0 v_0 - (Q\mathbf{u},\mathbf{v})_h \tag{31}$$

or if Q can be written on the form $hQ = H^{-1}P$ for P satisfying

$$P + P^T = E_N - E_0 = \mathrm{diag}(-1,0,...,0,1) \tag{32}$$

where $E_0 = \mathrm{diag}(1,0,...,0)$ and $E_N = \mathrm{diag}(0,0,...,1)$. Using the semi–discrete equation 29, the energy estimate for the semi–discrete problem can be obtained as

$$\begin{aligned} &\tfrac{dE}{dt} = \tfrac{d}{dt}\|u(\cdot,t)\|^2 = (u_t,u)_h + (u,u_t)_h \\ &= (-aQu + bQQu,u)_h + (u,-aQu + bQQu)_h \\ &= -a[u_N^2 - u_0^2] + 2b[u_N(Qu)_N - u_0(Qu)_0] \\ &-2b(Qu,Qu)h \le au_0^2 + 2b[u_N(Qu)_N - u_0(Qu)_0]. \end{aligned} \tag{33}$$

We would get non-growing energy in time if the homogeneous boundary conditions could directly be imposed in (33). However, this will change the difference operator Q such that its SBP property might be lost. To avoid this problem, boundary conditions are weakly imposed by the simultaneous approximation term (SAT) technique (Gustafsson, 2008). A first derivative SBP operator with diagonal quadrature matrix H in (30) is a $O(h^{2s})$ accurate central difference operator which is $O(h^s)$ accurate at and near boundaries $s = 1,2,3$. Such an SBP operator is globally $O(h^{s+1})$ accurate.

APPENDIX C. REFORMULATION OF COEFFICIENTS

The four unknown coefficients $C_i, i = 1,..,4$ can be determined using values of the four variables surrounding the image point. It can be expressed as

$$\mathbf{C} = \mathbf{V}^{-1}\{\phi\} \tag{34}$$

where $\mathbf{V}$ is the Vandermonde matrix corresponding to the bilinear interpolation scheme for four surrounding nodes. The value at the image point can be expressed as

$$\phi_{\mathrm{IP}} = \begin{bmatrix} 1 & x_{\mathrm{IP}} & y_{\mathrm{IP}} & x_{\mathrm{IP}}y_{\mathrm{IP}} \end{bmatrix} \begin{bmatrix} C_1 \\ C_2 \\ C_3 \\ C_4 \end{bmatrix} \tag{35}$$

The vector in bracket can be expressed as

$$\mathbf{V}_{\mathrm{IP}} = \begin{bmatrix} 1 & x_{\mathrm{IP}} & y_{\mathrm{IP}} & x_{\mathrm{IP}}y_{\mathrm{IP}} \end{bmatrix} = \sum_{i=1}^{4} \alpha_i V_i \tag{36}$$

where V_i is the ith row of $\mathbf{V}$ and α_i depends on the coordinates of the image point and the four surrounding nodes. Thereby, the matrix equation for α can be written as

$$\begin{bmatrix} 1 \\ x_{\mathrm{IP}} \\ y_{\mathrm{IP}} \\ x_{\mathrm{IP}}y_{\mathrm{IP}} \end{bmatrix} = \begin{bmatrix} 1 & 1 & 1 & 1 \\ x_1 & x_2 & x_3 & x_4 \\ y_1 & y_2 & y_3 & y_4 \\ x_1y_1 & x_2y_2 & x_3y_3 & x_4y_4 \end{bmatrix} \begin{bmatrix} \alpha_1 \\ \alpha_2 \\ \alpha_3 \\ \alpha_4 \end{bmatrix} \tag{37}$$

By rearranging, α can be obtained as

$$\alpha = \mathbf{V}^{-T}\mathbf{V}_{\mathrm{IP}}^{T}. \tag{38}$$

Thus, the value at the image point can be expressed as

$$\phi_{\mathrm{IP}} = \phi^{T}\mathbf{V}^{-T}\mathbf{V}_{\mathrm{IP}}^{T} \tag{39}$$

Inserting the result obtained in Eq. (38), the value at the image point can obtained be as

$$\phi_{\mathrm{IP}} = \sum_{i=1}^{4} \alpha_i \phi_i \tag{40}$$

Paper IV [55]

High order immersed boundary method for compressible viscous flows based on summation-by-parts operators

M. E. Khalili, M. Larsson, B. Müller

Submitted for journal publication (2017).

Is not included due to copyright

Paper V [57]

Immersed boundary method for viscous compressible flows around moving bodies

M. E. Khalili, M. Larsson, B. Müller

Submitted for journal publication (2017).

Is not included due to copyright